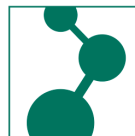# ETH *zürich*

Swiss Federal Institute of Technology in Zurich
Department of Chemistry and Applied Biosciences
Laboratory of Inorganic Chemistry

MAX PLANCK INSTITUTE
FOR POLYMER RESEARCH

Max Planck Institute for Polymer Research
Department of Physics at Interfaces
Laboratory of High-Resolution Atomic Force Microscopy

Perovskite Thin Films under the Microscope: The Impact of Grain Passivation on Morphology and Stability

Master Thesis

submitted by
Thomas William Gries
born 13.02.1994 in Wiesbaden, Germany

Supervising Professor at ETH: Prof. Dr. Maksym Kovalenko
Supervisor at Max Planck Institute: Prof. Dr. Stefan Weber

"You can lead a horse to water,
but a pencil must be lead."

– *RuPaul Andre Charles*

ETH

Eidgenössische Technische Hochschule Zürich
Swiss Federal Institute of Technology Zurich

Declaration of originality

The signed declaration of originality is a component of every semester paper, Bachelor's thesis, Master's thesis and any other degree paper undertaken during the course of studies, including the respective electronic versions.

Lecturers may also require a declaration of originality for other written papers compiled for their courses.

I hereby confirm that I am the sole author of the written work here enclosed and that I have compiled it in my own words. Parts excepted are corrections of form and content by the supervisor.

Title of work (in block letters):

Perovskite Thin Films under the Microscope: The Impact of Grain Passivation on Morphology and Stability

Authored by (in block letters):
For papers written by groups the names of all authors are required.

Name(s):	First name(s):
Gries	Thomas William

With my signature I confirm that
- I have committed none of the forms of plagiarism described in the 'Citation etiquette' information sheet.
- I have documented all methods, data and processes truthfully.
- I have not manipulated any data.
- I have mentioned all persons who were significant facilitators of the work.

I am aware that the work may be screened electronically for plagiarism.

Place, date	Signature(s)
Mainz, 07.12.2020	*Thomas Gimr*

For papers written by groups the names of all authors are required. Their signatures collectively guarantee the entire content of the written paper.

Abstract

Perovskite solar cells still suffer from low stability compared to their silicon counterparts. Various passivation strategies have been applied in order to enhance stability and to reduce defect formation. In this study, the model perovskite compounds $MAPbI_3$ and $Cs_{0.15}FA_{0.85}PbI_3$ were used in order to study the influence of five different passivation agents on the thin film stability and morphology: tetraethyl orthosilicate (TEOS) and (3-aminopropyl)triethoxysilane (APTES) as encapsulating agents, phenylethylammonium iodide (PEAI) for formation of Ruddlesden-Popper-type low-dimensional perovskite, and RbI and KI as defect-passivating agents. Stability under ambient conditions was quantified via photoluminescence- (PL) and ultraviolet-visible- (UV/Vis) spectroscopy as well as X-ray diffraction (XRD). Thin film topography and contact potential difference (CPD) maps were acquired via frequency modulated Kelvin probe force microscopy (FM-KPFM).

APTES, which has never been used before as an additive in thin film synthesis, yielded highly stabilized $Cs_{0.15}FA_{0.85}PbI_3$ films with no noticeable phase change to up to 3 d of ambient storage. This represents a significant enhancement to the pure $Cs_{0.15}FA_{0.85}PbI_3$ film which underwent phase-change within the first hour of ambient storage. FM-KPFM revealed strongly diminished, but highly oriented grains. Faster hydrolysis of APTES monomer compared to TEOS monomer in the precursor solution was detected via ^1H- and ^{29}Si- nuclear magnetic resonance (NMR), indicating largely divergent thin film formation dynamics reflected in the morphology. The promising results regarding thin film stability can motivate further optimization of the synthesis parameters.

The non-stabilizing effect of PEAI additive on $MAPbI_3$ films was assigned to a less pronounced formation of 2D-perovskite as compared to their $Cs_{0.15}FA_{0.85}PbI_3$ equivalents, where highly directed terrace structures on large grains could be associated with the presence of 2D-perovskite via FM-KPFM. Alkali metal iodide additives RbI and KI proved to form distinct phase segregations instead of being located on the grain exteriors and, thus, no significant stabilizing effect was observed under ambient conditions.

Acknowledgements

First of all, I want to express my gratitude to Prof. Dr. Maksym Kovalenko for taking the supervision of the project.

In particular, I would like to thank my supervisors Prof. Dr. Stefan Weber and Yenal Yalçınkaya. They always did their best to guide me through the project and to give me useful support. Thanks to them, I could gain a lot of experience during my time at Max Planck Institute for Polymer Research.

Furthermore, I want to thank Prof. Dr. Stefan Weber and Pascal Rohrbeck for all the practical advice regarding KPFM measurement practice. They were always there to help when I was petrified. Moreover, thanks to Pascal for providing the AFM and FM-KPFM images of the pure $MAPbI_3$ film.

I also want to thank Dr. Alexander Klasen who did pioneering work on perovskite solar cells at an institute technically specialized on polymer science.

For all the introductions on the devices and measurement support I want to thank Petra Kindervater and Manfred Wagner (NMR), Maren Müller and Gunnar Glaßer (SEM), Dr. Rüdiger Berger (AFM/IR), Helma Burg and Leon Prädel (TE) and particularly Michael Steiert (XRD).

I want to express my gratitude to the whole Weber group, to Pravash Bista, Amy Stetten, Yenal Yalçınkaya, Kostas Bidinakis, Pascal Rohrbeck and Amelie Axt, who warmheartedly welcomed me to the group and made my time at Max Planck Institute so enjoyable.

Last but certainly not least, I want to thank my mother, father and brother for being my moral support in all imponderables of life. I would be nothing without them.

Index of Abbreviations

Table of Contents

1 Introduction

1.1 Opportunities and Challenges of Perovskite Materials

The perovskite structure is one of the most ubiquitous structures on planet earth. It is mainly found in purely inorganic silicate minerals like brigdmantite ($MgSiO_3$) which is formed under high pressures in the earth's lower mantle.[1] The ideal cubic perovskite crystallizes in space group $Pm\bar{3}m$ and is based on the chemical formulation ABX_3 (s. Figure 1.1) as found in the eponymous $CaTiO_3$ structure. In its unit cell, the B-cation with oxidation state +IV is octahedrally surrounded by oxygen atoms and the A-cations with oxidation state +II are located in the corners of the cube. Other distributions of oxidation states may also be capable of forming perovskite structures, such as in organolead halide perovskites (OHPs) where the central lead atom is in oxidation state +II and surrounded by halide monoanions, and the organic methylammonium (MA) monocation is located in the corners of the cubic unit cell. Most perovskite structures encountered in nature, however, are of orthorhombic symmetry due to tilting of the corner-sharing octahedra.
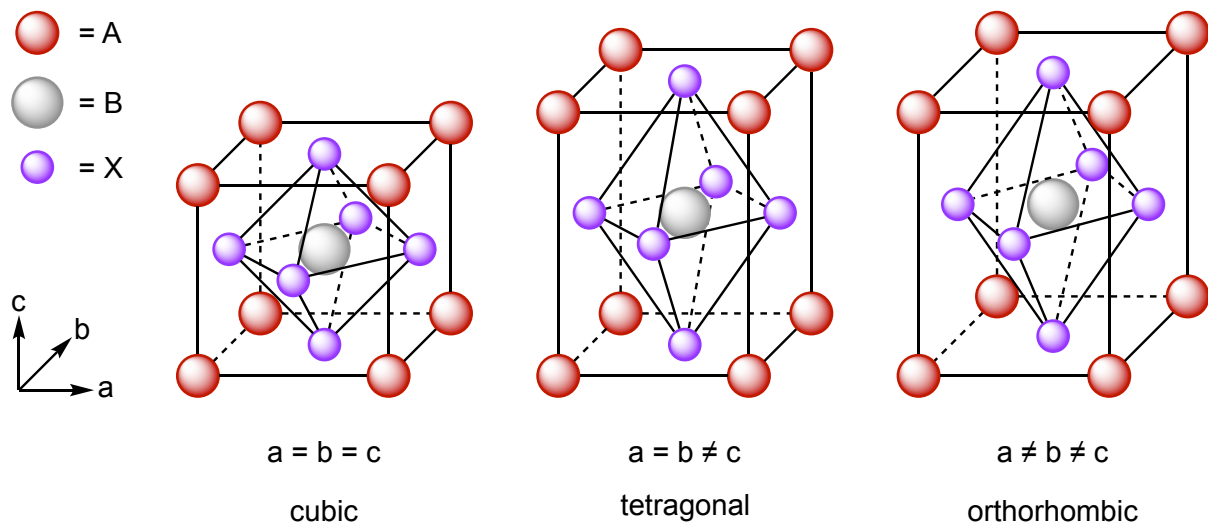

Figure 1.1. Unit cells of the cubic, tetragonal and orthorhombic perovskite crystal structure.

It has been until 2009 that Japanese researchers Miyasaka et al. discovered the potential of OHPs methylammonium lead bromide (MAPbBr$_3$) and methylammonium lead iodide (MAPbI$_3$) for photovoltaic applications.[2] Since then, the research field has received enormous attention with thousands of publications each year, doubtlessly accelerated by the urgency for finding alternative energy sources due to climate change and its implications. OHPs seem to have the ideal characteristics that make them a viable material for photovoltaics. Among those characteristics are a high absorption coefficient of around 10^5 cm^{-1}, low exciton binding energies, long charge carrier diffusion lengths, bandgap tunability by compositional variation as well as a high tolerance to structural defects.[3] These intrinsic material properties are complemented by facile processability from solution by coating techniques such as spin- or dip-coating, or doctor blading in order to fabricate thin films (< 1 µm) of the material. On a research level, solution-processed single-junction perovskite solar cells (PSCs) are now capable of yielding certified 25.5% power conversion efficiency (PCE), as of fall 2020.[4] Such efficiencies are significant considering that, in their landmark paper from 1961, William Shockley and Hans-Joachim Queisser determined the maximum achievable efficiency of this conversion of light to electrical energy to be 30% for a single p-n-junction (defined as the interface between a negatively and a positively doped region in a semiconductor) with a bandgap of 1.10 eV. The researchers assumed the sun to be an ideal black body radiator of 6000 K interacting with a silicon semiconductor at constant 300 K.[5] Furthermore, they assume the quantum efficiency of photon-to-exciton conversion to be 100%, with radiative recombination being the only loss mechanism. However, taking into account atmospheric phenomena such as absorption and scattering of the sunlight, the values of the Shockley-Queisser-Limit slightly shift to 33% PCE at a bandgap of 1.34 eV, still neglecting non-radiative recombination pathways.[6] The high efficiencies achieved today are therefore already on the cusp of the achievable thermodynamic limit. Besides in photovoltaics, perovskite semiconductors especially find application in the areas of field-effect transistors, light emitting diodes and photoluminescent colloidal nanocrystals.[7]

Despite its benefits regarding material properties, the path towards commercialization of PSCs is largely hindered by device instability. External factors such as sensitivity to moisture and oxygen can be tackled by device encapsulation.[8] The far more inhibiting contribution is made by internal factors such as the thermal decomposition and ion migration during operation of the device.[8] These require careful compositional engineering on the thin film and are far from being fully understood.

1.2 Conversion Losses in Perovskite Solar Cells

In a semiconductor like perovskite, electrons are excited from the valence band to the conduction band of the material upon irradiation with photons exceeding the energy of the bandgap E_g. Thereby, an electron-hole pair is generated, the so-called exciton. After excitation, the electron relaxates to the conduction band edge due to thermalization, mirrored by the hole in the valence band, as illustrated in Figure 1.3. Thus, any surplus excitation energy with respect to the bandgap is released in this process. It is converted to heat and is therefore lost for the conversion to electricity.

In a solar cell, the charges created by irradiation need to be separated in order to generate an electrical current. One major advantage of perovskites is their low exciton binding energy of around 50 meV due to its high dielectric constant, which makes it possible for the generated charges to be screened from each other effectively.[9] The free charges are then extracted by charge-selective layers. This is realized by "sandwiching" the perovskite ambipolar transport layer in between an n-type (electron-transport layer, ETL) and a p-type (hole-transport layer, HTL) contact from which the charges are then fed into the electrical circuit via metal contacts (s. Figure 1.2).[10] Depending on the order of deposition of these layers, the devices are thus classified as n-i-p or p-i-n architectures.

Figure 1.2. Schematic of the fundamental structure of a solar cell in n-i-p architecture.

In addition to thermalization, further energy losses occur radiatively as well as non-radiatively. In radiative decay, electrons from the conduction band recombine with holes in the valence band and re-emit light equal to the bandgap energy. This photoluminescence (PL) effect cannot be avoided. Non-radiative decay, in turn, is caused by deep electronic trap states in which the charges that are not extracted by the device are confined until they are annihilated by a hole and a phonon is emitted. Note that non-radiative Auger recombination represents a third pathway of decay. Here, an electron and a hole recombine, and the released energy is directly consumed by excitation of a second electron. The Auger effect, however, has been shown to largely occur at high carrier densities beyond the ones present in PSCs.[11]
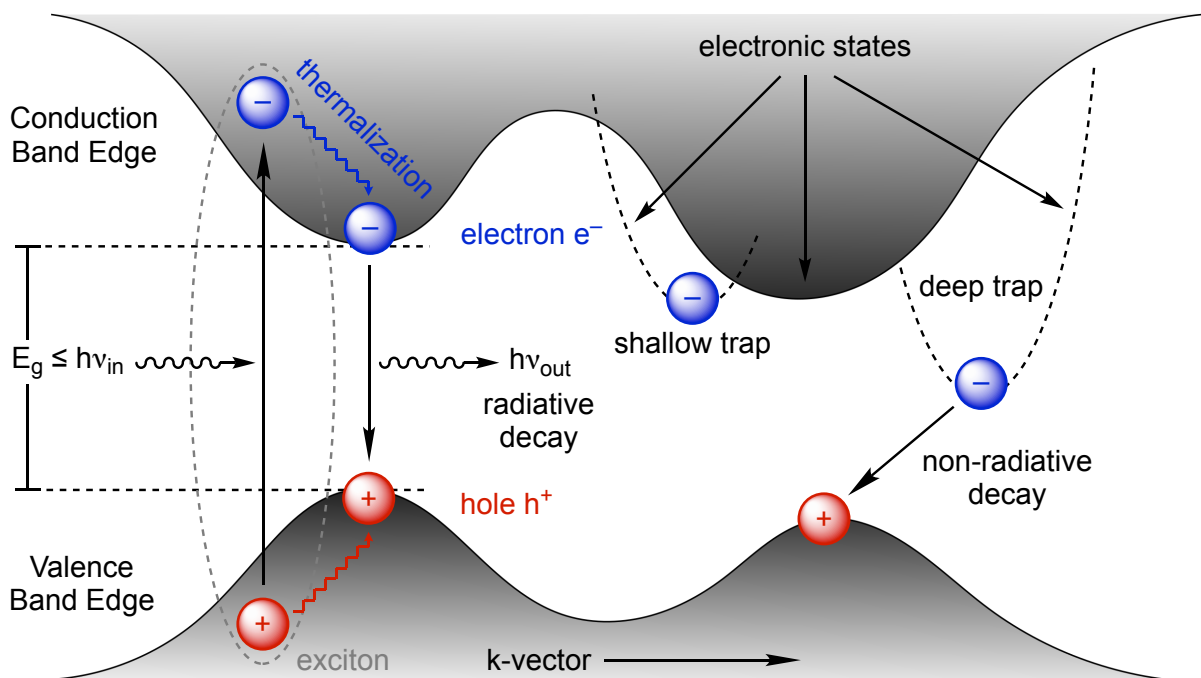
Figure 1.3. Schematic of the valence and conduction band in a direct semiconductor. After irradiation, the formed exciton can decay radiatively or non-radiatively.

It is known that defects in the bulk perovskite crystal such as interstitials and vacancies possess low formation energies and only introduce shallow trap states close to the conduction band.[12] In the first instance, these shallow traps are not detrimental to the device's performance and are certainly a sign of the perovskite's high defect tolerance and high achievable open-circuit voltages. However, their mobility within the crystal is high, especially when an electric field is applied, so that they can become detrimental when they accumulate at the perovskite film's surface and interfaces.[3]

Generally, deep level trap states within the bandgap are detrimental to the device's performance. These trap states arise due to several factors: Interfaces and surfaces of the perovskite films including grain boundaries (GBs), for example, play an important role as introducers of deep-level traps.[3] Lucky for the scientist, those factors underly human engineering, at least in theory. Nevertheless, the dynamics of the traps states and their practical mitigation is still poorly understood.

Especially, the role of GBs is currently heavily debated. A GB is the interface where two grains of the film converge and can, therefore, be considered as an extended 2-dimensional defect area. One might be inclined to think that the high density of defects leads to the deep level traps described above and, thus, increases the rate of non-radiative decay. In fact, a 2015 study by De Quilettes et al. demonstrate lower PL intensity localized on the GBs, suggesting higher non-radiative decay.[13] Another study by Yun et al., however, claims a beneficial role of the GBs: The researchers found via Kelvin probe force microscopy (KPFM) and conductive atomic fore microscopy (c-AFM) measurements that charge extraction and collection actually occurred more efficiently along the GBs.[14] In a nutshell, a concise picture of the role of surface defects is still lacking.

Regarding passivation of surface defects, various strategic routes have been taken with beneficial effects on the device performance. A synopsis of the variety of possible causes of deep trap states and respective defect passivation strategies is given in Figure 1.4. Among those surface defects are charged imbalances such as undercoordinated or vacant ions, as well as structural imperfections such as metallic clusters or GBs.[3] Different strategies have to be applied in order to adapt to the type of defect on an individual basis. In this study, grain encapsulation strategies are juxtaposed to strategies encompassing the addition of ammonium salts as well as alkali metal salts. Thereby, the study hopes to contribute to elucidating the effect of grain passivation both on the nanostructure of perovskite thin films and their degradation dynamics.
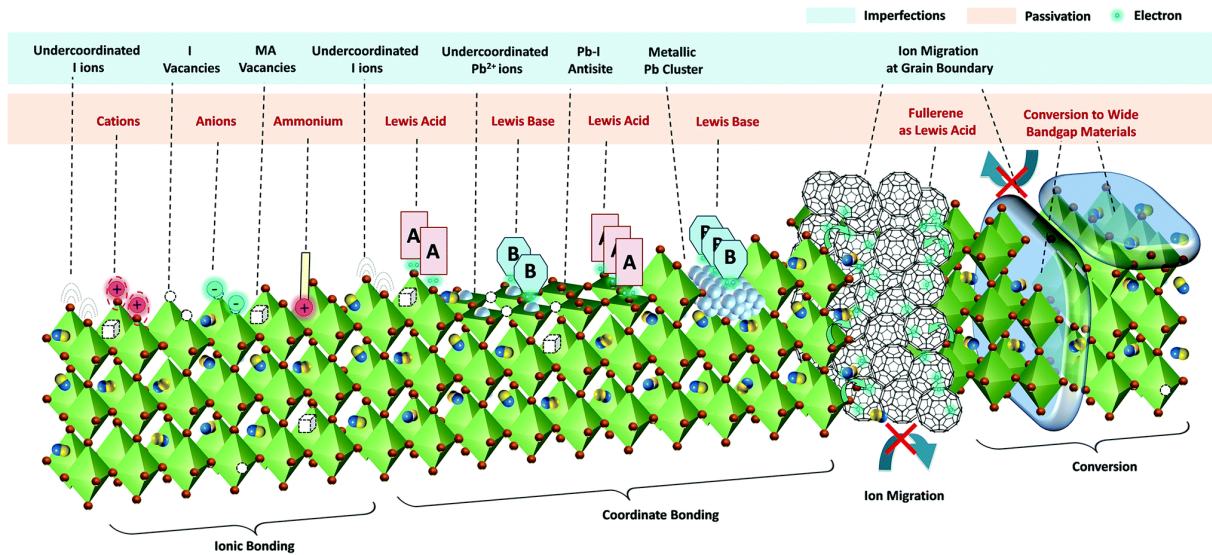
Figure 1.4. Schematic showing the numerous types of surficial defects and respective passivation approaches. Image taken from ref. [3].

1.3 Degradation and Passivation

The most prototypical representative of the OHP class is MAPbI$_3$ with a bandgap of around 1.55 eV. One major drawback of MAPbI$_3$ thin films is the instability of the MA$^+$ ion under humid and illuminated conditions as well as elevated temperatures.[15] For instance, water from the environment can, in a reversible reaction, form a monohydrate with the perovskite film especially at the GBs.[16] Li et al. showed that although the monohydrate could be removed under dry conditions, additional GBs were introduced into the film, which are detrimental to the device's performance due to additionally formed trap states.[16]

On the contrary, the main irreversible degradation pathway has been shown to be the evaporation of methylamine after deprotonation, also catalyzed by the contact to moisture.[17][18] Furthermore considered was the degradation via evaporation of iodomethane and ammonia, which is thermodynamically favored but largely kinetically hindered due to the higher degree of necessary bond rearrangement.[17] As a result from methylamine evaporation, areas with a high defect density develop due to non-stoichiometric elemental distribution on the surface.[19] Hence, a passivation strategy that provides iodide and furthermore occupies the formed vacancies seems to be a prerequisite in extending MAPbI$_3$ film lifetimes.

Not only does passivation provide the stability of the bare film, but it also improves the performance of the device in which the film is embedded. The performance of a PSC is characterized by the parameters open-circuit voltage (V_{OC}), the short-circuit current density (J_{SC}), the fill factor (FF) and the PCE. As discussed above, in an ideal case, charges that are generated due to irradiation eventually recombine radiatively. Therefore, there exists a charge concentration within the semiconductor at which the rates of excitation and relaxation are equally fast, ultimately splitting the thermodynamic equilibrium Fermi level into two quasi-Fermi levels.[3] The open-circuit voltage of a solar cell is directly related to the degree of splitting of these quasi-Fermi levels. Defect states, in turn, introduce alternative pathways for non-radiative charge carrier recombination and thus decrease the splitting of the quasi-Fermi levels, leading to a decreased V_{OC}.[20] The maximum achievable V_{OC} was determined to be 1.32 V for MAPbI₃ with a bandgap of 1.60 eV.[20] Additionally, J_{SC} and, consequently, FF are also negatively affected by non-radiative recombination at defect states. A successful passivation of defect states in PSCs is therefore always reflected in high V_{OC}, J_{SC} and FF. The different approaches to passivate the grains of MAPbI₃ as well as formamidium lead iodide (FAPbI₃) thin films will be introduced in the following paragraphs.

Grain encapsulation represents one strategy to retain evaporating methylamine and protect the grain from contact with air and humidity.[21] For that purpose, a thin layer of an oftentimes insulating material is synthesized *in-situ* around the grains. It can therefore be considered to be more a defect prevention rather than a defect passivation strategy. Silica-precursors such as the tetraethyl orthosilicate (TEOS) and (3-aminopropyl)triethoxysilane (APTES), which were used in this work, fall into this category. Using APTES extends the encapsulation technique by an active amine functionality (s. Figure 1.5). This approach has never been taken before and, thus, it is not known if the propylamine moiety acts as a Lewis-basic coordinating agent for undercoordinated lead(II) or if the chain ends are incorporated into the lattice as propylammonium A-site cations.
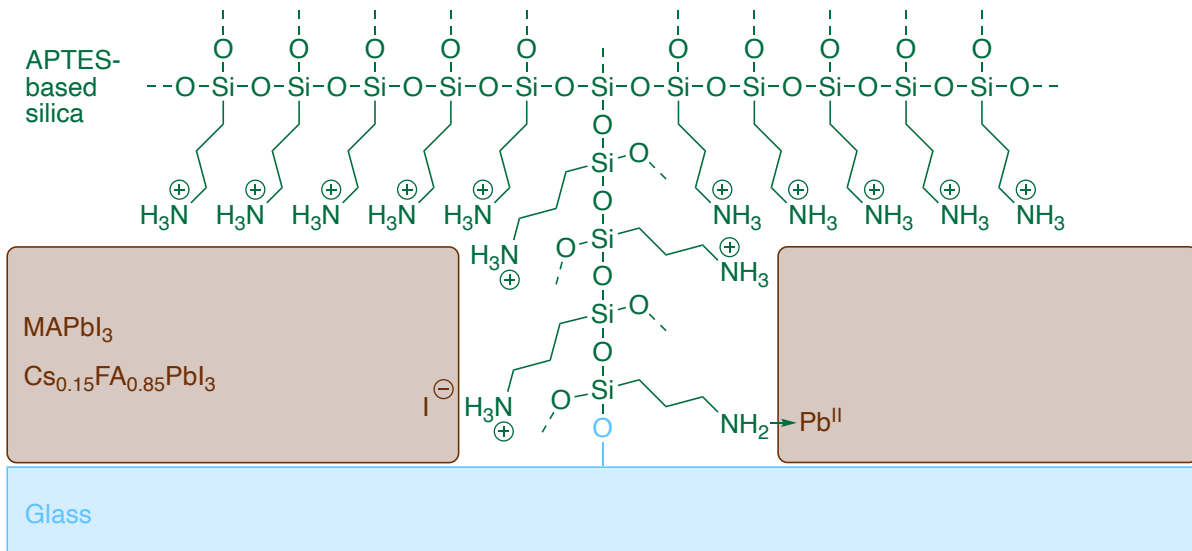
Figure 1.5   Suggested mechanism of polymerized APTES acting as an encapsulation agent for perovskite grains. It is not known if the protonated amine functionality is incorporated into the perovskite lattice (left) or if the electron pair of the amine coordinates undercoordinated lead on the perovskite surface as a Lewis base (right).

2-Phenylethylammonium iodide (PEAI) is known to form a sheet-like perovskite of Ruddlesden-Popper phase, as shown in Figure 1.6.[22][23] The PEA$^+$ ion is expelled during perovskite crystallization due to lattice mismatch, so that it accumulates at the GBs, where the 2-dimensional Ruddlesden-Popper phase is formed. The morphology of this 2D-perovskite passivation layer has been proposed not to be a uniformly sheet-like structure spreading around the grain, but rather a mixture of sheets with $n \times n$ PbI$_6^-$ octahedra (n = 1-4) included in a shell of PEA$^+$ ions.[24] Here, the charged ammonium functionality is included in the crystal lattice on the A-site while the phenyl moiety acts as a spacer in between the individual sheets. With the 2D-layered perovskite, a wider bandgap material is introduced in between the grains, generating a heterojunction on each GB.[25] That way, charge carriers are more inclined to be reflected on this introduced energy barrier instead of being trapped and recombining non-radiatively.[3][25] Moreover, the introduction of a phenyl group close to the surface of the perovskite film increases its hydrophobicity and impedes the penetration with ambient water.[26]
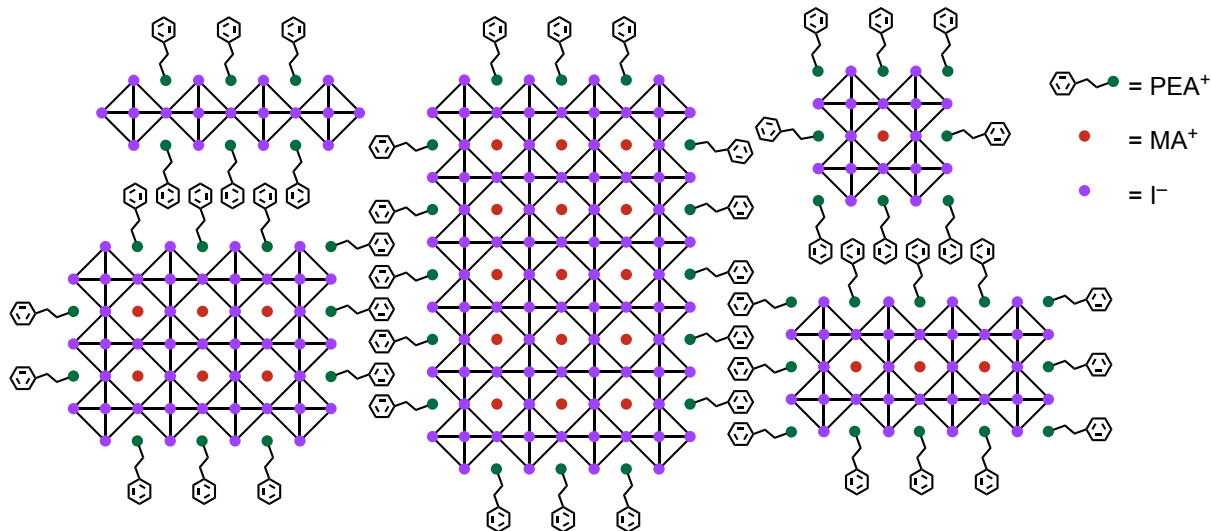
Figure 1.6. Formation of 2-dimensional Ruddlesden-Popper phase in a MAPbI$_3$-PEAI-system.

In a third passivation approach, inorganic salts like alkali metal iodides are added to the perovskite precursor solution in order to generate an excess of iodide in the resulting film. On one hand, this passivation strategy fills occurring iodide vacancies on the surface of the perovskite grains and, on the other hand, the alkali metal cations may passivate other surface defects such as undercoordinated iodide (s. Figure 1.4).[27] The considerably smaller ionic radius of rubidium (s. Table 6.3) compared to MA and a decreased tolerance factor (s. Section 6.6.2) raised questions about its incorporation into the perovskite crystal lattice. While initial reports suggested an incorporation at low molar amounts,[28] more recent nuclear magnetic resonance (NMR) studies found no sign of incorporation whatsoever.[29] Nevertheless, a positive impact of Rb- and K-addition on open-circuit voltage, shot-circuit current, fill factor, PCE as well as increased stability have been reported.[27][29]

The pathway of degradation in FAPbI$_3$ films is qualitatively different from the degradation in MAPbI$_3$ films. In FAPbI$_3$, a phase-transition occurs from the photoactive α-phase to the thermodynamically more stable δ-phase at around 150 °C.[30] Due to the larger size of the FA$^+$ ion, a perovskite crystal structure is thermodynamically unfavored at room temperatures, as can be estimated from the tolerance factor t, as demonstrated in Section 6.6.2.[31] In order to tune the tolerance factor to a more favorable range of 0.8-1.0, the smaller cation cesium is added, which is fully incorporated into the perovskite lattice up to 15 mol%, mitigating the lattice strain and, therefore, lowering the phase transition temperature to the order of room-temperature.[29] However, the phase transition is facilitated by humidity, which is the reason

for the higher sensitivity to degradation of $Cs_{0.15}FA_{0.85}PbI_3$ films under ambient conditions than $MAPbI_3$ films. With around 1.40 eV, the direct bandgap transition of FA-based films is closer to the optimum bandgap for photovoltaic applications than in $MAPbI_3$ films, which makes research on these materials a promising area of research.

Although intrinsically more stable towards high temperatures, the formamidinium (FA^+) ion especially shows instability when brought into contact with water and is converted to ammonia and *s*-triazine.[30][32] With formamidinium-based films, encapsulating agents like TEOS and APTES are supposed to screen the perovskite film from water to prevent this conversion rather than retaining the cation inside the grain. 2D-passivation and passivation with inorganic cations is assumed to work similarly to the $MAPbI_3$ films described above.

We have seen that perovskite film degradation poses qualitatively different challenges that need to be addressed individually on the level of passivation. In this study, the three fundamentally different passivation approaches described above are compared to each other: A grain encapsulation approach with TEOS and APTES, the 2D-3D-hybrid structure introduced by PEAI addition, as well as RbI and KI as inorganic salt additives. Besides comparing the ambient stability of the synthesized films, this study uses atomic force microscopy (AFM) imaging and FM- (frequency modulated) KPFM as a means to measure contact potential differences (CPD) on the perovskite surface. The generated topography and CPD maps provide information on the mechanistic details of the chosen passivation strategies.

2 Methods

2.1 Atomic Force Microscopy

AFM is able to map sample surfaces with high resolution and in a minimally destructive way. It does not require highly energetic electromagnetic radiation like in X-ray diffraction (XRD) or electron beams like in scanning electron microscopy (SEM) in order to characterize surfaces. Therefore, it is an ideal method to investigate photosensitive materials such as perovskite thin films.

(a) Forces Acting Between Sample and Tip

The fundamental principle of AFM is beautifully simple: A very sharp tip mounted on a supportive beam structure is moved over the sample surface, similar to a record player. The tip together with the beam structure is called cantilever and is usually made of silicon or silicon nitride. Various types of forces can occur between tip and sample, with van-der-Waals forces, electrostatic forces, chemical forces and magnetic forces being the most important ones. From the interaction, information can be obtained about the morphology of the surface: In topography imaging, for instance, repulsive forces due to Pauli repulsion at short distances and attractive electrostatic and van-der-Waals forces at larger distances are considered. The interaction between tip and surface can be modeled in a force-distance-curve as shown in Figure 2.1. During the movement over the surface, the cantilever interacts with the sample via a force field, causing the cantilever to deflect.

(b) Cantilever Deflection and Detection

In an AFM device, the tip-sample displacement is controlled by a z-piezo element to which the cantilever is connected. When the piezo element is approached towards the sample surface from an infinite distance, the cantilever initially experiences no force and remains in its rest position (step 1 in Figure 2.1). A few nanometers above the surface, the cantilever enters the force field of attractive van-der-Waals and electrostatic forces, and a fast snap-to-surface (step 2, so-called "snap-in") occurs, causing the cantilever to deflect downwards. Upon further approach of the

piezo element, the cantilever first returns to its rest position before Pauli repulsions cause upwards deflection (step 3). During retraction (step 4), additional adhesive forces come into play, causing a delayed withdrawal from the surface (step 5, so-called "pull-off"). The force between sample and tip can thus be inferred from the degree of deflection via the equations of Hooke's law due to the cantilever's spring-like behavior.

The detection of the cantilever deflection is usually accomplished optically by a laser: The laser beam is directed on the reflective backside of the cantilever, and the reflected light is projected on a four-quadrant photodiode which converts the incident light into up to four electrical signals, depending on the laser beam location. It is therefore not only sensitive to vertical deflections of the cantilever, but also to lateral deflections.

(c) AFM Modes

The three most important modes to drive the AFM device are contact mode, non-contact mode and tapping mode, of which each utilizes different regimes of the force-distance curve. Non-contact mode is only operable in ultra-high vacuum and will not be considered here. In contact mode, the cantilever is in contact with the sample at all times. Due to the large repulsive forces in this regime, however, damaging of the sample or the tip are likely to occur.

In tapping mode, on the contrary, the cantilever is excited at its first resonance frequency while being moved along the surface at a distance corresponding to the attractive regime, as designated in Figure 2.1. The excitation is achieved with an additional piezo element (so-called actuator). During the movement, the tip is only punctually touching the surface, keeping the destructiveness to the surface at a minimum.
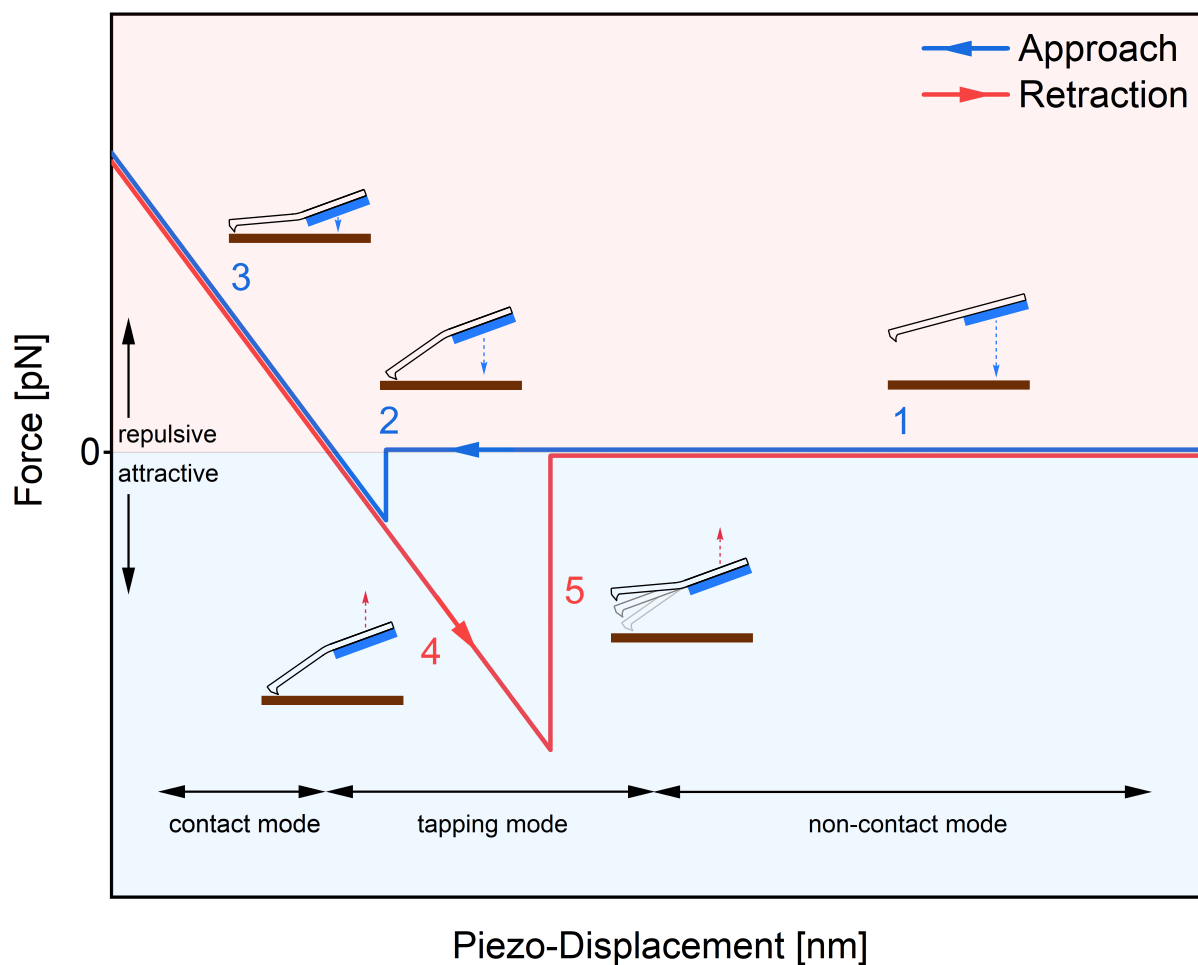
Figure 2.1   The tip-sample interaction is approximated by a force-distance curve. Contact mode, tapping mode and non-contact mode are each performed in different regimes of the curve.

(d) AFM Measurement

The fundamental setup of an AFM device is shown in Figure 2.2. In tapping-mode, the cantilever can be considered a driven harmonic oscillator which is damped by the force field between tip and sample. During a scan, the laser continuously measures the amplitude of the cantilever's vibration, while the sample is moved in the x,y-plane. If the tip approaches an elevated structure on the sample surface, the altered force gradient between the two will cause the amplitude to decrease. Inversely, a lower structure will cause the amplitude to increase. The change in amplitude is registered by the feedback electronics by comparison to the given setpoint amplitude. The deviation is translated into the z-signal, which triggers the z-piezo to adjust to the change according to the constant setpoint amplitude. Furthermore, the z-signal generates the topography image.
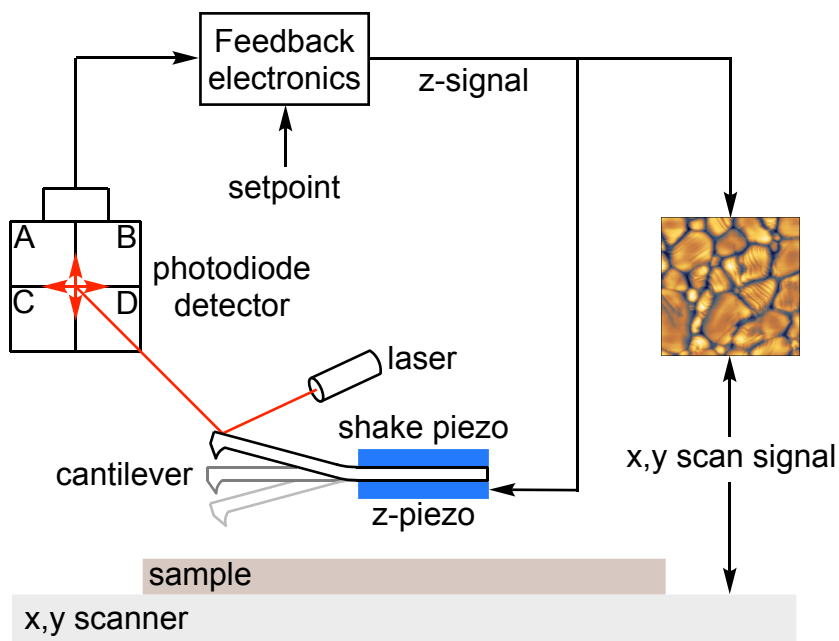
Figure 2.2. Fundamental AFM setup. The amplitude is detected by the four-quadrant photodiode via the deflection of the cantilever. After comparison with the setpoint, an error signal (z-signal) is generated and fed back to the z-piezo which then adapts according to the height.

Besides the bare topography, AFM is capable of mapping out other properties of the sample. For example, the local Young's modulus of a sample can be extracted from the force-distance curves. Furthermore, electrical properties of the sample can also be measured by exchanging the usually non-conductive tip to a conductively coated tip. In KPFM, this capability of the AFM device is exploited. KPFM accomplishes to provide information about the electrostatic forces between the tip and the sample, which makes it an ideal candidate for spatially resolved examination of local properties of perovskite thin films.

2.2 Kelvin Probe Force Microscopy

Following commentary on the working principle of KPFM is based on a paper by Axt et al.[33] When two conductors are brought into contact with each other, electrons move from the material with the higher Fermi level to the material with the lower Fermi level, so that an electrostatic force field is created according to the difference in work functions of the respective materials, as visualized in Figure 2.3. The same occurs if we consider the conductive AFM cantilever with Fermi energy ε_F^{tip} and the sample with Fermi energy ε_F^{samp}. The potential difference U_{CPD} is described by Equation 1.

(1) $$U_{CPD} = \frac{\phi_{tip} - \phi_{samp}}{e}$$

U_{CPD}:   contact potential difference

ϕ: work function

e: elemental charge

In KPFM, the system of tip, sample and the space in between is best described by a capacitor charged with energy E according to Equation 2.

(2) $$E = \frac{1}{2} \cdot C \cdot (\Delta U)^2$$

E: energy

C: capacity

ΔU: potential difference

To obtain the electrostatic force between tip and surface, the energy of the capacitor is derived with respect to the distance between the two, yielding Equation 3. Furthermore, the potential difference ΔU can be interpreted as the difference in any externally applied voltages U_{ext} and the potential difference U_{CPD}.

(3) $$F_E = \frac{1}{2} \frac{\partial C}{\partial z} (U_{ext} - U_{CPD})^2$$

F_E: electrostatic force

z: distance

The KPFM experimental setup is shown in Figure 2.4. The sample itself is grounded at all times in order to prevent the accumulation of excess charges. Simultaneously, a constant bias voltage U_{DC} as well as an alternating current (AC) voltage U_{AC} are applied between tip and sample. U_{ext} can now be reformulated as the sum of U_{AC} and U_{DC}, leading to Equation 4.

$$(4) \qquad F_E = \frac{1}{2}\frac{\partial C}{\partial z}(U_{DC} + U_{AC}\sin(\omega_E t) - U_{CPD})^2$$

ω_E: angular frequency

t: period

The expression is now expanded, and its terms are sorted according to the angular frequency, leading to the three spectral components of the force as presented in Equations 5-7.[33] From those equations, it becomes evident that the application of U_{AC} at the frequency ω generates a modulation of the force both at frequencies ω_E and $2\omega_E$.

$$(5) \qquad F_{stat} = \frac{1}{2}\frac{\partial C}{\partial z}\left[(U_{DC} - U_{CPD})^2 + \frac{U_{AC}^2}{2}\right]$$

$$(6) \qquad F_{\omega_E} = \frac{\partial C}{\partial z}(U_{DC} - U_{CPD})U_{AC}\sin(\omega_E t)$$

$$(7) \qquad F_{2\omega_E} = -\frac{1}{4}\frac{\partial C}{\partial z}U_{AC}^2\cos(2\omega_E t)$$
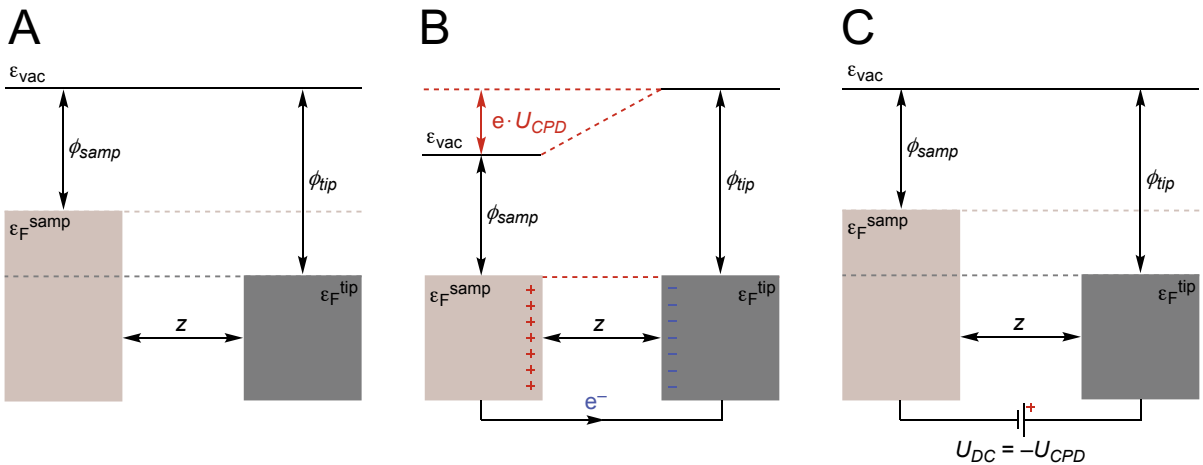
Figure 2.3. Schematic of the fundamental process of equilibration when two materials with different work functions (A) are brought into electrical contact with each other (B). Electrons will flow from the material with higher Fermi energy to the material with lower Fermi energy, creating a potential difference U_{CPD}. (C) By applying an external bias voltage U_{DC} the potential difference U_{CPD} can be nullified. Figure modified from ref. [34].

Similar to AFM, the force between tip and sample is inferred from the oscillation of the cantilever measured by a laser. In AM-KPFM, the oscillation amplitude A is used as an observable value. During the scan over the surface, a feedback-loop adjusts the bias voltage U_{DC} in order to nullify the cantilever's oscillation amplitude. The required U_{DC} then equals the negative U_{CPD} at a given position. However, AM-KPFM measurements are susceptible to imaging artifacts due to AC-coupling of U_{AC} with the actuator piezo.[33] Moreover, stray capacitance from the cantilever beam and the tip-cone contribute to the capacitance gradient in Equations 5-7, leading to a deteriorated lateral resolution.[33] Therefore, AM-KPFM was complemented by FM-KPFM, which was the method of choice for this study.

When mechanically vibrating in the force field of the surface, the cantilever experiences a shift in its resonance frequency ω_0 due to its altered effective spring constant. This shift is proportional to the change in force with respect to the distance and is approximated by Equation 8.

$$(8) \qquad \Delta\omega \approx \frac{\omega_0}{2k} \cdot \frac{\partial F_{TS}}{\partial z}$$

$\Delta\omega$: frequency shift

ω_0: resonance frequency

k: spring constant

F_{TS}: tip-sample force

In FM-KPFM, the external application of U_{AC} introduces a periodically fluctuating electrostatic force field at frequency ω_E. Due to the fact that the spectral components of the electrostatic force F_E (Equations 5-7) are contained in the tip-sample force F_{TS}, the cantilever's resonance frequency experiences a modulation of its resonance frequency at ω_E and $2\omega_E$, as implied by Equation 8. After Fourier transformation, this modulation becomes visible as two sidebands around ω, precisely at $\omega \pm \omega_E$ and $\omega \pm 2\omega_E$.[33]

Another implication of F_E being contained in F_{TS} is the fact that measurement at the sidebands is now sensitive to the second derivative of the capacity with respect to the distance (C'') instead of the first derivative (C'). Thus, long-range contributions of the cantilever beam and the tip-cone to the electrostatic force are suppressed, enhancing the measurement resolution compared to AM-KPFM.

During the scan of a surface, FM-KPFM measures the oscillation amplitude A and the phase φ of the cantilever as observable values via projection of the laser beam on the four-quadrant photodetector. Analogously to topography imaging in AFM, the A-signal is processed by a first lock-in amplifier which controls the height over the surface via the z-piezo element. Additionally, the φ-signal is fed into a second lock-in amplifier (s. Figure 2.4), determining the amplitude of the sideband signals $\omega \pm \omega_E$ and $\omega \pm 2\omega_E$. The KPFM feedback then uses this amplitude information in order to adjust U_{DC} so that the sidebands vanish. Then again, U_{CPD} equals $-U_{DC}$.
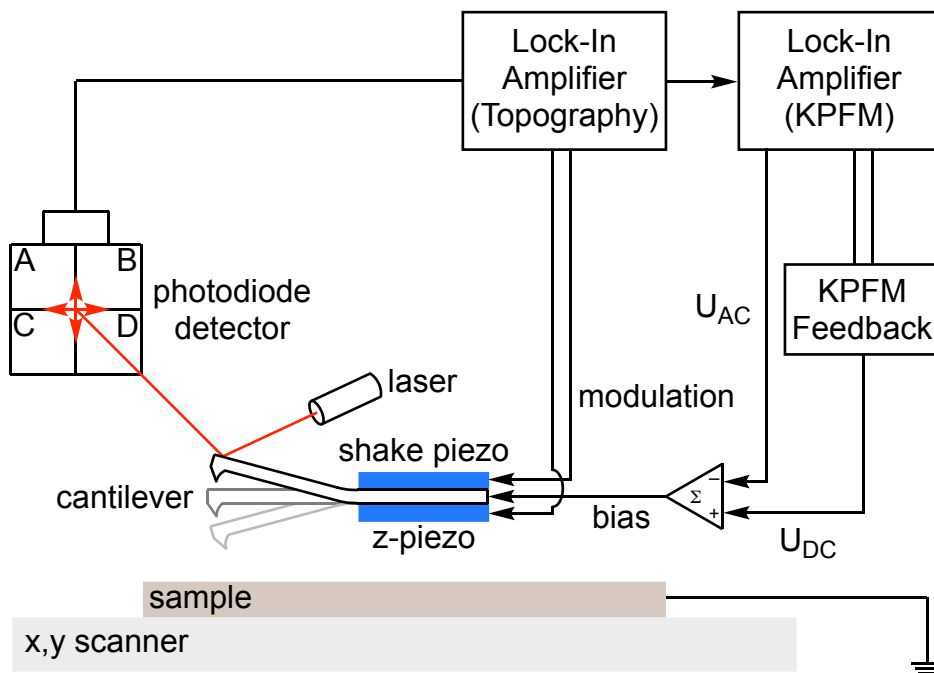
Figure 2.4. FM-KPFM setup. Amplitude and phase of the cantilever are detected by the four-quadrant photodiode via the reflection of the laser on the cantilever backside. Like in AFM, the first lock-in amplifier detects the amplitude, generates the z-signal and adjusts the height of the cantilever according to the sample topography. The second lock-in amplifier infers the sideband amplitude from the φ-signal. The KPFM feedback then nullifies the sidebands by adjusting U_{DC} applied to the cantilever.

Using FM-KPFM, the CPD between tip and the surface of perovskite films can be visualized with high resolution. However, in order to obtain absolute values regarding the local work functions of the sample ϕ_{samp}, calibration of the tip's inherent work function ϕ_{tip} is required prior to each measurement. Such calibrations are usually achieved by measuring the CPD of the cantilever against a material with known work function, such as highly oriented pyrolytic graphite (HOPG).[35] In this study, however, we were primarily interested in the contrasts contained within one image. For this purpose, calibration of the cantilever is not required since images showing U_{CPD} provide equal contrast to images showing ϕ_{samp}, only with an ideally constant offset.[36] It is known that the work function of a Pt-Ir-coated silicon tip is around 5.5 eV, which can give an estimation of the absolute values.[35] Note that all KPFM images within this work were only ever taken under dark conditions.

2.3 Contributions to the Local Contact Potential Difference

The U_{CPD} visualized in KPFM images contains several contributions, the deconvolution of which is not always easy to achieve. In FM-KPFM, there is still a contribution of the tip itself that cannot entirely be eliminated. At steep edges on the sample surface, the electrical contact area between the cone-shaped tip and the sample cannot be assumed to be constant. A higher contact area in those regions translates into an overestimation of the local CPD on edges against scan direction and an underestimation of the CPD on edges in scan direction. An estimation if this effect plays a role can be achieved by an overlay of the CPD signal with the surface topography, but nonetheless it is important to prepare the samples as smooth as possible. In addition to topography crosstalk, sample particles adhering to the tip may significantly alter the measured CPD signal.

Furthermore, the CPD signal is dependent on the chemical nature of the sample. Two materials that show deviating work functions can be distinguished on the basis of the height of their CPD signal. KPFM, therefore, can provide information about phase segregations on the sample surface. As long as the difference in the materials' work functions is sufficiently large, two phases can fairly certainly be discerned. More subtle variations caused, for example, by microsegregations within a mixed cation perovskite grain are more difficult to extract from the total signal.

In general, the height of the CPD signal can also be influenced by upward or downward band bending at the sample surface, as illustrated in Figure 2.5. Downward band bending implies locally lower vacuum energy levels, which lead to a higher U_{CPD} if the Fermi level of the tip is assumed to be constant throughout the scan line. Band bending can be induced by several effects: One important effect is downward band bending due to donor-type defect states that lead to hole accumulation and electron depletion regions in the valence band.[34] Upward band bending, thus, is induced by acceptor-type states leading to electron accumulation and hole depletion in the valence band.[34] Illuminating the sample during the measurement is useful to specifically extract information about band bending and surface trap states due to higher charge carrier concentrations.
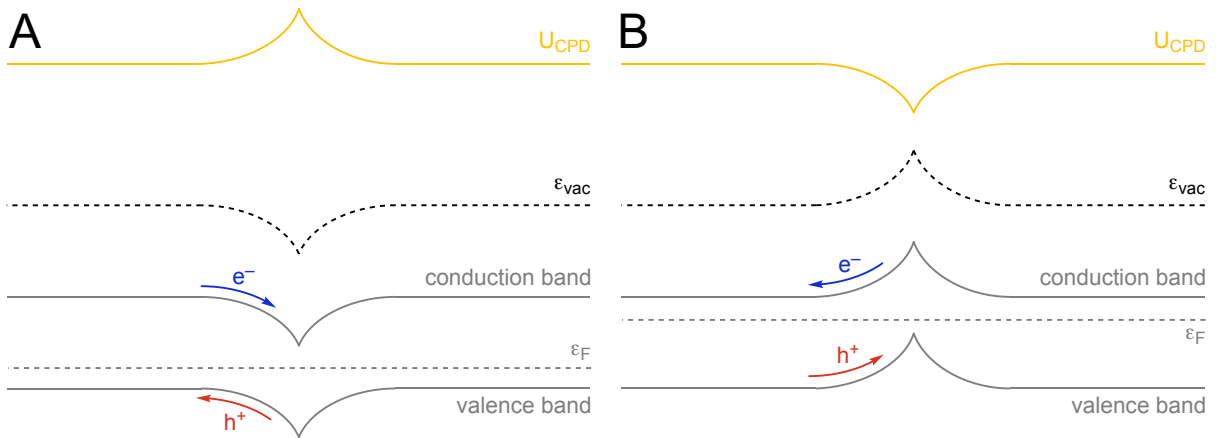

Figure 2.5.   (A) Downward band bending at the sample surface (grey) and its translation via the vacuum energy level ε_{vac} (black) to the measured contact potential difference U_{CPD} (orange). Fermi levels ε_F are aligned. (B) The reverse is the case for upward band bending. Figure modified from ref. [37].

Above, it was discussed how the value of ϕ_{samp} is sensitive to chemical modification as in grain passivation due to band bending. In addition, physisorption of dipolar molecules such as ambient water influences the measured value of U_{CPD} via elevation of the effective work function, leading to an underestimated U_{CPD} value.[38] The physisorption is dependent on surface polarity and hygroscopicity which may vary between differently passivated samples. This dependence is mitigated as much as possible by taking the KPFM measurement in an argon-filled glovebox with below 0.2 ppm water concentration.

Also ultimately related to band bending is a proven crystal facet dependence of the CPD of perovskite grains: For instance, the (100)-facet of cubic MAPbI$_3$ shows a higher inherent density of iodide vacancies, while the (112)-facet of the same material rather shows MA and Pb vacancies.[39] Considering the MAPbI$_3$ crystal structure, only the (100)-plane is intrinsically non-charged.[19] Since in thin films many other orientations may occur, it is conceivable that ions migrate to those charged surfaces in order to achieve charge neutrality, increasing the total number of point defects and, moreover, create an inherent facet-dependence of the CPD due to the defect density present on the surface.[19]

All the effects described above need to be taken into consideration when discussing KPFM images. Although a deconvolution may sometimes be difficult, the trends extracted by comparison of differently passivated samples can provide valuable information about the nature of a chosen passivation strategy.

3 Motivation

When we first started the characterization of the perovskite thin films, SEM seemed to be the most feasible and quick method to obtain information about the morphology of the prepared films. Figure 3.1 shows two examples of SEM images of the same area of an encapsulated $Cs_{0.15}FA_{0.85}PbI_3$ thin film synthesized on conductive FTO substrate, taken in a time interval of 5 min. From the formation of the substrate-deep gaps in between the grains, it becomes strikingly clear that the incident electron beam of the electron microscope has a strongly destructive effect, and that SEM might not be the method of choice in order to analyze the sensitive films.
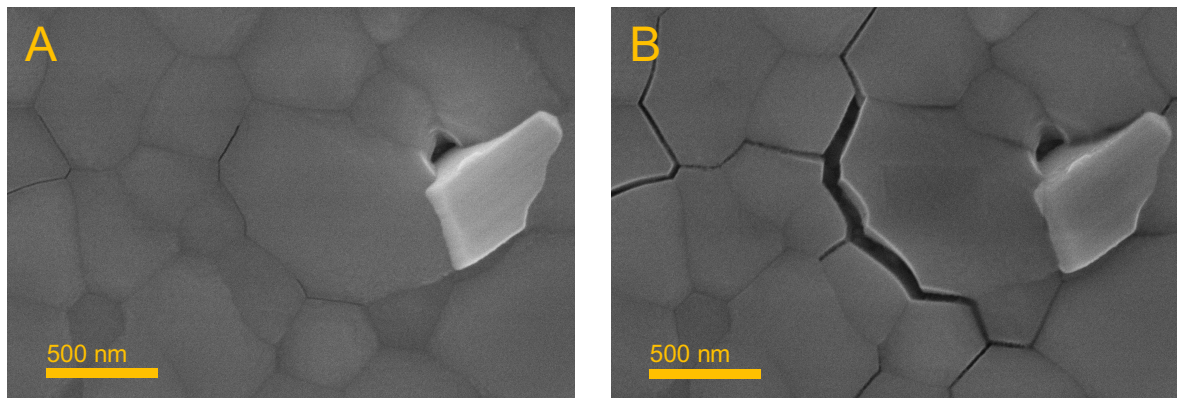

Figure 3.1. SEM images of a $MAPbI_3$ film passivated with TEOS grown on FTO-glass at an acceleration voltage of 10 kV and 50'000-fold magnification (A) in native state at t_0 and (B) after 5 min of irradiation with the imaging electron beam.

These results were emphasizing the need for a characterization method that reduces the interaction with the surface to a minimum. AFM meets exactly this requirement, especially when employed in tapping mode measurements. Being an analytical technique that interacts with the surface in a purely mechanical way, its application is ideal for samples that react very sensitively to any kind of electromagnetic irradiation. Moreover, SEM lacks the ability to visualize effects that occur specifically at the sample surface. FM-KPFM, however, is additionally capable of mapping out the local CPD between the tip and the sample surface, maintaining minimal intrusiveness.

The optimization of the synthesis conditions of a perovskite thin film for a given substrate is a very time-consuming process. Rather than achieving optimized films, the aim of this project was to connect macroscopically observable stabilization effects of different passivation agents on both MAPbI$_3$ and Cs$_{0.15}$FA$_{0.85}$PbI$_3$ thin films with the microscopically observed topography and CPD.

It is important to comprehend not only the impact a passivation strategy has on defects, but also on the morphology of the film. Solar cell performance enormously depends on the morphology of the thin film, be it due to grain size and GB density,[40] surface coverage,[41] or roughness.[42] All these factors determine cohesion of the multiply layered device and, therefore, determine the effective charge transport across all interfaces.

This study attempts to elucidate passivation mechanisms on perovskite thin films by comprehensive comparison of fundamentally different passivation strategies. In order to do so, grain-encapsulating agents (TEOS and APTES), 2D-perovskite-forming PEAI, and alkali metal iodides (RbI and KI) are used as additives in the synthesis of both MAPbI$_3$ and Cs$_{0.15}$FA$_{0.85}$PbI$_3$ films. Their degradation under ambient conditions was rigorously traced with means of UV/Vis and PL spectroscopy as well as XRD. In the second step, topography and CPD maps of the obtained films are created in order to be able to specify the observed differences in stability.

4 Results and Discussion

4.1 Precursor Solution Modification

In a recently published study, Liu et al. show that by simple addition of TEOS and water to a $Cs_{0.15}FA_{0.85}PbI_3$ perovskite precursor solution, the phase transition from the photoactive α-phase (black) in the resulting film to thermodynamically more stable, but photo-inactive δ-phase (yellow) could be significantly decelerated, yielding PSCs with 18.8% PCE and 97% PCE-retention after 1000 h ambient storage.[21]

In order to understand the occurring reaction between TEOS and water in the precursor matrix more precisely, with prospect of transferring the reaction principle to different silica precursors, kinetic studies were performed via ^{1}H-NMR and ^{29}Si-NMR spectroscopy on the native $Cs_{0.15}FA_{0.85}PbI_3$ precursor solutions (s. Section 6.5.1) as adapted from the literature, containing 1.00 M lead(II) iodide, 0.85 M formamidinium iodide (FAI), 0.15 M cesium iodide in a mixture of *N*,*N*-dimethylformamide (DMF) and dimethyl sulfoxide (DMSO).[21] As an internal standard for quantification, 0.05 M sodium 3-(trimethylsilyl)propane-1-sulfonate (DSS) was added.

4.1.1 NMR Studies of TEOS Precursor Solutions

From a mechanistical point of view, the Liu et al. suggest that upon addition of TEOS and water to the precursor solution hydrolysis of TEOS is triggered and silicate oligomers form according to the reaction shown in Scheme 4.1. Hereinafter, the different silicate species are designated in the commonly used nomenclature. M^i_X, D^i_X, T^i_X and Q^i_X refer to the number of oxygen atoms (one, two, three and four, respectively) to which the silicon atom is bound, while the superscript i denotes the number of formed Si-O-Si bridges. Furthermore, a subscript R is used for the pure precursor itself and H is used for its hydrolyzed analogs.[43]

24
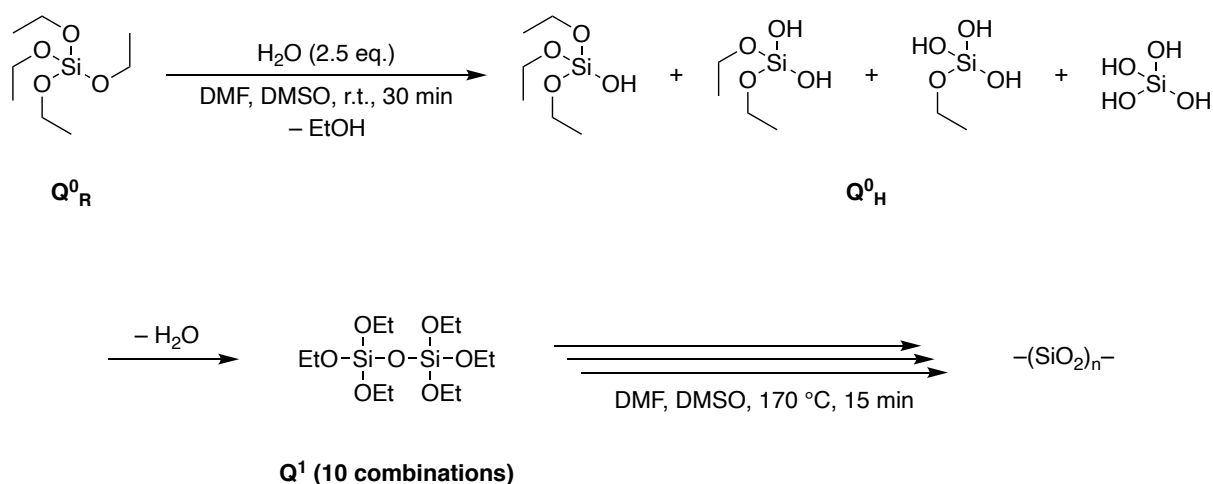
Scheme 4.1. Reaction equation of the hydrolysis of TEOS precursor via silicate oligomers to silica.

Details of the obtained spectra are shown in Figure 4.1; the full spectra are given in Figure A.1 and Figure A.2 in the appendix. At chemical shifts of 3.78-3.73 ppm and 1.17-1.13 ppm a quartet and a triplet are clearly visible, corresponding to the methylene and methyl groups, respectively, of silicon-bound ethoxy groups. CH_2 and CH_3 groups of free ethanol released during the reaction would be expected to appear slightly upfield-shifted at 3.50 ppm and 1.07 ppm, respectively, due to stronger shielding of the H-nuclei. In fact, after 20 h reaction time a quartet and a triplet started to emerge at the expected chemical shifts. According to their integral ratios, the conversion of the reaction was quantified to around 3%, demonstrating the fact that the condensation reaction of TEOS in the precursor solution at room temperature proceeded on very long timescales.

These first insights into the reaction kinetics contradict the description made by Liu et al., and suggest high temperatures around 170 °C to be essential for the TEOS hydrolysis rather than for the formation of the α-FAPbI$_3$ phase.
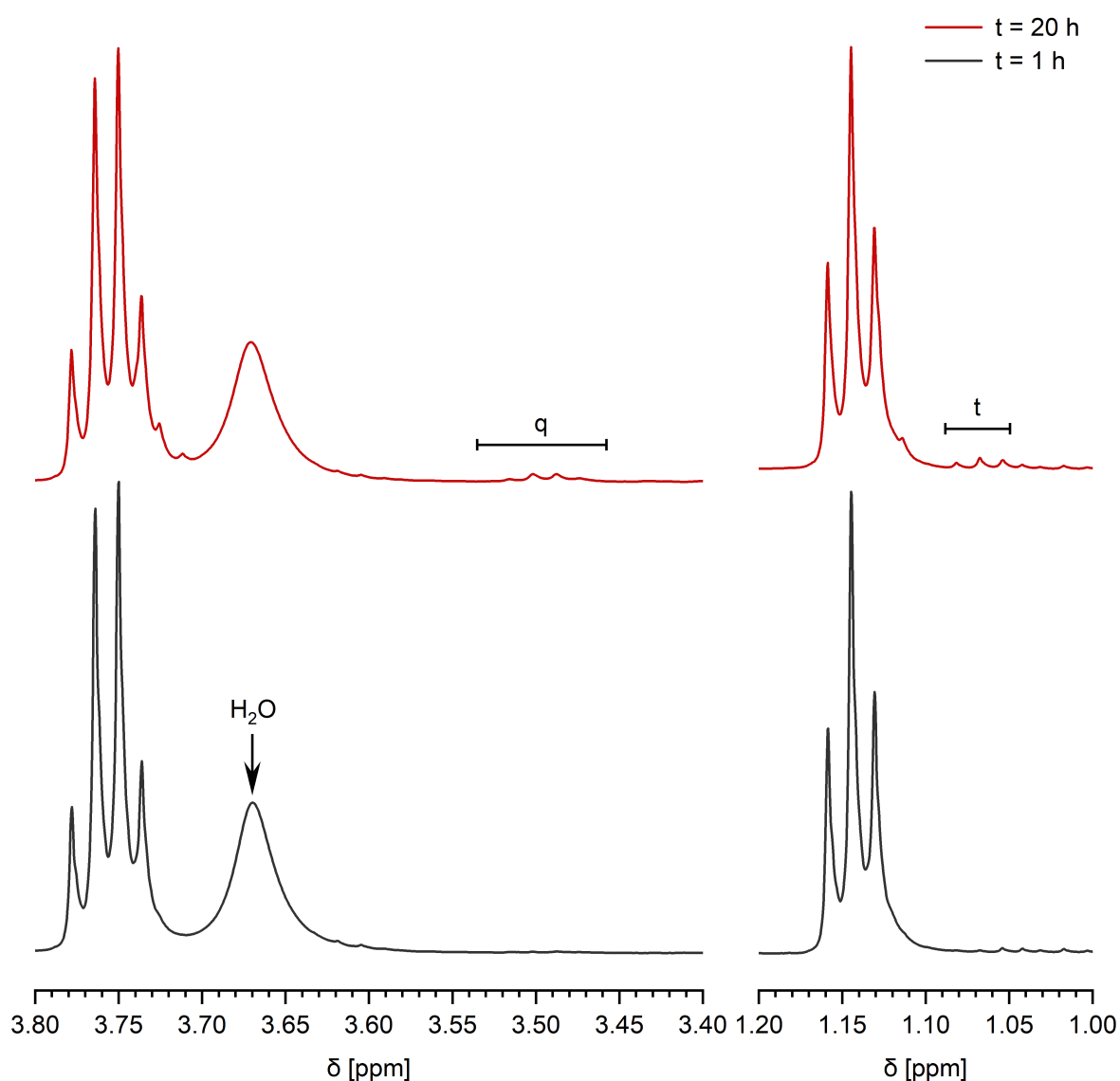
Figure 4.1. Detail of the ^{1}H-NMR spectrum of a $Cs_{0.15}FA_{0.85}PbI_3$ precursor solution containing 0.135 M TEOS and 0.3 M water after 1 h (black) and 20 h (red) reaction time at 25 °C. Peak heights are independently adjusted for optimal peak visibility.

The observations made above are confirmed via ^{29}Si-NMR spectroscopy on the same precursor solution (s. Figure 4.2). Due to the low concentration of TEOS in the precursor solution together with a naturally low abundance of the ^{29}Si nucleus (4.7%) and a small gyromagnetic ratio γ (−8.465 MHz·T^{-1}), an Insensitive Nuclei Enhanced by Polarization Transfer (INEPT) experiment was performed, with its pulse sequence transferring the polarization from methylene hydrogen nuclei to the silicon nucleus via *J*-coupling. Thus, the signal-to-noise ratio of ^{29}Si signals can be improved significantly. After 20 h reaction time, no other Si-species besides the Q^0_R monomer could be detected, confirming the assumption that the condensation polymerization, to a predominant part, takes place during the annealing of the perovskite film at temperatures of above 150 °C.
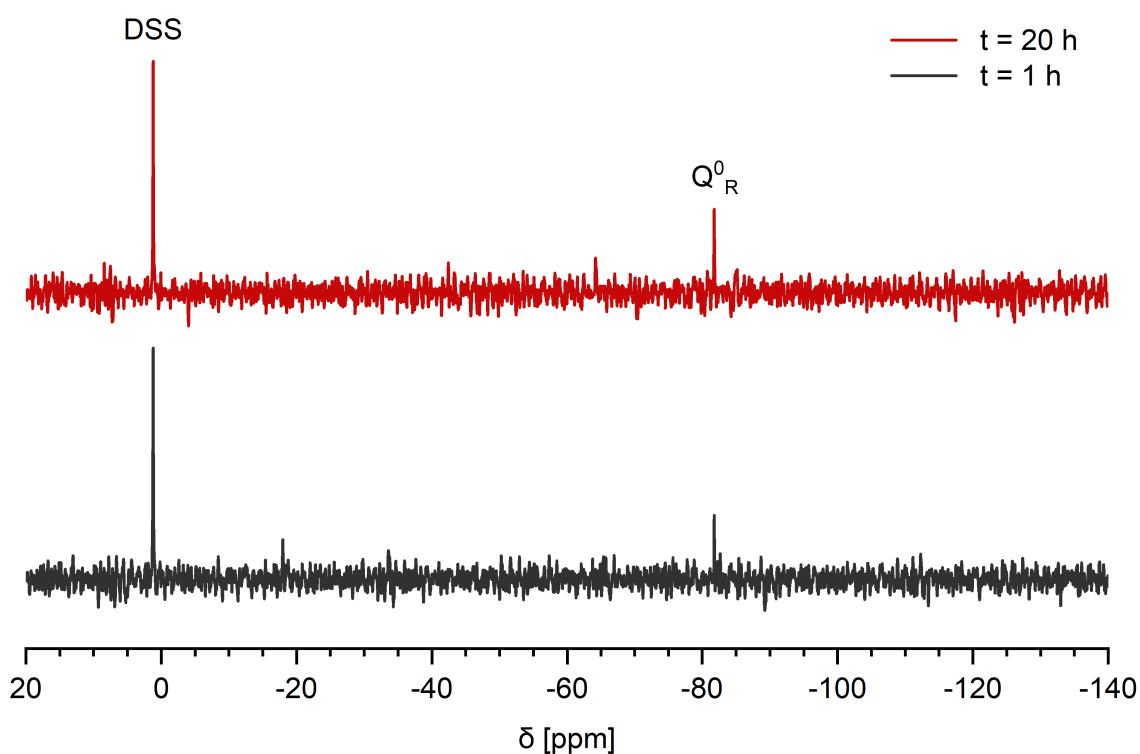
Figure 4.2. ^{29}Si-NMR spectrum (INEPT) of a $Cs_{0.15}FA_{0.85}PbI_3$ precursor solution containing 0.135 M TEOS and 0.3 M water after 1 h (black) and 20 h (red) reaction time at 25 °C.

4.1.2 NMR Studies of APTES Precursor Solutions

In order to improve the positive effects regarding the stability of the perovskite film grain encapsulation using TEOS, another silicon-based precursor was tested. By addition of APTES to the $Cs_{0.15}FA_{0.85}PbI_3$ precursor solution, we hoped that in addition to grain encapsulation upon polymerization, the free amine functionality would be able to either coordinate undercoordinated lead(II) or, in its ammonium form, coordinate iodide at the GBs of the perovskite structure and, therefore, would increase structural stability.

In the first step, an equivalent analytical strategy as described above via ^{1}H- and ^{29}Si-NMR spectroscopy was pursued in order to elucidate the mechanics of the reactions occurring in the perovskite precursor solution. Here, TEOS was simply replaced by 0.135 M APTES. The reaction expected to occur is shown in Scheme 4.2.[43]
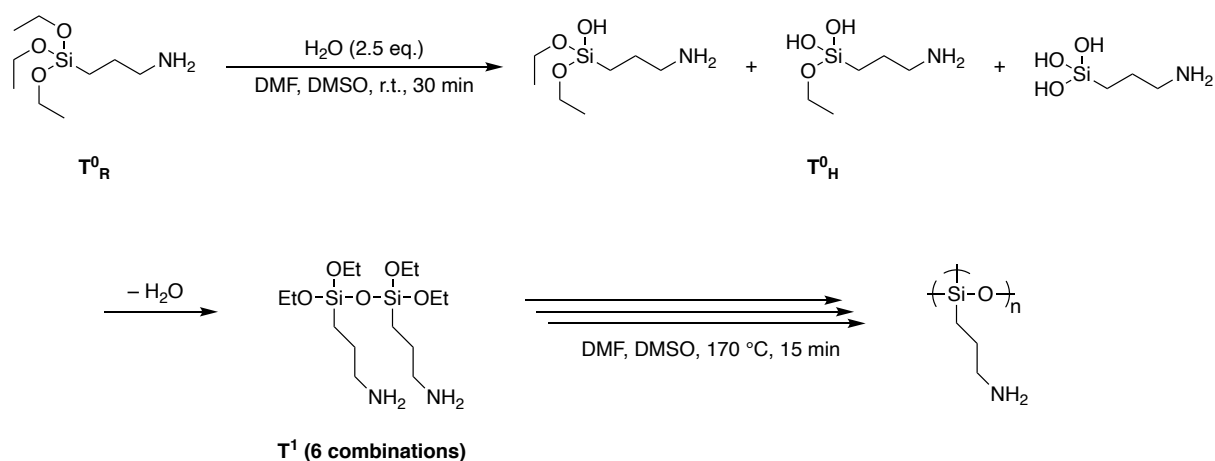
Scheme 4.2. Reaction equation of the hydrolysis of APTES precursor via oligomers to amino-functionalized organosilica.

Details of the obtained ^{1}H-NMR spectra taken 1 h and 48 h after preparation of the precursor solution are shown in Figure 4.3. The conversion of the hydrolysis of the APTES precursor to around 21% after merely 1 h reaction time could be quantified by estimating the integrals of the quartet signal at 3.53-3.46 ppm and the triplet signal at 1.09-1.04 ppm corresponding to CH$_2$- and CH$_3$-groups of free ethanol, respectively. Moreover, no water signal could be detected, showing that added water was being consumed relatively fast in the hydrolysis reaction. The monomer was entirely depleted at 48 h after the start of the reaction.
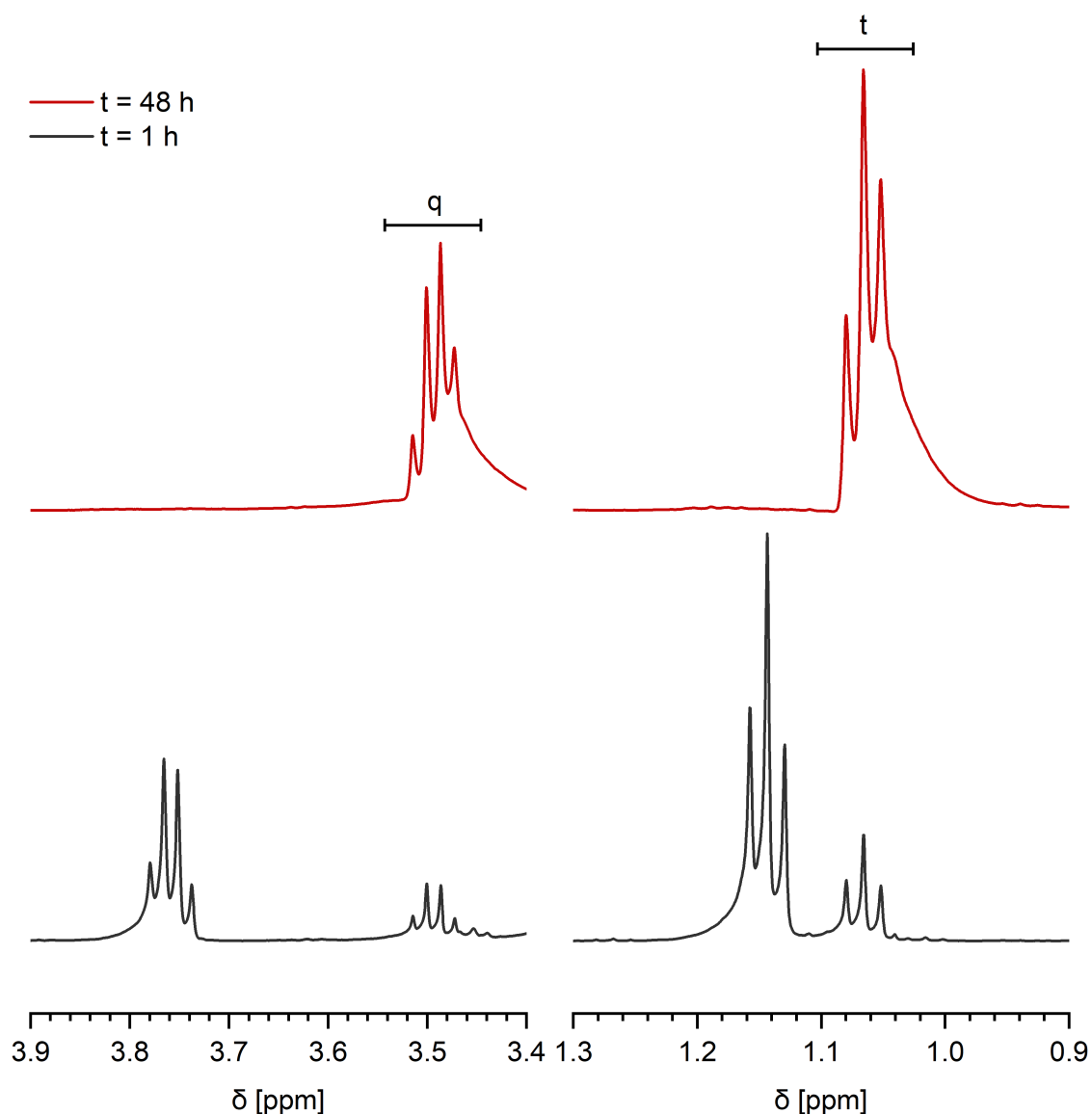
Figure 4.3. Details of the ^{1}H-NMR spectrum of a $Cs_{0.15}FA_{0.85}PbI_3$ precursor solution containing 0.135 M APTES and 0.3 M water at 1 h (black) and 48 h (red) reaction time. Peak heights are independently adjusted for optimal peak visibility.

The results of the ^{1}H-NMR experiments conformed to those of the ^{29}Si-NMR experiments. Here again, an INEPT pulse sequence was used. In the case of APTES, a larger enhancement of the ^{29}Si nucleus can be achieved compared to TEOS due to closer adjacency of the first methylene group of the propyl chain to the silicon nucleus and, therefore, larger *J*-coupling between the two. Figure 4.4 shows the progress of the reaction after three time-steps. The chemical shift of the T^0_R species at –46.07 ppm is in accordance with the literature.[43] After 20 h, the precursor was largely depleted. Instead, peaks at –57.05 ppm and –68.43 ppm started to emerge, corresponding to the linearly bridged T^2-trimer and T^3-tetramer, respectively. Note that the

bridged T^1-dimer was not visible in any of the spectra, presumably due to its short-livedness.[43] The decrease in peak height for the signals above –55 ppm can be explained by the fact that *J*-coupling between the ^{29}Si nucleus and the methylene hydrogen nuclei decreases with the addition of new monomers. In addition, the number of possible species increases with the addition of every monomer simply for combinatory reasons. In alignment with ^1H-NMR results, the T^0 monomer was fully depleted after 48 h. Additionally, a diversification of the T^3 signal could be observed as well as a new signal at –66.60 ppm which may be assigned to the distinct, pyramidally linked T^3-tetramer.
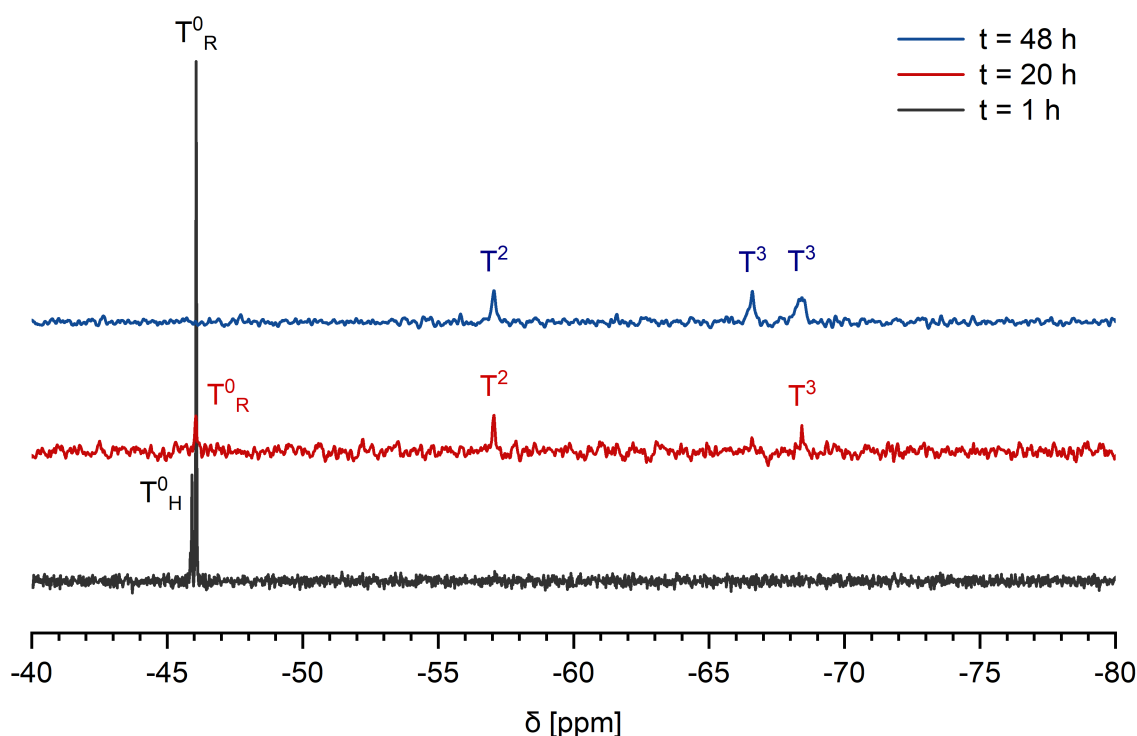
Figure 4.4.   Detail of the ^{29}Si-NMR spectrum (INEPT) of a $Cs_{0.15}FA_{0.85}PbI_3$ precursor solution containing 0.135 M APTES and 0.3 M water after 1 h (black), 20 h (red) and 48 h (blue) at 25 °C.

In summary, the ^1H- and ^{29}Si-NMR experiments proved that the hydrolysis of APTES proceeds much faster compared to TEOS in the same matrix. For this reason, every precursor solution with APTES-additive was only ever prepared immediately before thin film synthesis. Furthermore, no water was added to the solution since ^1H-NMR spectra of the used solvents (s. Figure A.10 and Figure A.11) showed trace amounts of water (0.018 mol·L^{-1} in a mixture of DMF/DMSO 5:1 v/v corresponding to 320 ppm, determined via integral ratios), presumably enough to start the condensation polymerization.

4.2 Stability Studies

Films composed of both MAPbI$_3$ and Cs$_{0.15}$FA$_{0.85}$PbI$_3$ were synthesized in a one-step solution deposition on glass. The considered additives, namely, grain-encapsulating agents TEOS and APTES, 2D-perovskite-forming PEAI and alkali metal iodides RbI and KI, were each added to the precursor solutions separately. The macroscopic degradation behavior of each obtained film under ambient conditions was photographically documented as well as quantified by ultraviolet-visible spectroscopy (UV/Vis), photoluminescence (PL) spectroscopy and XRD. That way, a full picture about optical properties in correlation with phase information can be drawn. Note that XRD analysis on multiple-phase systems in thin films entails the challenge of consistently assigning the diffraction peaks by matching throughout the entire scanned range, since certain reflections may be absent, and others may be overpronounced due to preferred crystal orientations within the film.

The high incident energies used in XRD (around 8 keV) accelerated the degradation process compared to bare degradation under ambient conditions. Therefore, the time-steps of the obtained absorption spectra are not necessarily conferrable to the time-steps of the X-ray diffractograms. Nevertheless, equivalent degradation processes are expected to occur, so that XRD provides information on the phases compounding the absorption spectra. Note that, in some cases, the films start to degrade already during the 20 min measuring time of the first scan, so that degradation peaks may appear in the first diffractogram.

In addition, the direct bandgaps (E_g) as well as the Urbach energies (E_U) were determined, as listed in Table 4.1 and Table 4.2 for MAPbI$_3$ and Cs$_{0.15}$FA$_{0.85}$PbI$_3$, respectively. In order to do so, the Tauc protocol described in Section 6.6.3 was applied to the initial absorption edge in each absorption spectrum at t_0.

4.2.1 Stability of MAPbI₃ Films

(a) General Observations

The UV/Vis spectra including the PL peak, XRD patterns as well as a photographic documentation of the degradation of MAPbI₃ films with respective additives (pure film, TEOS, APTES, PEAI, RbI, KI) are given in Figure 4.5 to Figure 4.10. All XRD patterns show reflections of tetragonal β-MAPbI₃ (ICSD collection code 241478, space group I4/mcm, lattice constant a = 8.8548 Å, c = 12.6592 Å, gray bars in Figure 4.5B to Figure 4.10B). Over the time of the measurement, reflections matching hexagonal PbI₂ (ICSD collection code 24263, space group $P6_3mc$, lattice constant a = 4.5570 Å, c = 13.9580 Å, pink bars in Figure 4.5B to Figure 4.10B) emerge, most easily discernible by the (002)-reflection at 2θ = 12.7°. The deviations from the reference pattern peak intensities imply that the formation of PbI₂ occurred in a preferred (002)-orientation. Simultaneously, all UV/Vis spectra show an emerging absorption at 494 nm which was, therefore, assigned to PbI₂. These results are in agreement with the general hypothesis that an excess of PbI₂ develops due to loss of methylamine.[17][18] Determined direct bandgap energies and Urbach energies for the passivated MAPbI₃ films are given in Table 4.1.

Table 4.1. Direct bandgap energies and Urbach energies of each MAPbI₃ perovskite film determined via Tauc method on the first edge in the absorption spectra at $t = 0$ h.

Perovskite Composition	Passivating Agent	E_g [eV]	E_U [meV]
MAPbI₃	-	1.61 ± 0.01	37.8 ± 0.2
MAPbI₃	TEOS	1.59 ± 0.01	52.5 ± 0.4
MAPbI₃	APTES	1.62 ± 0.01	59.0 ± 0.6
MAPbI₃	PEAI	1.59 ± 0.01	58.7 ± 0.4
MAPbI₃	RbI	1.58 ± 0.01	67.6 ± 0.5
MAPbI₃	KI	1.60 ± 0.01	42.9 ± 0.3

(b) Non-Passivated MAPbI₃ Films

MAPbI₃ films showed considerable stability at ambient conditions. Only at 48 h, significant signs of degradation become visible, indicated by the pronounced PbI₂-absorption in Figure 4.5A. The bandgap of (1.61 ± 0.01) eV determined from the PL peak position at 771 nm coincides with the bandgap determined via Tauc plot.

The so-called Urbach tail gives an estimation of the electronic and structural disorder in a semiconductor and the presence of trap states.[44] The smaller the Urbach energy, the smaller the amount of sub-bandgap absorption, thus indicating fewer trap states. The characteristic energy of the Urbach tail was determined to be (37.8 ± 0.2) meV in this system, which is about double the value that was observed by other groups.[44] Thus, this system showed larger defect density to begin with. However, the structural disorder is strongly dependent on the parameters of the thin film preparation. The relatively large value in this system indicates that the film fabrication needs to be optimized further, but it can be used as a reference value for comparison with the passivated films, nevertheless.
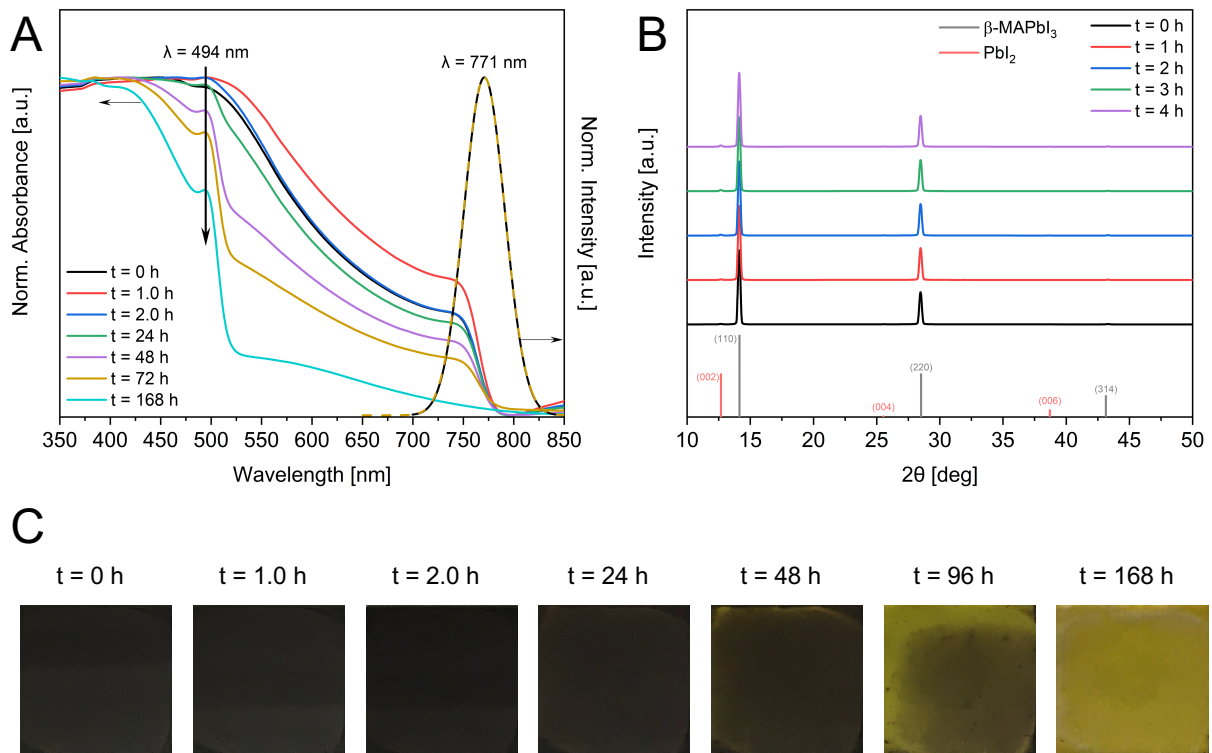

Figure 4.5. (A) Normalized UV/Vis and PL spectra of a non-passivated MAPbI₃ thin film recorded over the course of one week, (B) XRD patterns recorded in time-steps of 1.0 h, (C) photographic record of the degrading films.

(c) TEOS-Encapsulated MAPbI₃ Films

The addition of grain-encapsulating TEOS did not improve, but rather deteriorate the stability of the MAPbI$_3$ film under ambient conditions, as can be concluded from the clear emergence of the PbI$_2$ absorption at 24 h (s. Figure 4.6A). This goes along with a strong increase in Urbach energy to (52.5 ± 0.4) meV, indicating a higher density of intra-bandgap states due to a stronger disordering of the crystal lattice in the encapsulated film. Grain encapsulation using TEOS was, therefore, insufficient in both retaining methylamine within the structure and in reducing sub-bandgap absorption. Due to its hydrophilicity and suspected porosity, it might even support the binding of water from the atmosphere and, that way, promote the humidity-accelerated degradation pathway.
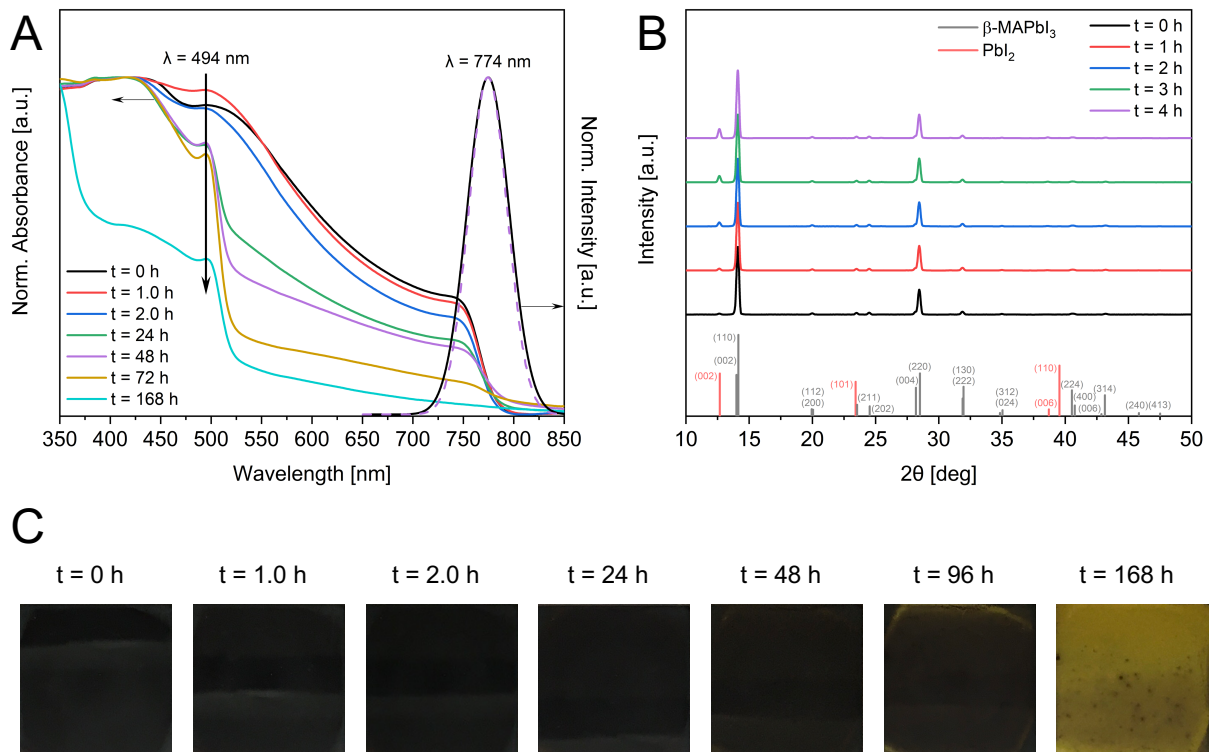

Figure 4.6. (A) Normalized UV/Vis and PL spectra of a TEOS-encapsulated MAPbI$_3$ thin film recorded over the course of one week, (B) XRD patterns recorded in time-steps of 1.0 h, (C) photographic record of the degrading films.

(d) APTES-Encapsulated MAPbI₃ Films

Using APTES as an encapsulating agent for perovskite films has never been done before. APTES has been shown to improve the stability of MAPbI$_3$ nanocrystals by acting as a capping agent protecting the perovskite against external protic solvents.[45] Regarding perovskite thin film stability, addition of APTES yields the most auspicious enhancement. In the UV/Vis spectra (s. Figure 4.7A), the films show signs of degradation only at 48 h storage. However, the PL absorption shifts to a lower wavelength (758 nm) compared to all the other samples, which show PL peaks at around 774 nm. This is synonymous with an increased bandgap of (1.62 ± 0.01) eV, determined via Tauc plot. The shift can be explained by quantum confinement of the perovskite grains due to a significantly smaller particle size. It seems, therefore, plausible that the ammonium functionality of the APTES polymer acts as a capping agent for the growing perovskite crystals during annealing. Moreover, the diffraction pattern in Figure 4.7B exhibits significantly broadened lines, quantified by their full width at half maximum (FWHM) value.

The FWHM of a peak in XRD is largely determined by the convolution of three contributions: The instrument response, the grain size (Scherrer broadening) and microstrain.[46] Microstrain is a consequence of variations of the lattice parameters due to structural defects such as dislocations, vacancies and interstitials, while grain size effects will only be significant at crystallite sizes of below 100 nm.[46] In fact, AFM topography imaging, which will be discussed in more detail below, revealed a strong reduction in grain size in the APTES-encapsulated MAPbI$_3$ film (s. Figure A.12A) to the range of below 100 nm. This is reflected in the line broadening of the (110)-reflection of β-MAPbI$_3$ to 0.41° as compared to 0.22° for the same reflection in the pure film. Furthermore, it is suggested that the ammonium group also prevents the PbI$_2$ crystals formed during degradation from growing large, indicated by an even larger broadening of the PbI$_2$ (002)-reflection at 12.7° to a FWHM of 0.56° (s. Figure 4.7B), which is, in turn, significantly higher than 0.41° for the (110)-reflection of β-MAPbI$_3$. Part of the line broadening can also be explained with APTES introducing microstrain due to a higher degree of structural disorder. This assumption is consistent with an increase in Urbach energy to (59.0 ± 0.6) meV compared to (37.8 ± 0.2) meV in the pure film. However, optimizing the amount of APTES additive may mitigate this increase in Urbach energy as well as the reduction in grain size.

As a proof-of-concept, we showed that APTES is able to function as an encapsulating agent superior to TEOS. Further enhancement of the stabilizing effect might be conceivable by substituting one of the ethoxy groups with a methyl or phenyl group in order to enhance the hydrophobicity of the surface while still maintaining the ability to (linearly) polymerize.
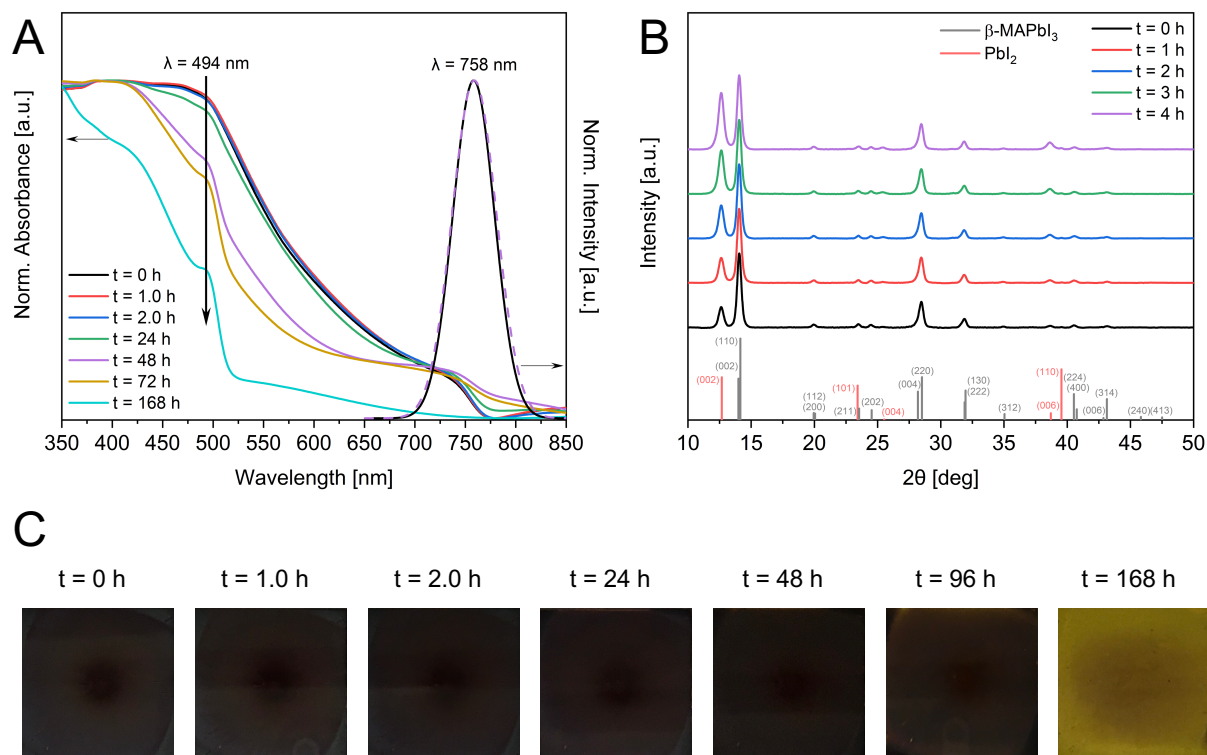

Figure 4.7. (A) Normalized UV/Vis and PL spectra of an APTES-encapsulated MAPbI₃ thin film recorded over the course of one week, (B) XRD patterns recorded in time-steps of 1.0 h, (C) photographic record of the degrading films.

(e) PEAI-Passivated MAPbI₃ Films

In our experiments, MAPbI$_3$ thin films containing PEAI did not show superior stability compared to the pure films. Although 2D-passivation is believed to increase the hydrophobicity of the film,[26] it does not prevent methylamine to permeate through the hydrophobic layer. Interestingly, an increased FWHM of 0.35° of the PbI$_2$ (002)-reflection compared to 0.24° of the β-MAPbI$_3$ (110)-reflection is observed again in the XRD patterns in Figure 4.8B. This suggests a mechanistic relation of the APTES and PEAI-passivation mechanism, pointing towards ammonium ions acting as capping agents for the perovskite as well as for the formed PbI$_2$ in both cases. As a consequence of the 3D-2D-hybrid structure, Urbach energies are expected to increase.[47] In fact, they still show a degree of structural disorder that is yet lower than in the APTES-encapsulated film. The lower defect density found in PEA$^+$-passivated films may imply a smaller degree of microstrain introduced by the 2D-layer as compared to the structurally more rigid, glassy APTES polymer.
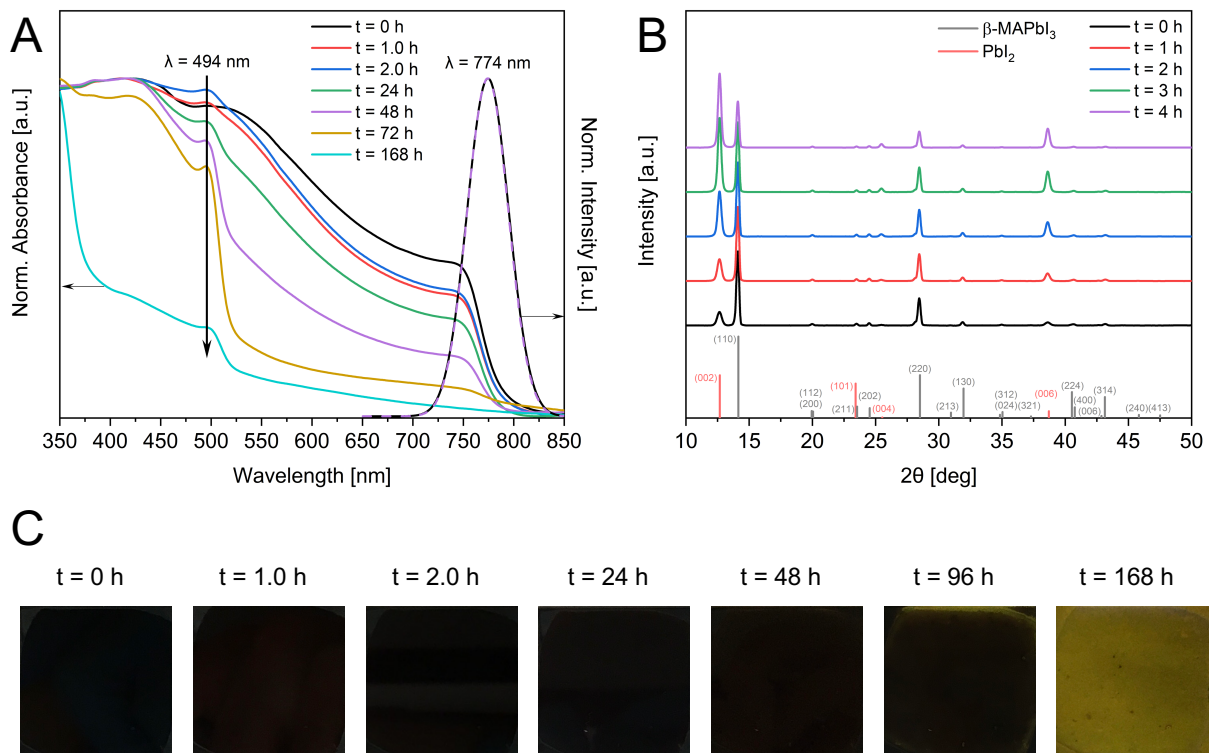

Figure 4.8. (A) Normalized UV/Vis and PL spectra of an PEAI-passivated MAPbI$_3$ thin film recorded over the course of one week, (B) XRD patterns recorded in time-steps of 1.0 h, (C) photographic record of the degrading films.

(f) RbI- and KI-Passivated MAPbI$_3$ Films

Addition of inorganic salts like RbI and KI did not improve MAPbI$_3$ film stability under ambient conditions, as is apparent from the UV/Vis spectra in Figure 4.9A and Figure 4.10A. However, although the PbI$_2$ absorption is clearly visible in both spectra after 24 h, no PbI$_2$ phase is detected in via XRD (s. Figure 4.9B and Figure 4.10B) at shorter time periods. Instead of PbI$_2$, intermediate phases are formed, indicated by the reflections at 11.5° (asterisk in Figure 4.9B) and at 15.8°, 23.8°, 29.0°, 39.0°, 40.2° and 48.7° (asterisks in Figure 4.10B) which did not match any known phase. The presence of these unassigned XRD reflections coincides with the UV/Vis absorptions at 424 nm for RbI-passivated films and 408 nm for KI-passivated films. These absorptions cannot be observed in the UV/Vis spectra of any other MAPbI$_3$ film. For the RbI-passivated sample a decreasing intensity of the intermediate phase is observed in the XRD pattern while for the KI-passivated sample the contrary is the case. This goes along with a slight redshift in the PL for the RbI sample and a blueshift for the KI sample.

One has to assume two distinct phases in each case. It can by hypothesized that due to the high loading of alkali iodide of 20 mol% with respect to the A-cation, a certain degree of alkali metal cations is able to be incorporated into the perovskite lattice at interstitial sites, as it has been suggested before.[48] If an initial incorporation of the Rb$^+$ ion is assumed, which is also consistent with the high Urbach energy of (67.6 ± 0.5) meV since the presence of interstitials is synonymous with a higher structural disorder, the data suggests that MAPbI$_3$ expels these surplus Rb$^+$ ions causing them to segregate to the separate phase. This process is consistent with the XRD result, if one interprets the β-MAPbI$_3$-(110)-reflection in the XRD pattern (s. Figure 4.9B) as increasing rather than the unassigned reflection at 11.5° as decreasing. The MAPbI$_3$ film thus relaxes structurally, shifting the PL absorption and bandgap energies closer to the values of the pure reference film (s. Figure 4.9A).[49]

The contrary would be the case for the KI-passivated film. However, an initial phase segregation is observed neither in the UV/Vis spectrum (s. Figure 4.10A) nor in the XRD pattern (s. Figure 4.10). It can be hypothesized that the K^+ ions are initially located on the surface and the GBs,[48] as also suggested by the relatively small Urbach energy of (42.9 ± 0.3) meV, but then diffuse due to its small size into the perovskite lattice,[50] located at interstitials and shifting the PL peak to smaller wavelengths, as well as agglomerate in a mixed phase, giving rise to the unassigned reflections at 15.8°, 23.8°, 29.0°, 39.0°, 40.2° and 48.7°. Although both being alkali halides, RbI and KI show contrary behavior regarding grain passivation in MAPbI$_3$ films. Identification of the nature of the respective second phases would be needed in order to verify the assumptions made.
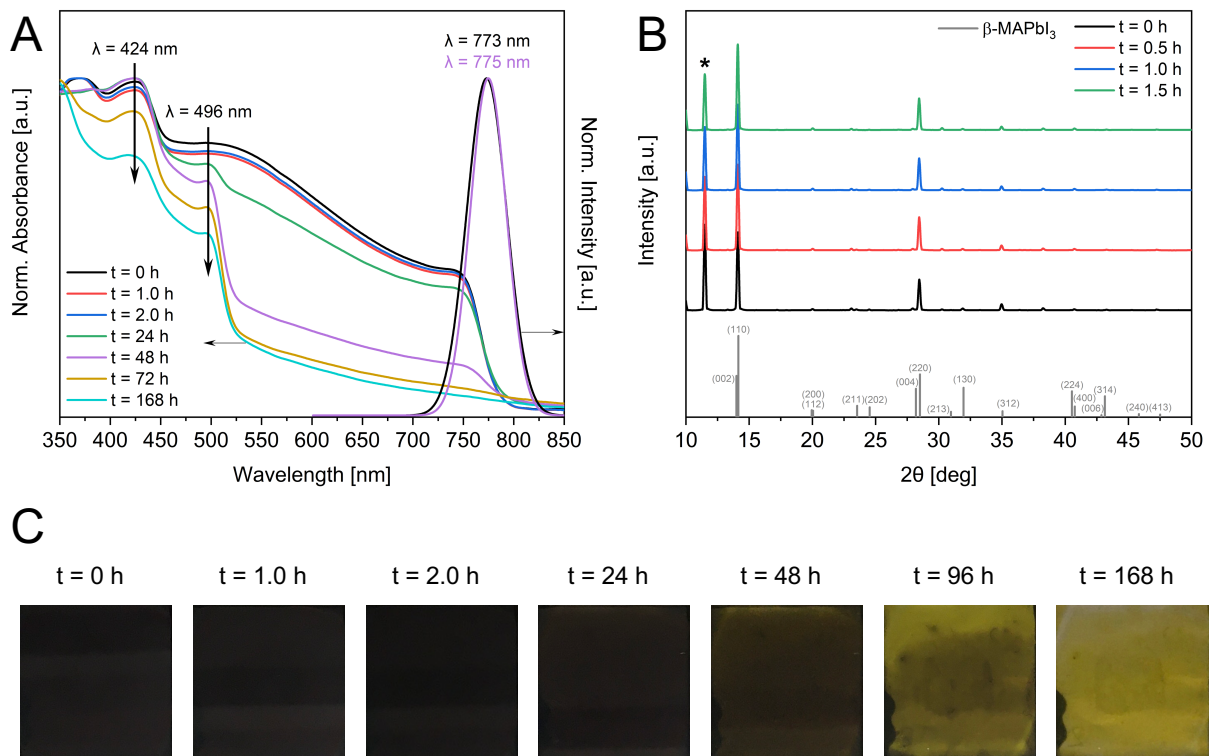

Figure 4.9. (A) Normalized UV/Vis and PL spectra of a RbI-passivated MAPbI$_3$ thin film recorded over the course of one week, (B) XRD patterns recorded in time-steps of 0.5 h, (C) photographic record of the degrading films.

Figure 4.10. (A) Normalized UV/Vis and PL spectra of a KI-passivated MAPbI$_3$ thin film recorded over the course of one week, (B) XRD patterns recorded in time-steps of 1.0 h, (C) photographic record of the degrading films.
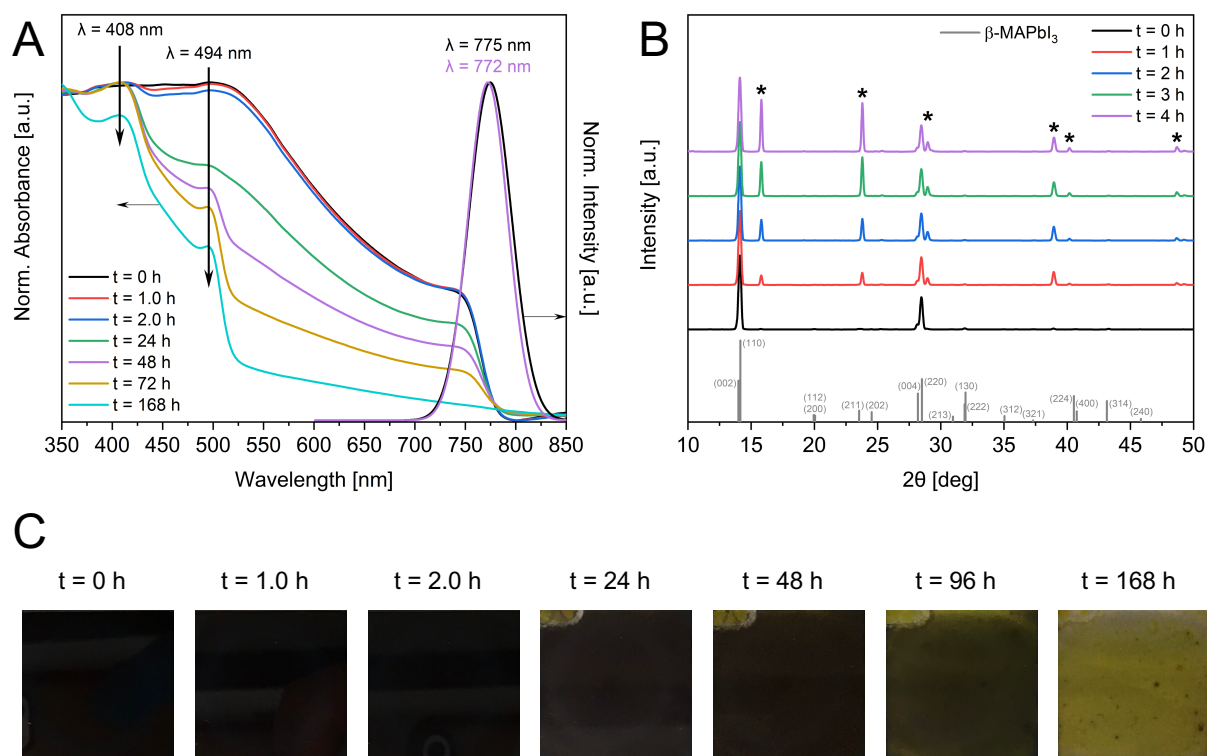
(g) Interim Conclusion

In this part of the study, the macroscopically observed stability of modified MAPbI$_3$ thin films was quantified via UV/Vis and PL spectroscopy as well as XRD. The highest stabilizing effect was obtained in an encapsulation-approach using APTES as an additive. Although APTES reduced the grain size and increased the Urbach energy, further optimization may lead to a beneficial compromise between stability and performance enhancement. Moreover, it opens the path to further functionalization of the surface such as hydrophobization.

4.2.2 Stability of $Cs_{0.15}FA_{0.85}PbI_3$ Films

(a) General Observations

The $Cs_{0.15}FA_{0.85}PbI_3$ films show a characteristic absorption edge in UV/Vis spectra at 795 nm (s. Figure 4.11A to Figure 4.16A), corresponding to the trigonal α-FAPbI$_3$ phase (COD entry no. 4335631, space group $P3m1$, lattice constant a = 8.9817 Å, c = 11.0060 Å, dark gray in Figure 4.11B to Figure 4.16B). The absorption at 379 nm is assigned to hexagonal δ-FAPbI$_3$ since it coincides with the emergence of the respective reflections in XRD (COD entry no. 4335640, space group $P6_3mc$, lattice constant a = 8.6603 Å, c = 7.9022 Å, yellow in Figure 4.11B-Figure 4.16B), most prominently shown by the (100)-reflection at $2\theta = 11.8°$. Direct bandgap energies as well as Urbach energies for the $Cs_{0.15}FA_{0.85}PbI_3$ films are listed in Table 4.2.

Table 4.2. Direct bandgap energies and Urbach energies of each $Cs_{0.15}FA_{0.85}PbI_3$ perovskite film determined via Tauc method on the first edge in the absorption spectra at $t = 0$ h.

Perovskite Composition	Passivating Agent	E_g [eV]	E_U [meV]
$Cs_{0.15}FA_{0.85}PbI_3$	–	1.55 ± 0.01	52.3 ± 0.5
$Cs_{0.15}FA_{0.85}PbI_3$	TEOS	1.55 ± 0.01	51.2 ± 0.4
$Cs_{0.15}FA_{0.85}PbI_3$	APTES	1.55 ± 0.01	68.1 ± 0.6
$Cs_{0.15}FA_{0.85}PbI_3$	PEAI	1.55 ± 0.01	52.2 ± 0.5
$Cs_{0.15}FA_{0.85}PbI_3$	RbI	1.52 ± 0.01	67.7 ± 0.5
$Cs_{0.15}FA_{0.85}PbI_3$	KI	1.54 ± 0.01	57.9 ± 0.5

(b) Non-Passivated $Cs_{0.15}FA_{0.85}PbI_3$ Films

The $Cs_{0.15}FA_{0.85}PbI_3$ film without additives exhibited significant structural instability. As apparent from the UV/Vis spectrum in Figure 4.11A and confirmed by the XRD patterns in Figure 4.11B, the active α-phase is practically entirely converted to photoinactive δ-phase within 2 h of ambient storage. The Urbach energy of (52.3 ± 0.5) meV is, again, significantly larger than Urbach energies observed by other groups of down to 15 meV, stressing the need for further optimization of the deposition parameters.[51]

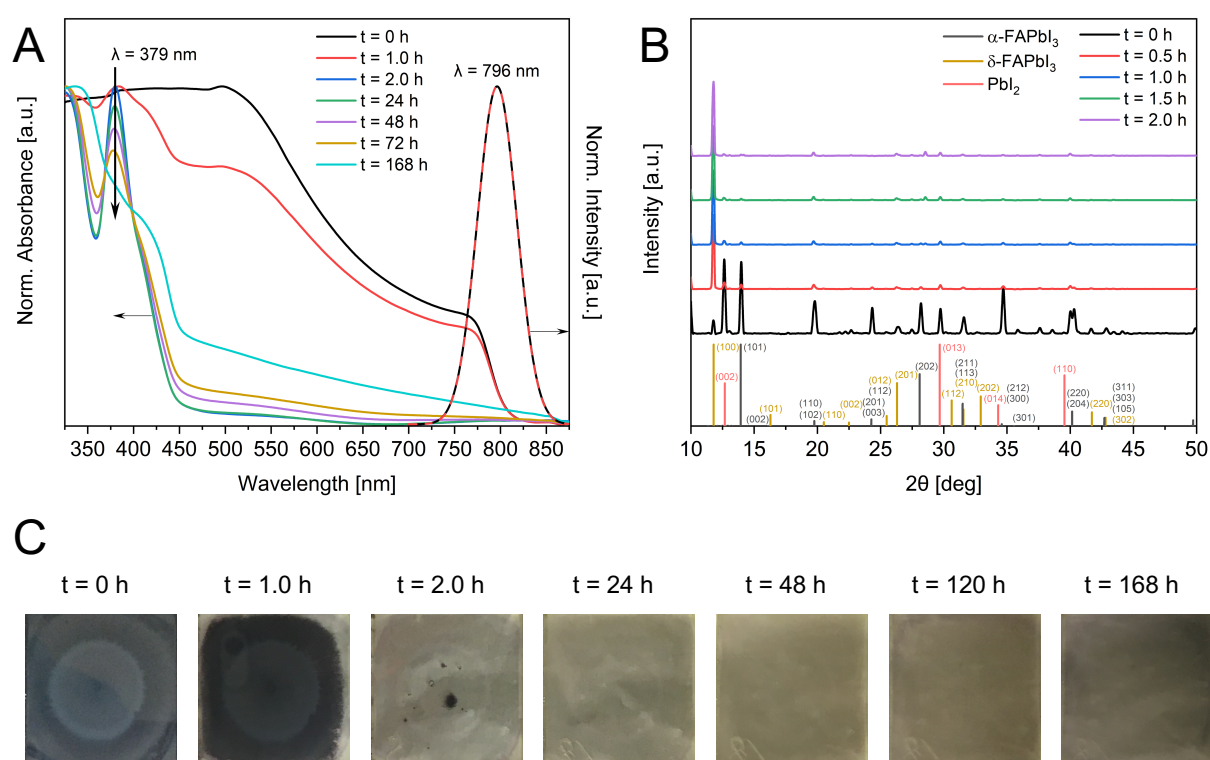

Figure 4.11. (A) Normalized UV/Vis and PL spectra of a non-passivated $Cs_{0.15}FA_{0.85}PbI_3$ thin film recorded over the course of one week, (B) XRD patterns recorded in time-steps of 0.5 h, (C) photographic record of the degrading films.

(c) TEOS-Encapsulated $Cs_{0.15}FA_{0.85}PbI_3$ Films

In our experiments, the addition of TEOS to the precursor solution decreased the stability of the resulting film in comparison to the non-passivated sample. This calls into question the results of Liu et al., who claim decelerated degradation in their films, explaining this by enhanced phase stability by silica grain encapsulation based on results of DFT-calculations[21] Note that the photographs in Figure 4.12C were taken on aluminum foil and that the substrates became entirely transparent. The XRD pattern in Figure 4.12B implies very rapid degradation since no characteristic (101)-reflection of α-FAPbI$_3$ at 13.9° could be captured. One reason for the observed decrease in phase stability may be the hydrophilicity of silica, binding atmospheric water and, thus, feeding into the water-mediated degradation mechanism for FAPbI$_3$ films instead of excluding water.[15]

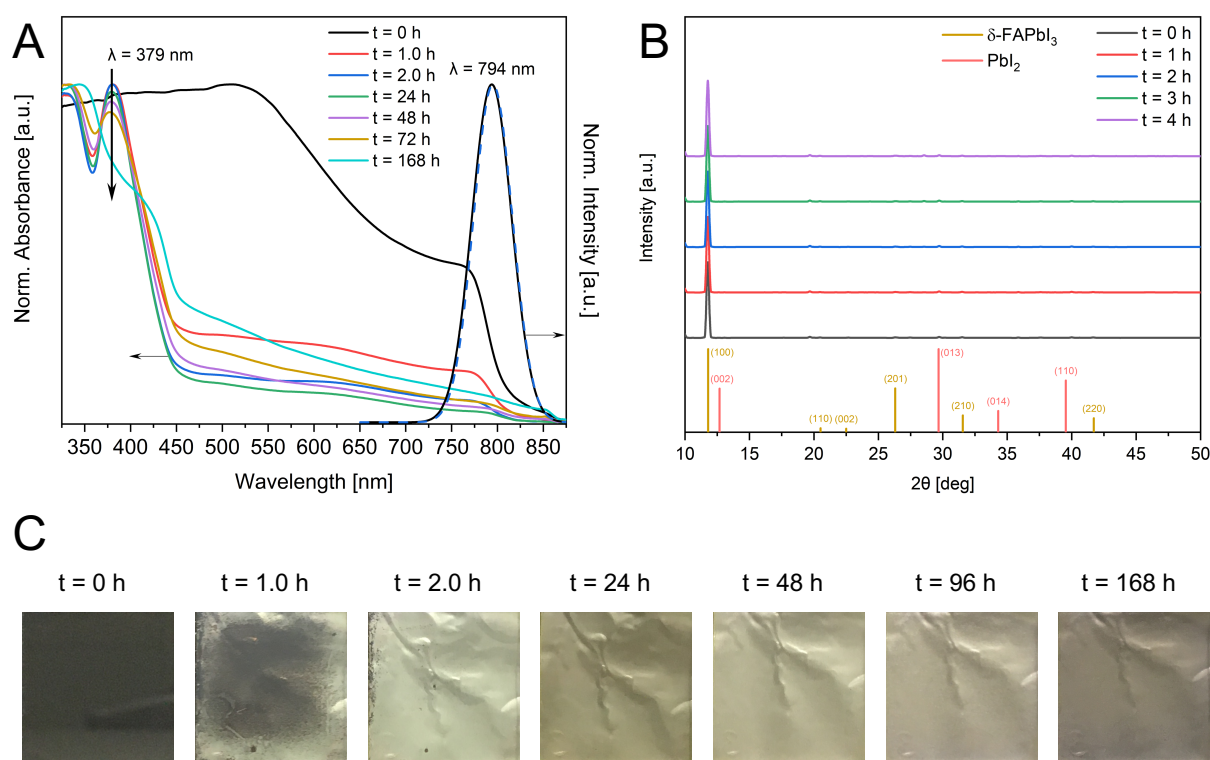**Figure 4.12.** (A) Normalized UV/Vis and PL spectra of a TEOS-encapsulated $Cs_{0.15}FA_{0.85}PbI_3$ thin film recorded over the course of one week, (B) XRD patterns recorded in time-steps of 1.0 h, (C) photographic record of the degrading films.

(d) APTES-Encapsulated $Cs_{0.15}FA_{0.85}PbI_3$ Films

Applying APTES as an encapsulating agent, however, the film stability could be dramatically increased. The UV/Vis spectrum (s. Figure 4.13A) does not show any considerable changes in the film composition within three days of ambient storage. Even after one week, no δ-FAPbI$_3$ absorption can be detected. Instead, an absorption at 345 nm shapes out, which indicates a different pathway of degradation than in the other FAPbI$_3$ samples. The XRD-pattern in Figure 4.13B, shows all the relevant α-FAPbI$_3$ reflections, although the (100)-reflection is largely overpronounced. This supports the hypothesis from Section 4.2.1 of the APTES polymer acting as a capping agent to the perovskite, leading to a strongly oriented growth of the α-FAPbI$_3$ crystals, with the (100)-plane being overrepresented.

In Section 4.2.1, XRD line broadening was associated with a reduction in grain size as well as introduced microstrain.[46] In an analogous manner, an increase in FWHM of the (101)-reflection of α-FAPbI$_3$ from 0.18° in the reference sample to 0.28° can be observed in Figure 4.13B. The reason for the enhanced stability at ambient conditions can therefore be found in this reduction in crystallite size: Due to a large surface-area-to-volume ratio a compressive strain is induced in the crystal lattice.[52] Since the δ-FAPbI$_3$ unit cell occupies a larger volume than the α-phase unit cell, the phase transition via $[PbI_6]^{4-}$ octahedral tilting is inhibited, providing ambient stability.[52] However, the increased stability comes at the price of a higher probability of trap states at surface defects, due to the enhanced surface-area-to-volume ratio.[52] This fact is also reflected in the increase of Urbach energy to (68.1 ± 0.6) meV compared to (52.3 ± 0.5) meV in the reference sample.

The APTES-encapsulated sample conspicuously shows that, in additive engineering, there is a tradeoff between the δ-phase stability and the introduction of defect states. Careful adjustment of the added amount of encapsulating agent is therefore required in order to find an optimal compromise between the two.
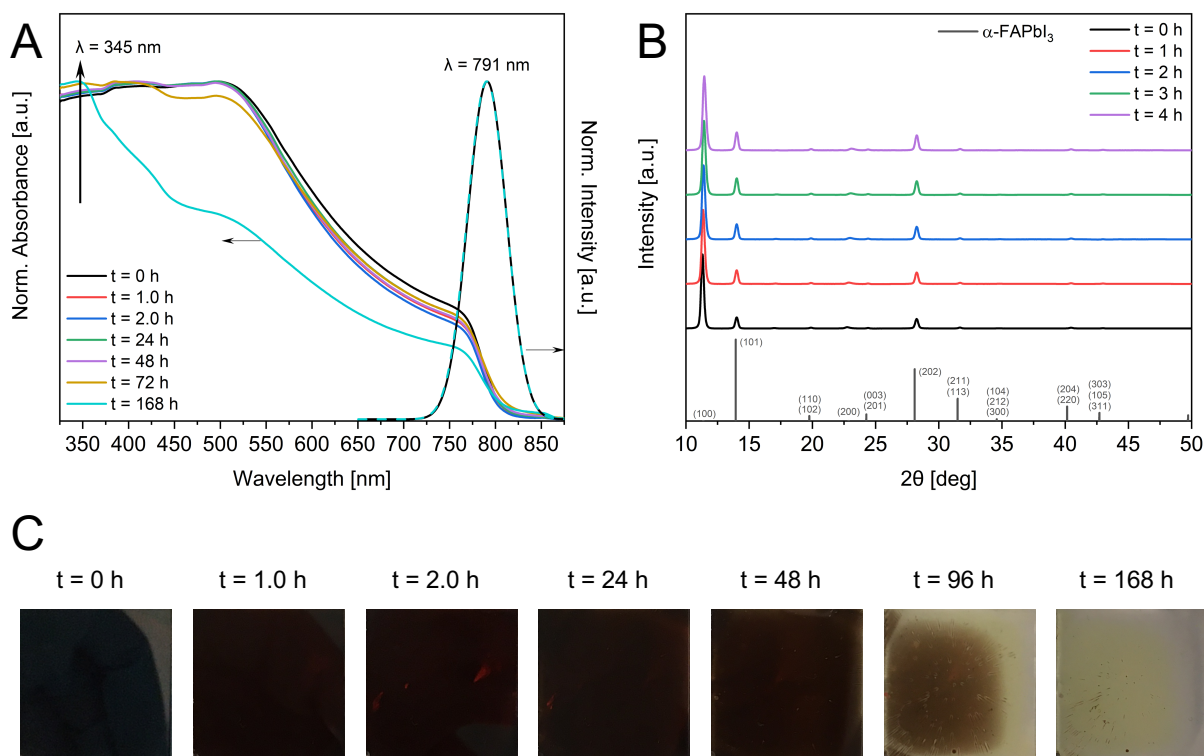
Figure 4.13. (A) Normalized UV/Vis and PL spectra of an APTES-encapsulated $Cs_{0.15}FA_{0.85}PbI_3$ thin film recorded over the course of one week, (B) XRD patterns recorded in time-steps of 1.0 h, (C) photographic record of the degrading films.

(e) PEAI-Passivated $Cs_{0.15}FA_{0.85}PbI_3$ Films

A similarly strong effect on stabilization could be achieved by PEAI-passivation. The XRD patterns in Figure 4.14B does not exhibit any δ-FAPbI$_3$ or PbI$_2$ reflections indicative of degradation. As discussed in Section 1.3, the phenyl groups of the PEA$^+$ ion increase the hydrophobicity of the film.[26] In contrast to MAPbI$_3$, however, the speed of degradation of FAPbI$_3$ films is not mainly determined by the loss of A-cations but the phase transition facilitated by humidity. Therefore, it is plausible to assume that the hydrophobic layer of the Ruddlesden-Popper phase assists in reducing the contact with water and, thereby, contributing to the observed ambient stability without any significant changes up until 24 h of storage (s. Figure 4.14A) in UV/Vis.
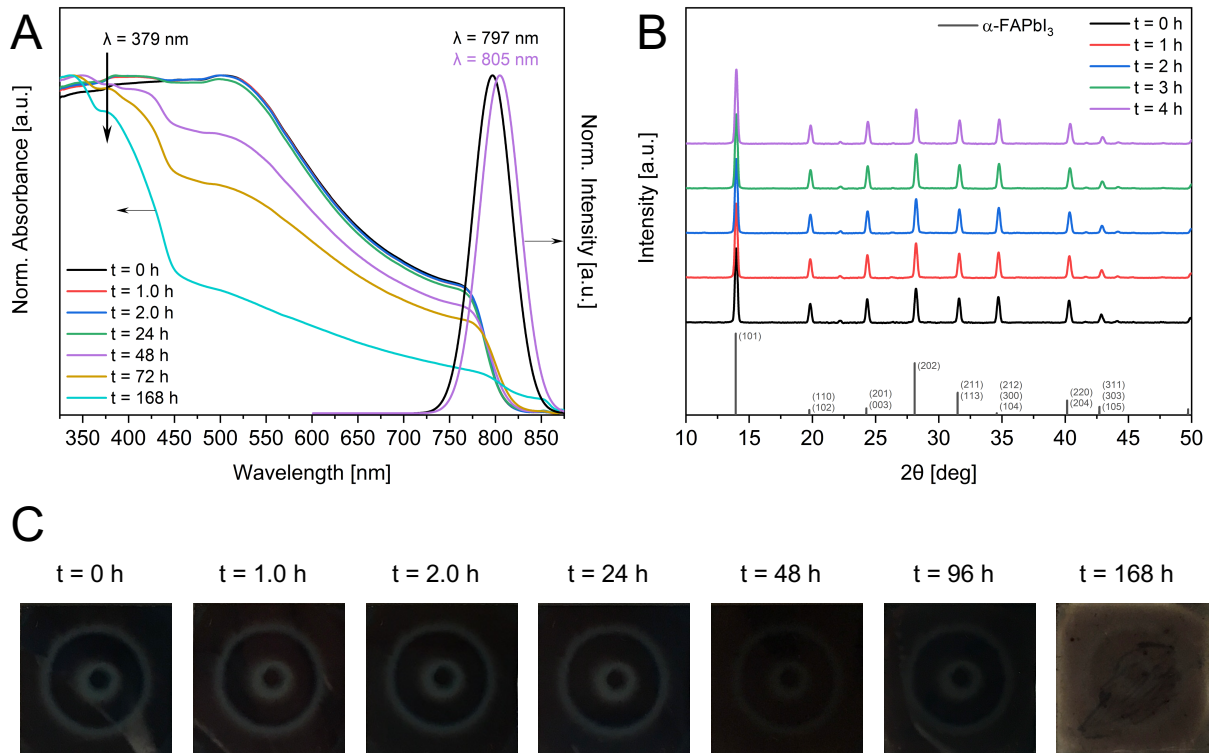
Figure 4.14. (A) Normalized UV/Vis and PL spectra of a PEAI-passivated $Cs_{0.15}FA_{0.85}PbI_3$ thin film recorded over the course of one week, (B) XRD patterns recorded in time-steps of 1.0 h, (C) photographic record of the degrading films.

(f) RbI-Passivated $Cs_{0.15}FA_{0.85}PbI_3$ Films

In contrast to the results discussed for RbI-passivation on $MAPbI_3$ films, where intermediate phases were observed, RbI initially formed separate domains in $FAPbI_3$ films. Reflections at angles 2θ of 24.3°, 34.6°, 42.7° and 49.7° in the XRD patterns are assigned to cubic RbI (COD entry no. 9009738, space group $Fm\bar{3}m$, lattice constant a = 7.3291 Å, turquois in Figure 4.15B). However, the intensities of these reflections decrease over time. Clear phase segregation was also indicated by floating grains in AFM topography (s. Figure A.12B). Note that the dark circles in the photos in Figure 4.15C as well as Figure 4.16C simply stem from a steel plate glued to the substrate, necessary for analysis via AFM.

Although δ-$FAPbI_3$ is forming (absorption at 379 nm in Figure 4.15A), the XRD pattern suggests the additional formation of an intermediate phase, indicated by the intensification of the reflection at 13.2° (asterisk in Figure 4.15B), corresponding to the absorption at 415 nm in UV/Vis (s. Figure 4.15A). This reflection has been assigned to $RbPbI_3$ by Saliba et al.[28]

46

Consistent with the hypotheses delineated in Section 4.2.1 regarding the possibility of interstitial incorporation of Rb^+ ions into the perovskite lattice, it is therefore conceivable that the system initially consists of three distinct phases: a rubidium-rich α-$FAPbI_3$ phase, $RbPbI_3$ and excess RbI. Again, the system's structural disorder is characterized by a strong increase in Urbach energy from (52.3 ± 0.5) meV in the pure film to (67.7 ± 0.5) meV.

At first, the doped α-$FAPbI_3$ lattice releases strain by forming δ-$RbPbI_3$ with any excess PbI_2 formed during degradation. This is reflected in the growing reflection peak at 13.2° in the XRD pattern (s. Figure 4.15B) as well as in the depletion of initial excess PbI_2, the presence of which is indicated by the reflection at 12.3°. This expulsion is accompanied by a blueshift in PL towards the value of the reference sample, corresponding to a widening of the bandgap. As soon as all Rb^+ ions have been expelled, the common transformation from α-$FAPbI_3$ to δ-$FAPbI_3$ occurs due to an increase in phase transition temperature,[53] as indicated by the sudden emergence of the δ-$FAPbI_3$ (100)-reflection after 10 h of ambient storage, accompanied by the absorption at 379 nm in UV/Vis. Contrary to the described stabilizing mechanism however, any excess RbI may in turn accelerate the degradation due to its hygroscopic binding of atmospheric water. For purposes that go beyond the investigation of the stabilizing mechanism, it is therefore suggested to lower the RbI-loading from the here-used 20 mol% to below 10 mol% in order to erase detrimental effects caused by the hygroscopicity of RbI.[28]

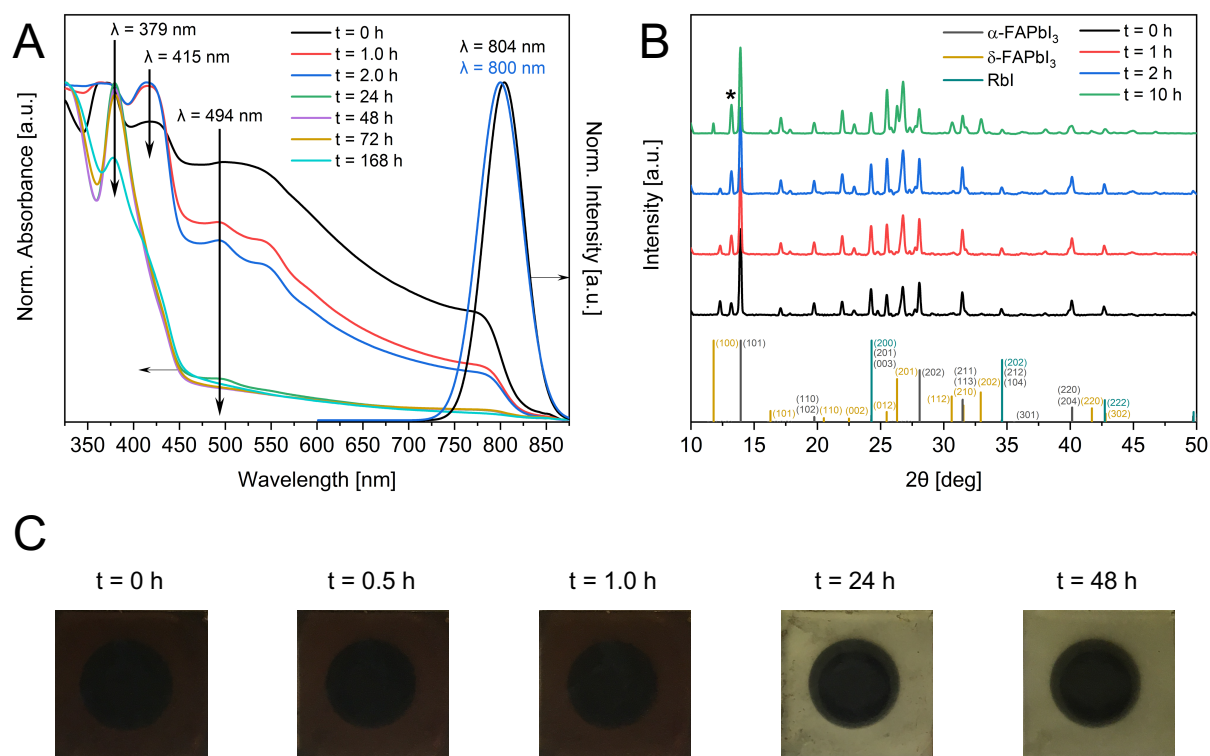**Figure 4.15.** (A) Normalized UV/Vis and PL spectra of a RbI-passivated $Cs_{0.15}FA_{0.85}PbI_3$ thin film recorded over the course of one week, (B) XRD patterns recorded in time-steps of 1.0 h, (C) photographic record of the degrading films.

(g) KI-Passivated Cs$_{0.15}$FA$_{0.85}$PbI$_3$ Films

As for the addition of KI, separate domains with reflections at angles of 21.8°, 25.4° and 44.5° matching cubic KI (ICSD collection code 22158, space group $Fm\bar{3}m$, lattice constant a = 7.0491 Å, purple in Figure 4.16B) were observed as well. This was consistent with results from KPFM measurements discussed below (s. Figure 4.24). However, an intermediate phase was neither detected in the UV/Vis spectra (Figure 4.16A) nor in the XRD patterns. In comparison to the non-passivated FAPbI$_3$ films, KI provides a slight stabilizing effect for at least 2 h under ambient conditions (concluding to Figure 4.16A), when δ-phase in the pure film had already entirely formed (cf. Figure 4.11A). This stabilization effect, however, becomes marginal when comparing the XRD patterns of both of the samples. The redshift of the PL peak from previously 798 nm to 807 nm is the only evidence that ion diffusion into the perovskite lattice, similar to the process described above for the MAPbI$_3$ film, may occur.

Literature explaining the passivation mechanism via alkali metal cations is scarce, but Son et al. as well suggest the possibility of K$^+$ occupying O$_h$ interstitial sites and thus suppressing the migration of I$^-$ anions.[50] Nonetheless, this doping effect is not sufficient in order to lower the phase transition temperature to δ-FAPbI$_3$, although it does enhance the electrical performance under illumination.[50]
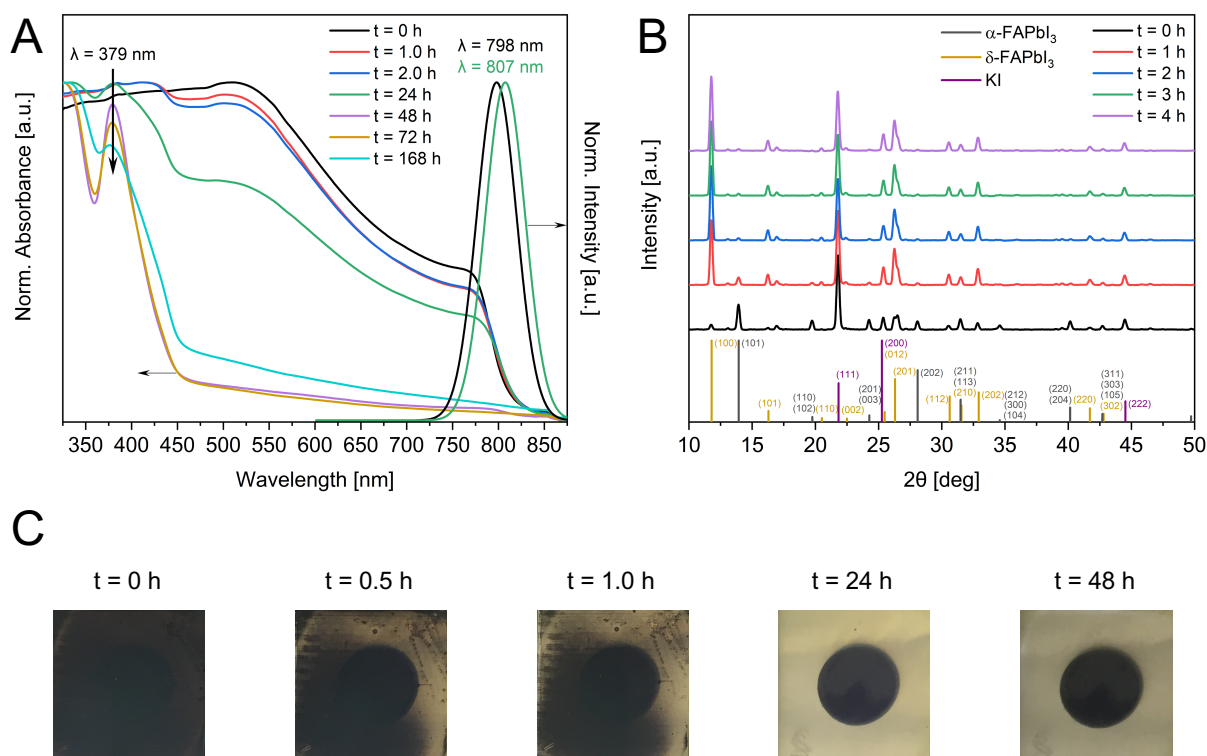
Figure 4.16. (A) Normalized UV/Vis and PL spectra of a KI-passivated $Cs_{0.15}FA_{0.85}PbI_3$ thin film recorded over the course of one week, (B) XRD patterns recorded in time-steps of 1.0 h, (C) photographic record of the degrading films.

(h) Interim Conclusion

In summary, significant stabilization of α-FAPbI$_3$ could be achieved by the addition of either APTES or PEAI to the thin film composition. The stabilizing effect of APTES has been associated with the reduction of crystallite sizes due to the capping property of the amine functionality. The reduction in grain size and undesired introduction of defect states may be circumvented by either reducing the amount of APTES in the precursor solution or by coating a second layer of APTES monomer on top of a conventionally grown film in order to avoid microstrain and rather take advantage of the encapsulating property after polymerization.

4.3 Kelvin Probe Force Microscopy Measurements

On a macroscopic scale, the tested passivation agents proved to have strongly divergent effects on the ambient stability of the perovskite film. In order to find evidence for the observed behavior on a microscopic scale, AFM and FM-KPFM were performed. Mapping of the topography and the CPD of the differently passivated samples thereby reveals information about surface-specific effects, as discussed in Section 2.3.

(a) Non-Passivated MAPbI$_3$ Films

The topography and the CPD maps of a pure MAPbI$_3$ film, which was thermally annealed for 15 min, are shown in Figure 4.17A and Figure 4.17B, respectively. DMSO-annealing proved to be disadvantageous in the thin film synthesis since dewetting and pinhole formation occurred due to increased diffusion. An AFM image of this effect is given in Figure A.12C in the appendix. From the topography of the thermally annealed film, it is apparent that the marked area 1 exhibits steeper regions than the rest of the sample. It is therefore plausible to assume a geometric contribution to the CPD within that area in Figure 4.17B. In the overlay of the two images in Figure 4.17C, it becomes even more evident that one side of the elevation consistently exhibits a higher CPD than the other side.

However, the geometric contribution can only partially explain the non-uniform CPD distribution over the whole scan area. The marked areas 2, 3 and 4, for instance, are at similar altitudes of around 120 nm, but vary significantly in their CPD: Values of (-0.44 ± 0.01) V in area 2, (-0.38 ± 0.02) V in area 3, and (-0.55 ± 0.04) V in area 4 were determined. Since the measurement was taken in a dry environment and no additives that can induce band bending were added, effects of chemi- and physisorption were minimized. Moreover, excluding geometric factors as well, these varying CPD values may be explained either by band bending due to stoichiometric deviations or an inherent facet dependence.

In the XRD patterns in Figure 4.5B, a strong predominance of (110)- and (220)-reflections was found along with virtually no occurrence of PbI_2. Due to the self-doping effect of $MAPbI_3$ caused by excess PbI_2 after evaporation of methylamine from the grain surface, PbI_2-rich grain will be increasingly more n-doped compared to a perfectly stoichiometric $MAPbI_3$ grain, leading to an elevation of the Fermi level.[54] As described above (s. Figure 2.5), higher vacuum energy levels translate into a lower detected CPD. Thus, it can be argued that area 4, which exhibits an especially low CPD, represents a PbI_2-rich grain, while the grains in areas 2 and 3 with a ΔCPD of (0.06 ± 0.02) V might in fact be different facets of a $MAPbI_3$ crystal. When comparing the CPD maps of passivated samples with the one of the non-passivated sample, an inherent facet contrast in the range of 60 mV can, thus, serve as a reference value.
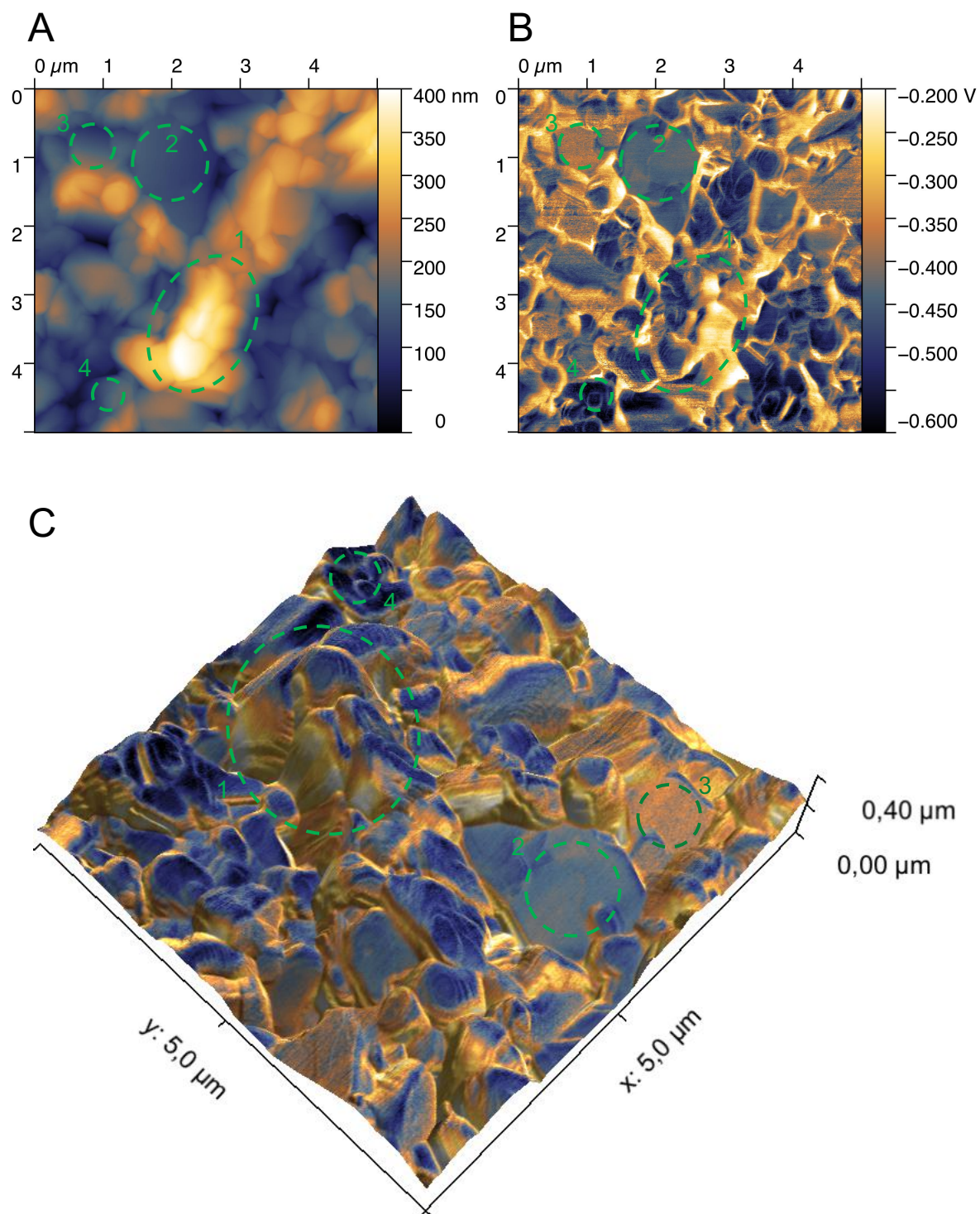
Figure 4.17. (A) Topography of a thermally annealed MAPbI$_3$ sample, (B) CPD map of the same area on the sample, (C) overlay of the two images. Images (A) and (B) by courtesy of Pascal Rohrbeck.

(b) Non-Passivated $Cs_{0.15}FA_{0.85}PbI_3$ Films

For comparison, the topography and CPD maps of a pure, DMSO-annealed $Cs_{0.15}FA_{0.85}PbI_3$ film are presented in Figure 4.18A and Figure 4.18B. As exemplified on the elevated grain in area 1, there is a low CPD on both sides of the elevation. With the help of the overlay in Figure 4.18C, it becomes clear that the correlation between topography and CPD is, therefore, assumed to be small.

Since, in this case, the sample consists of a mixed-cation perovskite, microsegregations into Cs-rich areas and Cs-poor areas are possible. Areas 2 and 3, for instance, exhibit a contrast of (0.08 ± 0.04) V, which is in the same order of magnitude as the facet dependence demonstrated in the non-passivated $MAPbI_3$ film. The facet dependence has previously been attributed to a different distribution of defects on the surface of the respective facets.[39] The higher CPD in area 2 could, therefore, be explained by downward band bending due to donor-type defects such as I^- vacancies while, *vice versa*, the lower CPD in area 3 can be caused by upward band bending due to predominantly FA^+ or Cs^+ vacancies. The effect of an explicit phase segregation, however, is expected to be much more pronounced, which can be observed in area 4. Here, the CPD drops to (-0.9 ± 0.2) V, correlating to a small grain structure in the topography. Due to the presence of excess PbI_2 confirmed via XRD (s. Figure 4.11B), the signal may be assigned to that phase.

Evidently, the CPD map shows a lower signal-to-noise ratio (SNR) than the respective CPD map of the $MAPbI_3$ film (cf. Figure 4.17B). A lower SNR implies an attenuated electric field between tip and sample surface. Such an attenuation may be caused by the presence of an insulating layer within the space between tip and surface. However, the nature of the eventual insulating layer could, unfortunately, not be rationalized.
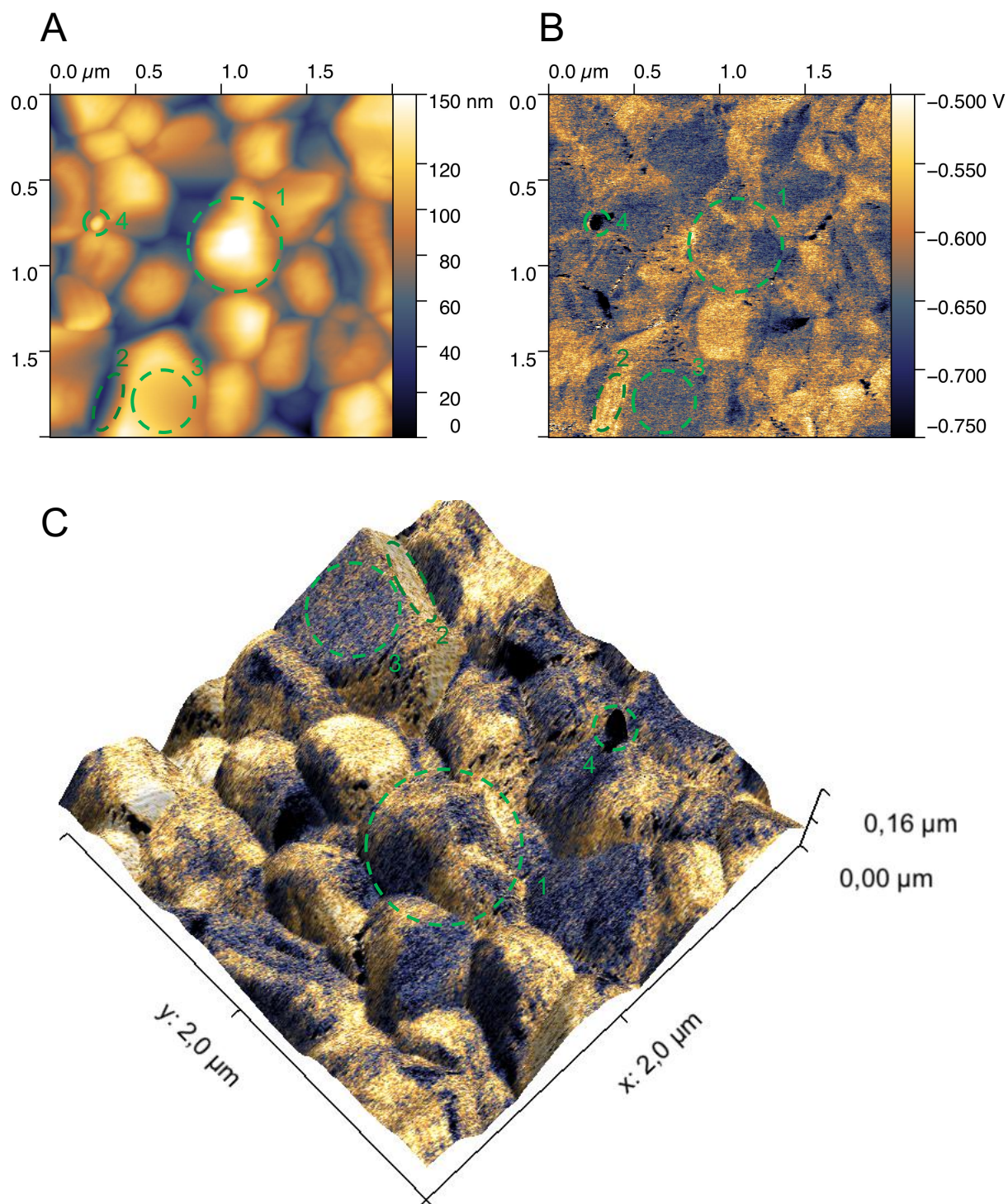
Figure 4.18. (A) Topography of a DMSO-annealed $Cs_{0.15}FA_{0.85}PbI_3$ sample, (B) CPD map of the same area on the sample, (C) overlay of the two images.

(c) TEOS-Encapsulation

In Figure 4.19A and Figure 4.19B, topography and CPD of a DMSO-annealed MAPbI$_3$ film with TEOS additive are shown. Evidently, DMSO-annealing leads to an increased grain size of up to 800 nm. The very slow polymerization of TEOS observed via ^{29}Si-NMR (s. Section 4.1.1) evidently allows the perovskite crystal to grow without inhibition due to polymer rigidification. Again, the XRD pattern in Figure 4.6B shows a high count of (110)- and (220)-reflections. Strikingly, the marked areas 1 and 2 exhibit the same facet dependent deviation in CPD of (0.06 ± 0.4) V that has been extracted for the pure MAPbI$_3$ film.

With regard to Figure 4.19B, there is no visible CPD contrast at the GBs. If the assumption of silica-encapsulated grains held true, darker areas along the GBs would be expected due to silica being an electrical insulator, not yielding a CPD signal. However, if the thickness of the insulating layer is below the lateral resolution of the device, it may not be discretely visible in the image, but may instead reduce the SNR as described above. If grain encapsulation worked as assumed, also the top of the grain would be covered with a thin layer of silica. Therefore, the reduced SNR in the CPD map in Figure 4.19B can serve as an indication for successful grain encapsulation described by Liu et al.[21] Nevertheless, the stability studies in Section 4.2.1 did not show enhancement of the film's ambient stability, even though an encapsulating layer may be present.
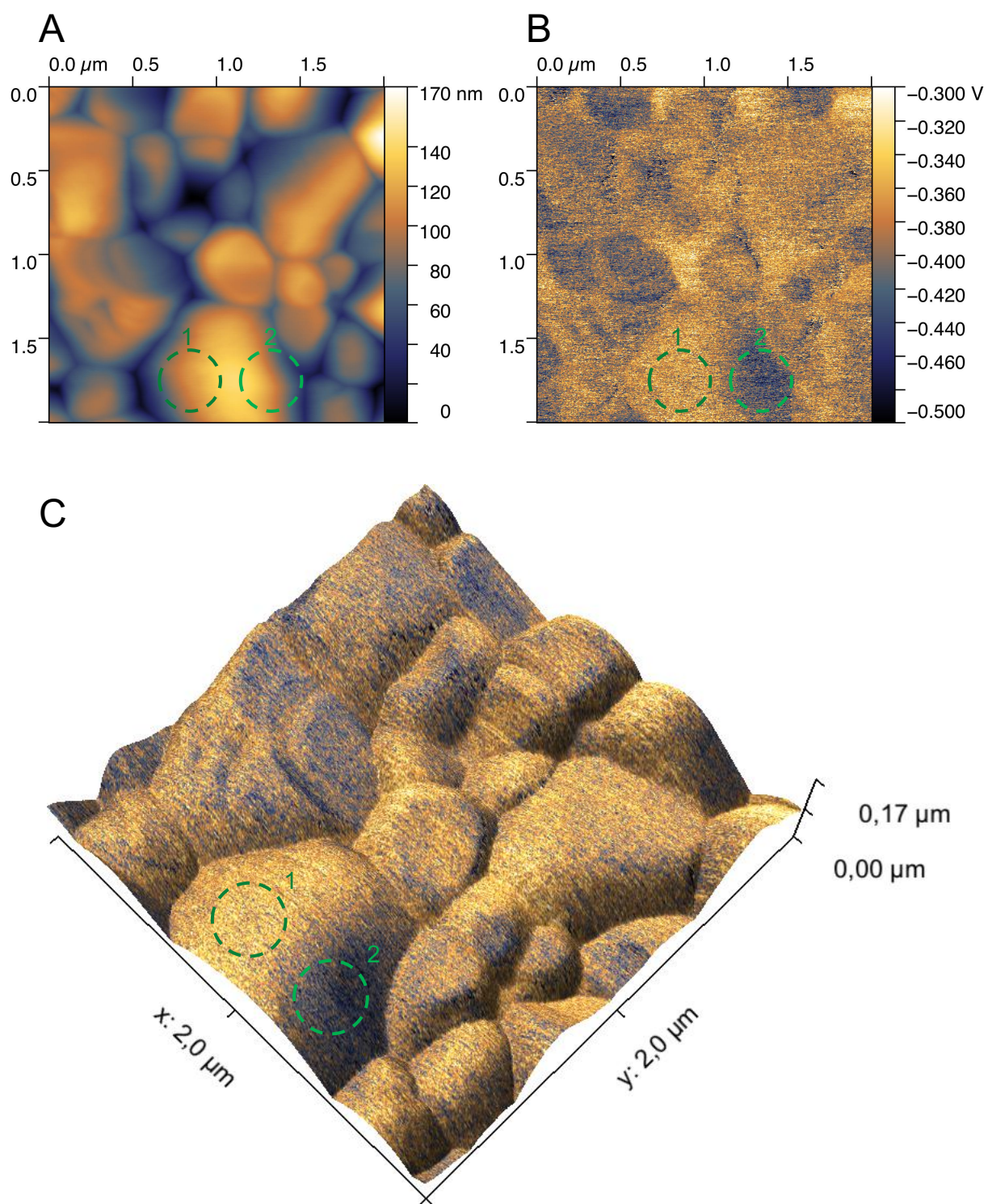
Figure 4.19. (A) Topography of a DMSO-annealed MAPbI$_3$ sample with TEOS additive, (B) CPD map of the same area on the sample, (C) overlay of the two images.

(d) APTES-Encapsulation

The topography of an APTES-encapsulated $Cs_{0.15}FA_{0.85}PbI_3$ sample most noticeably shows truncated-pyramid-like structures (s. Figure 4.20A). These structures are also reflected in the CPD map in Figure 4.20B. This is a strong indication for the amine group of APTES acting as a capping ligand, enabling growth of the (100)-facet, as observed via XRD (s. Figure 4.13B). The suggestion of small, yet highly oriented grains from Section 4.2.2 can, thus, be confirmed. The flat tops of the pyramids consistently exhibit high CPD values of around $(+0.9 \pm 0.2)$ V. The captured value is not dependent on the height of the facet, as demonstrated in areas 1 to 3, which are all positioned at different heights. Furthermore, areas with a comparatively low CPD of down to $(+0.3 \pm 0.1)$ V also do not show altitude dependence (areas 4 and 5).

The high contrast of the CPD map can be an indication of a varying coverage of the perovskite with APTES-polymer. Due to localized initiation of the self-condensation polymerization, nucleation centers occur from which the reaction then propagates. We have seen via ^{29}Si-NMR in Section 4.1.2 that the hydrolysis of APTES occurs drastically faster than the hydrolysis of TEOS under equal conditions, amplifying the non-uniform growth once nucleation centers have formed. Contrary to film growth with TEOS additive, the polymerization reaction is in interference with the perovskite crystallization, making the simultaneous perovskite/APTES film growth a very complex process.

For instance, the occurrence of low CPD values such as in areas 4 and 5 suggests the presence of highly cross-linked APTES-microparticles. On other areas (8 and 9), however, the comparatively higher CPD indicates perovskite crystals being buried under an APTES-layer. Accordingly, the bright areas 1 to 3 correspond to a very thin APTES-layer.

Clearly, the reaction conditions for the *in-situ* synthesis of the APTES encapsulation layer need to be optimized, as also indicated by the critically high Urbach energies in Section 4.2.2. For example, monomer concentration or annealing temperature can be decreased in order to decelerate the polymerization of APTES. Nevertheless, the observed stabilizing effect on δ-$FAPbI_3$ under ambient conditions is very promising.
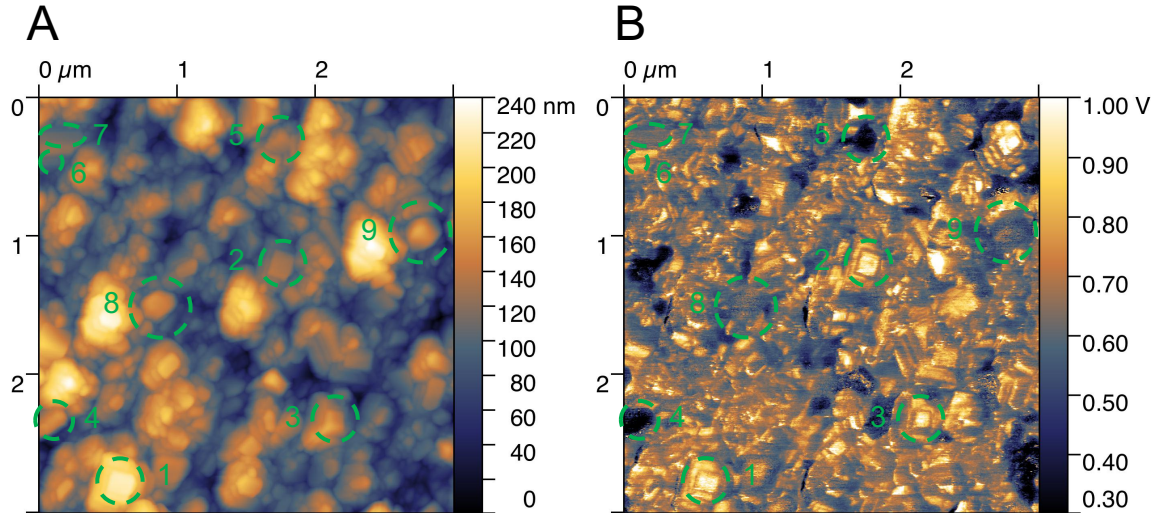
Figure 4.20.   (A) Topography of a DMSO-annealed $Cs_{0.15}FA_{0.85}PbI_3$ sample with APTES additive, (B) CPD map of the same area on the sample.

(e) PEAI-Passivation

The 2D-perovskite passivation layer due to PEAI-addition did not enhance the long-term stability of $MAPbI_3$ films, while it had a significantly beneficial effect on mixed-cation $Cs_{0.15}FA_{0.85}PbI_3$ films. It is therefore interesting to look via KPFM for microscopic evidence for the observed behavior.

The XRD pattern of PEAI-passivated $MAPbI_3$ film (s. Figure 4.8B) showed a higher, while the PEAI-passivated $Cs_{0.15}FA_{0.85}PbI_3$ film (s. Figure 4.14B) showed an equal diversity of reflections compared to their non-passivated correspondents. The XRD results are reflected in the topography of the two samples: Although both samples were DMSO-annealed, $MAPbI_3$ grains exhibit a significantly smaller grain size as well as a higher orientational disorder (s. Figure 4.21A) compared to the $Cs_{0.15}FA_{0.85}PbI_3$ grains, which grew up to 1.2 μm (s. Figure 4.22A) and show a more uniform distribution of CPD (Figure 4.22B). Interestingly, the areas 2, 3, 4 and 5 in the PEAI-passivated $MAPbI_3$ film all show an equally high CPD of $(+0.26 \pm 0.03)$ V, which is the translation of a decreased Fermi level. In areas 6 and 7, an intra-grain contrast as high as (0.22 ± 0.06) V was determined, which is well above the determined inherent facet contrast of $MAPbI_3$ of around 60 mV. It is therefore suggested that a 2D layer may only form on top of distinct facets of the 3D-grains, while others which do not show such high CPD values may lay bare.

Furthermore, the CPD signal of the passivated MAPbI$_3$ film shows distinctively high CPD values on the edges of particular grains. As evident from the profile along line 1 (s. Figure 4.21), this sharp increase to a maximum of $+440$ mV does not correlate to the topography and can, therefore, not purely be explained by a tip-geometric contribution. Due to their structure, 2D-perovskites are expected to exhibit strongly anisotropic electrical behavior.[55] If one assumes that the 2D-perovskite layer is located on particular facets of the grain, it is conceivable that, on the grain edges, either the 3D-perovskite grain interior itself or the lateral edge of the 2D-layer is exposed, leading to the sharp increase in CPD.
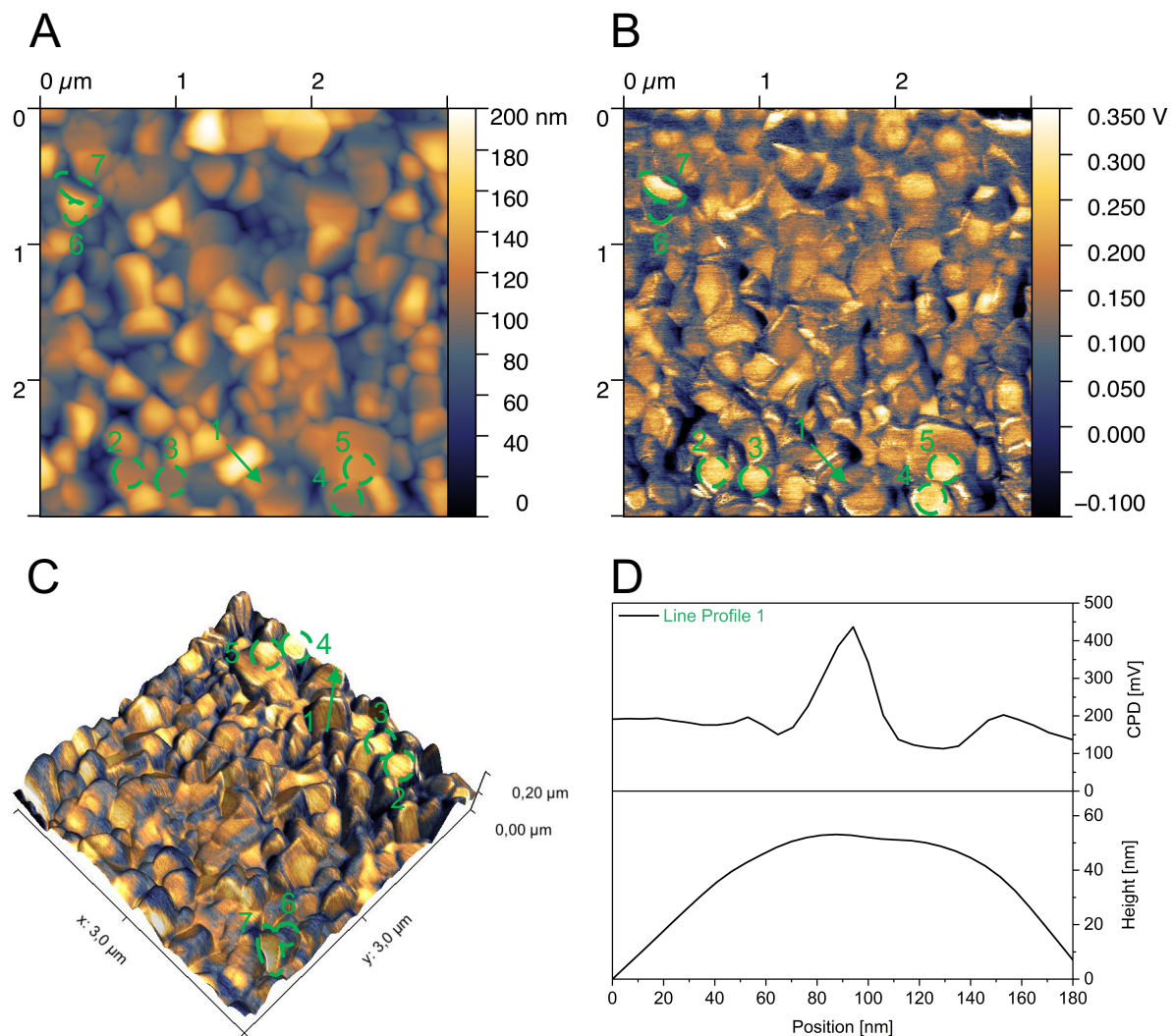

Figure 4.21. (A) Topography of a DMSO-annealed MAPbI$_3$ sample with added PEAI, (B) CPD map of the same area on the sample, (C) overlay of the two images. (D) CPD and height profiles along line 1, showing no correlation to each other. Both profiles were averaged over a line width of 25 pixels.

In contrast to the PEAI-passivated $MAPbI_3$ film, the corresponding $Cs_{0.15}FA_{0.85}PbI_3$ film exhibits large grains with extraordinarily pronounced terrace structures. Both of these observations imply altered crystal growth dynamics in the PEAI-passivated $Cs_{0.15}FA_{0.85}PbI_3$ film. Note that the dark spots in the CPD map in areas 4 and 5 are imaging artifacts arising due to phase jumps of the cantilever on the steep grain edges.

The UV/Vis spectrum of the PEAI-passivated $Cs_{0.15}FA_{0.85}PbI_3$ film (s. Figure 4.14A) showed no indication of the formation of low-dimensional perovskite in the bulk. Excitonic peaks would otherwise be expected in the range of 550 nm to 600 nm.[56] In contrast to the respective $MAPbI_3$ film, the passivated $Cs_{0.15}FA_{0.85}PbI_3$ film exhibits large grains of up to 1.2 µm as well as pronounced terrace structures on the surface, oftentimes perpendicular to the substrate surface, as it becomes clear from areas 6 to 9 of the 3D-profile of the surface in Figure 4.22D. Furthermore, a ΔCPD of around (0.18 ± 0.7) V was determined from areas 2 and 3, representing the lateral and the vertical edge of these terrace structures, respectively, which is larger than the ΔCPD of (0.08 ± 0.04) mV observed in a pure $Cs_{0.15}FA_{0.85}PbI_3$ film due to facet dependence.

Note that care has to be taken with the determined higher ΔCPD value. On the one hand, the darker areas on the terrace edges, as exemplified in area 6 in Figure 4.22C, may be imaging artifacts since the frequent riffles on the surface can cause perturbations that lead to oscillation phase jumps of the cantilever. On the other hand, no such anomalous phase jumps were detected in the considered areas 2 and 3, so that the determined ΔCPD value of (0.18 ± 0.7) V might, in fact, suggest a higher contrast between lateral and vertical terrace edges. This, in turn, can indicate the presence of layered perovskites on the surface along the terrace structures due to the fact that 2D-perovskites are expected to show electrical anisotropy.[55] The terrace structures may even only arise due to the presence of layered perovskite since they were not detected in the non-passivated $Cs_{0.15}FA_{0.85}PbI_3$ film.

Thus, the reason for the discrepancy in the stabilizing effect of PEAI on MAPbI$_3$ and Cs$_{0.15}$FA$_{0.85}$PbI$_3$ films may be found in the morphology of the two films. The MAPbI$_3$ film exhibits significantly smaller grains and preferred formation of 2D-perovskite on distinct facets, while the Cs$_{0.15}$FA$_{0.85}$PbI$_3$ film shows a high tendency to form larger grains. Indications have been found that the 2D-perovskite is covering the pronounced terrace structures in Cs$_{0.15}$FA$_{0.85}$PbI$_3$ films, with the PEA$^+$-layer protecting the interior more effectively from moisture.
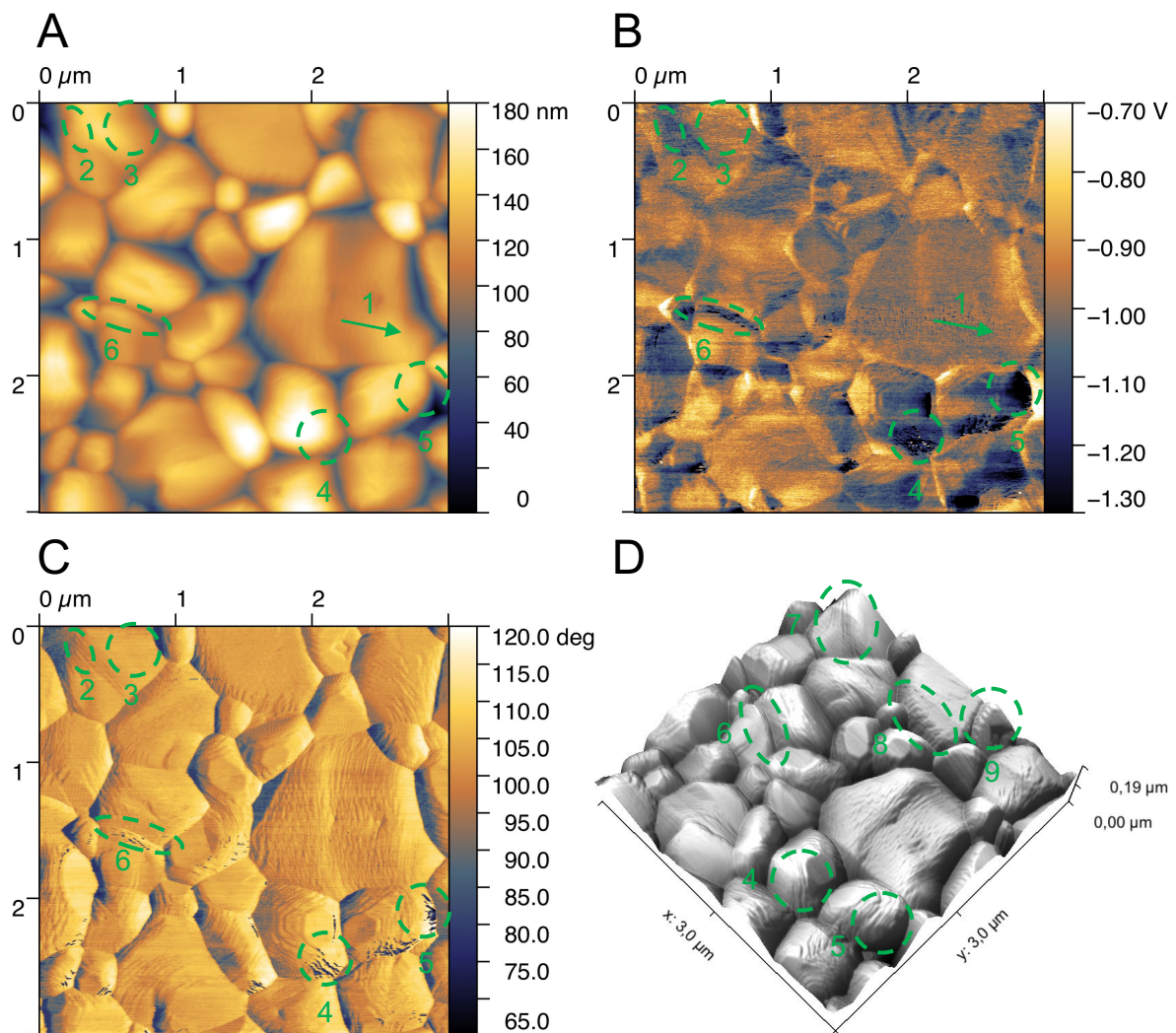

Figure 4.22 (A) Topography of a DMSO-annealed Cs$_{0.15}$FA$_{0.85}$PbI$_3$ sample with added PEAI, (B) CPD map and (C) phase image of the same area on the sample, (D) 3D-profile of the topography.

(f) RbI-Passivation

In Section 4.2.1, the occurrence of a mixed phase was observed in the XRD diffraction pattern. Furthermore, an initial incorporation of Rb^+ ions into the lattice was hypothesized. In Figure 4.23A and Figure 4.23B, the topography and CPD maps of a DMSO-annealed MAPbI$_3$ sample with a 20 mol% loading of RbI are presented. The topography echoes the strong predominance of (110)- and (220)-reflections determined via XRD.

In fact, the observation of ferroelastic twin domains (orthogonal to line 1), which have also been observed in pure MAPbI$_3$ films before,[57] can serve as an indicator for Rb-incorporation: The mismatch of Rb^+ in the perovskite lattice causes microstrain. At a certain concentration of mismatched ions, the lattice releases the strain by crystal twinning.[57] Due to alternating crystal facets being exposed to the surface, a contrast is visible in the topography as well as in the CPD signal, best visible in the overlay in Figure 4.23C. From the profile along line 1 in Figure 4.23D, the width and height of the ferroelastic stripes was determined to be around 100 nm and 0.4 nm, respectively, with a ΔCPD of approximately 30 mV. Note that the twin domains were also observed in pure MAPbI$_3$ films and are, therefore, by themselves no proof of Rb^+ incorporation. However, it is known that structural defects like dislocations, interstitials and vacancies induce microstrain,[46] facilitating the formation of ferroelastic twin domains particularly in this sample.

Moreover, the formation of a separate phase with a CPD value of (–0.2 ± 0.3) V was observed in areas 3 to 6, which substantiates the explanations made with respect to the XRD-pattern. According to the KPFM image, the separate phase exhibits a significantly lower Fermi level than the surrounding perovskite with a CPD of (–1.0 ± 0.1) V. The exact chemical composition of the phase can, however, not be determined from the CPD map.

The needle-shaped crystals visible in the top left corner (area 2) of Figure 4.23 show a similar CPD as the rest of the sample surface and can therefore be assigned to MAPbI$_3$. It is known that MAPbI$_3$ shows needle-like growth in its monohydrate form as a sign of degradation due to humidity exposure.[58] The observed unassigned phase in XRD with a reflection at an angle 2θ of 11.5° can, however, not be explained by the formation of MAPbI$_3$ monohydrate with certainty since the reflection does not match with any observed reflection in the literature.[16]
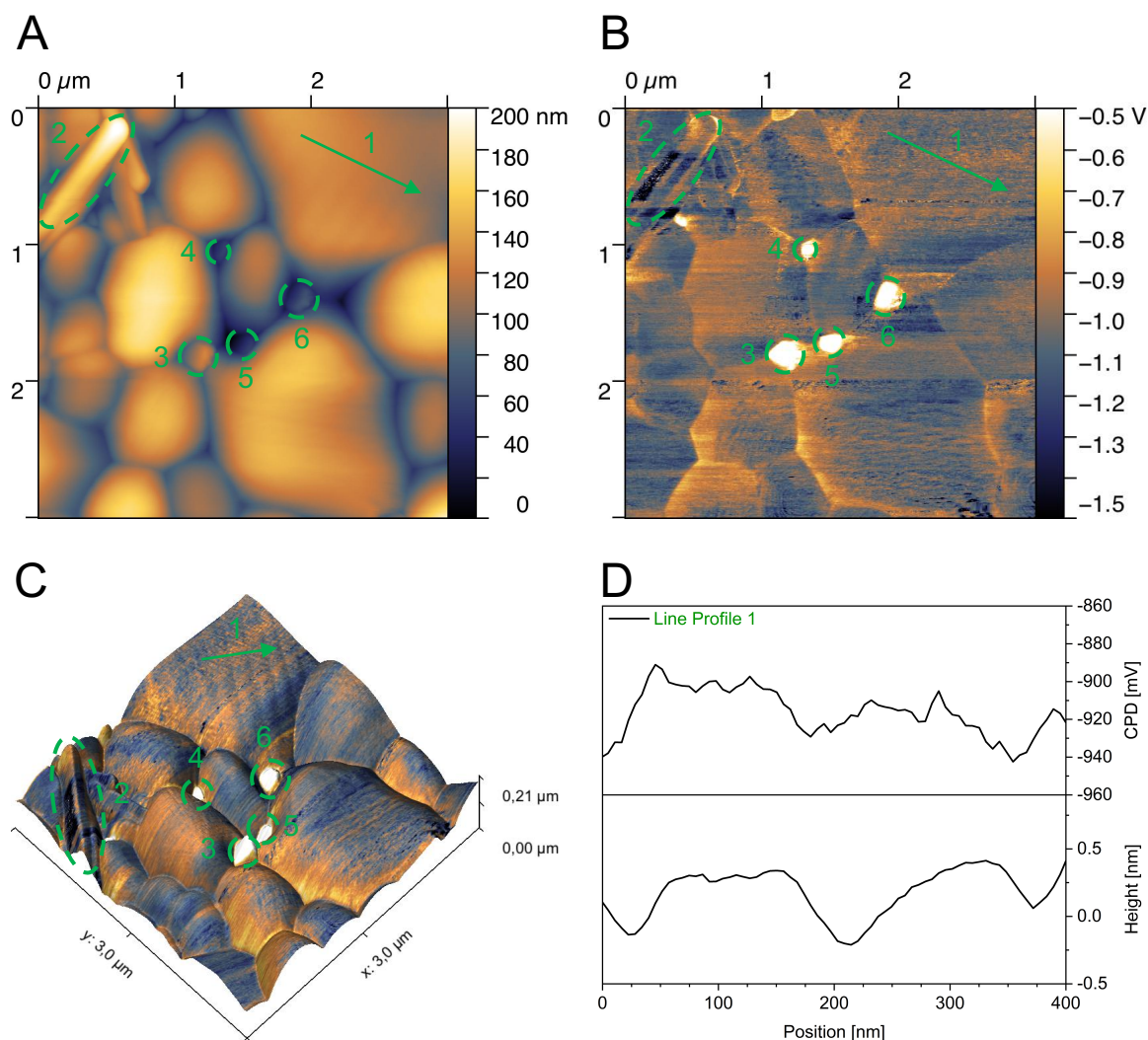
Figure 4.23. (A) Topography of a DMSO-annealed MAPbI$_3$ sample with added RbI, (B) CPD map of the same area on the sample, (C) overlay of the two images. (D) CPD profile and baseline-corrected height profile along line 1, both profiles were averaged over a line width of 100 pixels.

(g) KI-Passivation

In a KI-passivated Cs$_{0.15}$FA$_{0.85}$PbI$_3$ sample, no significant stabilization effect was observed in Section 4.2.2. Instead, the XRD pattern showed phase segregation into separate KI-domains. Areas 1 and 2 in the CPD map of the DMSO-annealed film in Figure 4.24B show an intra-grain contrast of (0.08 ± 0.04) V. Since this value does not significantly deviate from the facet contrast inherent to the non-passivated sample, the only indication for phase segregation can be found in the altered morphology compared to the rest of the film.

In areas 3 and 4, which represent two facets on the same grain, a ΔCPD of (0.07 ± 0.01) V was determined. This value is in agreement with the inherent facet-dependent contrast that was determined for the pure film. Thus, no aberrant band bending or doping effect can be detected, indicating that there is neither K^+ incorporation into the lattice nor a formation of a passivation layer around the grains. This observation corresponds well to the negligible stabilizing effect of KI addition found above.

A reason for the enhanced solar cell performance observed by other groups cannot be given on the basis of the obtained results: Abdi-Jalebi et al. claim that KI is immobilized at the GBs and surfaces, filling perovskite halide vacancies.[27] In our experiments, this presence could not be confirmed. However, in order to test their hypothesis, the DMSO-annealing step should, in our case, be renounced since it facilitates the phase segregation of KI due to increased diffusion. Besides KPFM, time-resolved PL can serve as an indication for the open question if defect passivation at the GBs actually takes place.
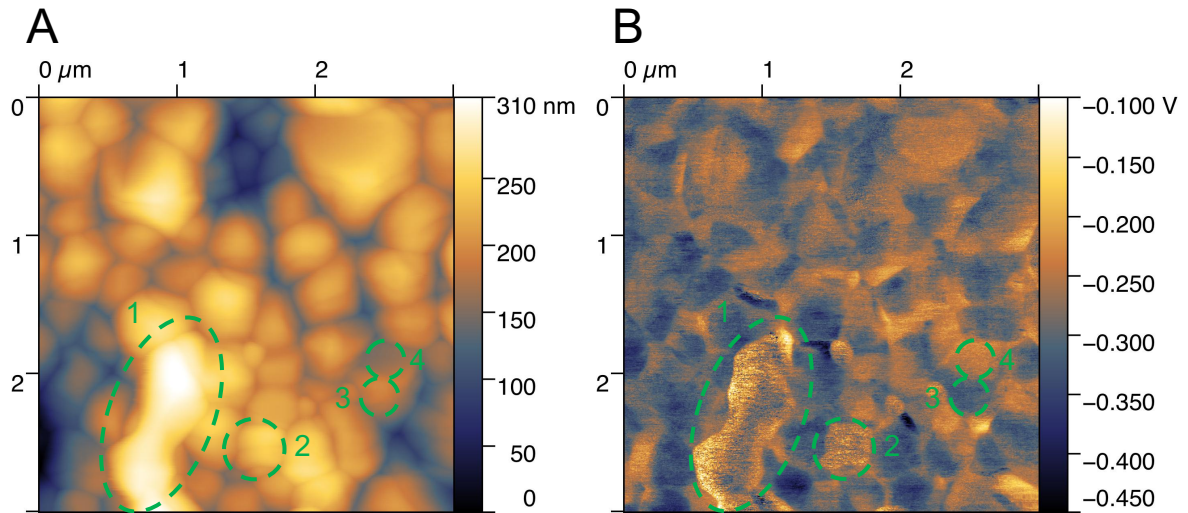

Figure 4.24. (A) Topography of a DMSO-annealed $Cs_{0.15}FA_{0.85}PbI_3$ sample with added KI, (B) CPD map of the same area on the sample.

(h) Interim Conclusion

In summary, an inherent facet contrast of (0.06 ± 0.2) V and (0.08 ± 0.04) V could be extracted from the total CPD signal for $MAPbI_3$ and $Cs_{0.15}FA_{0.85}PbI_3$ films, respectively. On the basis of a reduced SNR and in accordance with the claims made in the literature, it is suggested that TEOS does, in fact, form an encapsulation layer around the perovskite grains.[21] In our experiments, however, the presence of the encapsulation layer did not enhance the film's ambient stability. On the contrary, topography imaging on an APTES-encapsulated $Cs_{0.15}FA_{0.85}PbI_3$ film showed the strong reduction in grain size which may be the reason for a lowered phase transition temperature and increased stability. However, the film's homogeneity needs to be optimized for future applications.

The significantly enhanced intra-grain contrast in a PEAI-passivated $MAPbI_3$ film along with the occurrence of sharp lines of high CPD on the edges of the small grains indicate preferred formation of 2D-perovskite layer on distinct facets, while the corresponding $Cs_{0.15}FA_{0.85}PbI_3$ film formed significantly larger grains with pronounced terrace structures. The occurrence of terrace structures was associated with the presence of 2D-layered perovskite on the surface.

Finally, it could be shown that RbI and KI tend to form separate phases under the given synthesis conditions. The observation of ferroelastic twin domains is no proof but can serve as an indication of partial incorporation into the perovskite lattice at defect sites. On the contrary, an assumed localization of potassium at the grain exterior could not be detected via FM-KPFM.[27]

5 Conclusion and Outlook

Within this work, smooth thin films of $MAPbI_3$ and $Cs_{0.15}FA_{0.85}PbI_3$ could successfully be synthesized in pure form and with addition of encapsulating agents TEOS and APTES and passivating agents PEAI, RbI and KI. Time-resolved characterization of the synthesized films via UV/Vis and PL spectroscopy as well as XRD was performed.

There are no reports in the literature on the use of APTES as an encapsulation agent on perovskite thin films. Both in $MAPbI_3$ and in $Cs_{0.15}FA_{0.85}PbI_3$ films, APTES was among the additives with the highest stabilizing effect under ambient conditions. No considerable changes in absorption were detected via UV/Vis after 3 d of ambient storage for a $Cs_{0.15}FA_{0.85}PbI_3$ film, as compared to less than 1 h for a non-passivated film. The stabilizing effect was attributed to a decreased phase transition temperature due to reduced grain size, detected via XRD and visualized via AFM, suggesting the amino functionality acting as a capping ligand for the perovskite grain during growth. Nevertheless, these first trials still yielded comparatively high Urbach energies, implying that the synthesis parameters need to be optimized in the future.

With respect to the impact of the different additives on grain morphology and CPD, AFM and FM-KPFM proved to be useful tools. It could be shown that formation of Ruddlesden-Popper phase due to addition of PEAI is causing different growth dynamics in $Cs_{0.15}FA_{0.85}PbI_3$ compared to $MAPbI_3$ thin films, in the former case leading to pronounced terrace structures orthogonal to the substrate plane and drastically increased stability compared to the non-passivated sample.

Time-resolved ^{1}H-NMR and ^{29}Si-NMR experiments on the native precursor solution proved that APTES hydrolysis occurs on a faster time scale than TEOS hydrolysis, which was reflected primarily in the morphology of the thin films. Decreasing APTES monomer concentrations as well as annealing temperatures may decelerate the polymerization and enable the grains to grow larger, while still maintaining its phase-stabilizing property. On the contrary, TEOS addition did not prove to be useful for thin film encapsulation since the encapsulation layer indicated by FM-KPFM could not enhance film stability.

Finally, it has become clear that upon addition of RbI and KI phase segregation within the film tends to occur. Nevertheless, indication of partial lattice incorporation of Rb$^+$ has been found via time-resolved XRD and FM-KPFM. For the future, it is suggested to decrease the loading of alkali metal iodide from 20 mol% to below 10 mol% and to renounce any solvent annealing in order to prevent the observed phase segregations.

Prior to this project, the mechanistic details of the different passivation strategies and their impact on thin film morphology and stability were not clear. By comprehensive comparison, this study was able to extract mechanistic differences and give explanations for macroscopically observed degradation behavior.

Unfortunately, Urbach energies for the non-passivated films were higher than in comparable films reported in the literature.[44] In order to lower the initial Urbach energy, the spin-coating parameters need to be optimized. Contrary to the expectations, none of the passivating agents was capable of decreasing the Urbach energy. After optimization of the optimal synthesis parameters and additive amounts with respect to a reduced Urbach energy, time-resolved PL measurements can be performed on the thin films. Increased time constants of the electronic decay would indicate a successful trap state passivation.

Furthermore, the presence of trap states in solar cell devices can be quantified on the basis of I-V-curves. High V_{OC}, I_{SC} and FF are indicative of low trap state density. Towards the end of the project, solar cell devices were built, and I-V-curves were taken. The obtained curves presented in Figure 5.1, however, show room for improvement. The maximum V_{OC} of 790 mV was obtained by an APTES encapsulated MAPbI$_3$ film. Detailed values are given in Table 5.1. The value of 790 mV is still low compared to an achievable V_{OC} around 1.3 V, indicating low quasi-Fermi level splitting due to fast recombination.[59] The shape of the MAPbI$_3$/APTES curve furthermore indicates presence of shunt pathways such as pinholes, as well as series resistances due to suboptimal interface connectivity. Nevertheless, the results are promising to yield well-performing solar cells once the thin film synthesis conditions are optimized.

Table 5.1. Measured values for solar cells fabricated within the scope of this work.

Solar Cell	J_{SC}	V_{OC}	J_{mpp}	V_{mpp}	P_{mpp}	FF
	[mA·cm^{-2}]	[mV]	[mA·cm^{-1}]	[mV]	[μW]	[%]
MAPbI$_3$	26.6	773	18.7	462	346	41.1
MAPbI$_3$/APTES	33.0	790	21.5	517	445	42.7
MAPbI$_3$/PEAI	24.8	461	18.5	316	234	51.3
MAPbI$_3$/KI	24.5	773	17.8	551	393	51.8
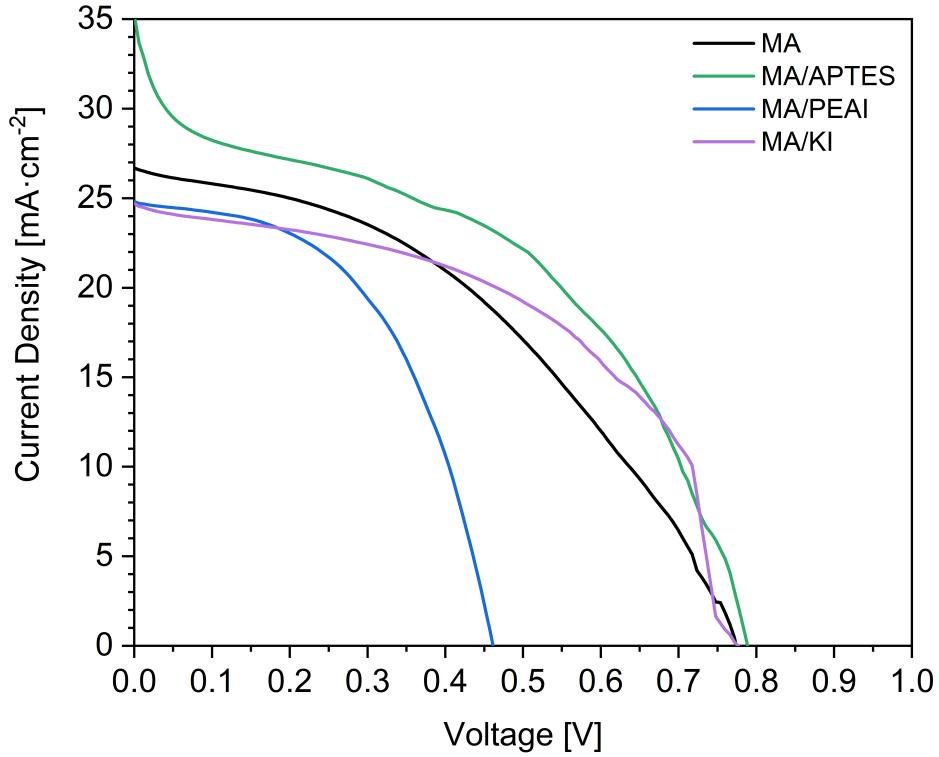
Figure 5.1. Forward *J-V*-scan of selected passivated films under AM1.5G illumination.

6 Experimental Part

6.1 Chemicals

Table 6.1. List of used chemicals.

2,2',7,7'-Tetrakis[*N*,*N*-di(4-methoxyphenyl) amino]-9,9'-spirobifluorene	$C_{81}H_{68}N_4O_8$	Sigma Aldrich	99%
(3-Aminopropyl)triethoxysilane	$C_9H_{23}NO_3Si$	Acros	99%
4-*tert*-Butylpyridine	$C_5H_4NC(CH_3)_3$	Sigma Aldrich	96%
Acetone	$(CH_3)_2CO$	FisherSci	98.8%
Acetonitrile	CH_3CN	Acros	99.9%
Cesium iodide	CsI	Sigma Aldrich	99.9%
Chlorobenzene	C_6H_5Cl	Acros	99.8%
Diethyl ether	$(C_2H_5)_2O$	Aldrich	99.8%
Dimethyl sulfoxide	C_2H_6SO	Sigma Aldrich	99.9%
Formamidinium Iodide	$CHN_2H_3 \cdot HI$	Greatcell	99.9%
Hydroiodic acid (57 wt% in H_2O)	HI	Sigma Aldrich	99.9%
Lead(II) acetate	$Pb(C_3H_2O_2)_2$	TCI	98%
Lead(II) iodide	PbI_2	TCI	98%
Lithium bis(trifluoromethanesulfonyl)imide	$LiN(SO_2CF_3)_2$	Sigma Aldrich	99%
Methylammonium chloride	$CH_3NH_2 \cdot HCl$	Acros	99%
Methylammonium iodide	$CH_3NH_2 \cdot HI$	Dyesol	99.9%
N,*N*-Dimethylformamide	$HCON(CH_3)_2$	Sigma Aldrich	99.8%
Phenylethylamine	$C_8H_9NH_2$	TCI	98%
Potassium iodide	KI	Alfa Aesar	99.9%
Propan-2-ol	C_3H_7OH	FisherSci	98.8%
Rubidium iodide	RbI	Sigma Aldrich	99.9%
Tetraethyl orthosilicate	$Si(C_2H_5O)_4$	Sigma Aldrich	98%
Titanium(IV) chloride	$TiCl_4$	Sigma Aldrich	99.9%
Toluene	C_7H_8	Acros	99.9%

6.2 Measurement Methods

AFM measurements were performed on an MFP3D microscope by AsylumResearch placed in an argon-filled glovebox (GS Mega Line, $O_2 < 0.6$ ppm, $H_2O < 0.2$ ppm). Conductive Pt-Ir-coated silicon cantilevers (Bruker SCM-PIT-V2, 225 µm × 35 µm) with a first resonance frequency of around 70 kHz, a spring constant of 3 N·m^{-1} and a nominal tip radius of 25 nm were used. In FM-KPFM measurements, an HF2LI-MOD lock-in amplifier by Zurich Instruments was used for signal processing. Samples were prepared on conductive indium tin oxide (ITO) coated glass substrates (pgo, 25 mm × 25 mm × 1 mm, $R_S = 20$ Ω/sq) using, unless stated otherwise, 15 min of DMSO-annealing in order to increase grain size for facilitated imaging. Obtained images were viewed and assessed using the software Gwyddion. CPD values were obtained by measuring the respective area in the CPD map via masking. Automatically generated median values were taken as the observable with the root mean squares being the uncertainty.

^{1}H-NMR and ^{13}C-NMR spectra for structure elucidation as well as water content determination were recorded on an AVIII 300 spectrometer by Bruker (300 MHz, 75 MHz). The chemical shifts were referenced to the solvent residual signal (^{1}H-NMR: $\delta_{DMSO} = 2.50$ ppm; ^{13}C-NMR: $\delta_{DMSO} = 39.52$ ppm). Signal assignment is in coherence with the one-dimensional spectra as well as the two-dimensional spectra (heteronuclear single quantum correlation, HSQC). ^{1}H-NMR and ^{29}Si-NMR spectra for time-resolved reaction kinetics were recorded on an AVIII 500 spectrometer by Bruker (500 MHz, 100 MHz) in the native precursor solution matrix without deuterated solvents. The chemical shifts and the peak integrals were referenced with respect to the defined amount of DSS added as an internal standard (^{1}H-NMR: $\delta_{DSS} = -0.05$ ppm; ^{29}Si-NMR: $\delta_{DSS} = 1.20$ ppm).

Photoluminescence (PL) spectra were recorded on a J&M Tidas FL3005SL fluorescence spectrometer with a diode array detector. Obtained spectra were fitted with a Gaussian function and normalized using the software Origin.

Ultaviolet-visible (UV/Vis) spectroscopy was performed on a Perkin Elmer Lambda900 UV/VIS/NIR spectrometer scanning from 900 nm to 300 nm. Measurements were taken on native perovskite films on glass substrate, using an integrating sphere in order to eliminate inaccuracies due to strongly light-scattering samples.

XRD patterns of the native thin films were acquired on a Rigaku SmartLab X-Ray diffractometer in reflection mode equipped with a D/teX Ultra 250 silicon strip detector and Cu-Kα_1 radiation (Ge monochromator, $\lambda = 1.5406$ Å). Samples were prepared on glass substrate. The obtained patterns were assessed using the software Match! 3.

SEM was performed on a Hitachi SU8000 operated at an acceleration voltage of 10 kV. Secondary electrons were detected on the upper detector.

6.3 Thin Film Preparation

The glass substrates (Thermo Scientific Frosted Microscope Slides, 76 mm × 26 mm × 1 mm) were cut into three approximately quadratic pieces and cleaned sequentially in a solution of 2 vol% Hellmanex in deionized water, in pure deionized water, in *iso*-propanol and in acetone in an ultrasonic bath for 15 min each. Subsequently, they were dried under dry nitrogen flow. The substrates were then subjected to UV-ozone treatment (FHR UVOH 150 LAB) for 30 min at an oxygen-flow of 1.0 L·min^{-1} before they were transferred into a nitrogen-filled flowbox (GS Glovebox P10T2 1000x, $H_2O \approx 20$ ppm) for spin-coating.

For MAPbI$_3$ thin film synthesis, lead(II) iodide (PbI$_2$) and methylammonium iodide (MAI) and respective passivating agents were weighed out on a high-precision balance (Mettler Toledo LabStyle 204, d = 0.1 mg) in a nitrogen-filled glovebox (MecaPlex Mecabox 82-1 LF). The powders were dissolved in a mixture of DMF and DMSO (5:1 v/v) to a 1 M solution with respect to the amount of lead(II) iodide. Dissolution of the powders as well as one-step spin-coating of the substrates was performed in the nitrogen-filled flowbox equipped with a spin-coater (Laurell Technologies WS-400BZ-6NPP/LITE). For the deposition, 100 μL of the precursor solution was evenly distributed over the freshly cleaned substrate surface. The plate was then spun at an acceleration of 4400 rpm·s^{-1} to 4500 rpm for 20 s overall. 10 s before the

end, 250 μL of toluene antisolvent was dropped onto the surface from a distance of approximately 5 mm. The thin film was subsequently subjected to either thermal or DMSO-solvent annealing at 120 °C for 15 min. DMSO-solvent annealing was performed by placing 30 μL of DMSO in a small reservoir under a Petri dish. After the atmosphere under the dish had saturated with solvent vapor, the film was rapidly slipped into the atmosphere. At last, the annealed films were transferred to an argon-filled glovebox (GS Mega Line, O_2 < 0.6 ppm, H_2O < 0.2 ppm) for characterization via AFM and KPFM.

Preparation of cesium formamidinium lead triiodide ($Cs_{0.15}FA_{0.85}PbI_3$) thin films was performed analogously to the procedure described in the previous paragraph. The parameters were occasionally altered to a two-step spinning program (3000 rpm for 10 s and 5000 rpm for 30 s) or annealing at 170 °C for 15 min. A detailed summary of the preparation parameters is given in Table 6.2.

Table 6.2. List of parameters used for perovskite thin film synthesis.

perovskite composition	passivating agent (p.a.)	c(p.a.) [mol·L^{-1}]	speed program ω, t, α [rpm, s, rpm·s^{-1}]	T_{anneal} [°C]
$MAPbI_3$	-	-	4500, 20, 4400	120
$MAPbI_3$	TEOS	0.135	4500, 20, 4400	120
$MAPbI_3$	APTES	0.135	4500, 20, 4400	120
$MAPbI_3$	RbI	0.200	4500, 20, 4400	120
$MAPbI_3$	KI	0.200	4500, 20, 4400	120
$MAPbI_3$	PEAI	0.015	4500, 20, 4400	120
$Cs_{0.15}FA_{0.85}PbI_3$	-	-	4500, 20, 4400	170
$Cs_{0.15}FA_{0.85}PbI_3$	TEOS	0.135	3000, 10, 2970 5000, 30, 4950	170
$Cs_{0.15}FA_{0.85}PbI_3$	APTES	0.135	4500, 20, 4400	170
$Cs_{0.15}FA_{0.85}PbI_3$	RbI	0.200	4500, 20, 4400	120
$Cs_{0.15}FA_{0.85}PbI_3$	KI	0.200	4500, 20, 4400	120
$Cs_{0.15}FA_{0.85}PbI_3$	PEAI	0.015	4500, 20, 4400	120

6.4 Solar Cell Preparation

(a) Zinc Etching

For PSC preparation in planar n-i-p architecture, fluorine doped tin oxide (FTO) coated glass substrates (Sigma Aldrich, 25 mm × 25 mm, R_S = 7 Ω/sq) were used. For the etching of the surface, the whole active area besides an approximately 5-mm-wide stripe on the edge was covered with acid-resistant Capton tape. The remaining area was covered uniformly with zinc powder and 1 M hydrochloric acid (~0.4 mL per substrate) was dropped on top. After 1 min reaction time, the substrates were rinsed with deionized water. Subsequently, the surface was thoroughly cleaned first with Hellmanex under a stream of hot tap water, and second with Milli-Q water ($\rho \geq 12$ MΩ·cm^{-1}), before being subjected to 30 min of argon-plasma treatment (TePla 200-G Plasma System) at 0.2 mbar Ar-pressure and 270 W power.

(b) Titanium Dioxide Layer

For the deposition of a ~100 nm thick compact titanium dioxide layer, a 2 M solution of titanium(IV) chloride, prepared according to the literature and stored at –15 °C,[60] was diluted to 0.75 M with cooled Milli-Q water (ρ = 18.2 MΩ·cm^{-1}) and filtered through a hydrophobic PTFE syringe filter (0.22 µm pore size). Before spin-coating (Headway Research) under ambient conditions, an approximately 5-mm-wide stripe opposite to the previously etched area of each argon-plasma cleaned FTO substrate was covered with scotch tape. Afterwards, 90 µL of the 0.75 M titanium(IV) chloride solution was dropped onto the center of the surface, and the plate was spun at 5000 rpm for 30 s. Upon removal of the scotch tape, the films were dried on a hotplate (Heidolph MR2002) at 150 °C for 10 min and annealed in a titanium oven at 500 °C for 30 min.

(c) Perovskite Layer

The substrates were then subjected to an additional UV-ozone treatment before the perovskite layer deposition was carried out according to the procedure described in Section 6.3 and the parameters stated in Table 6.2.

(d) Spiro-OMeTAD Layer

In a nitrogen-filled glovebox, 72.3 mg (0.06 mmol) of spiro-OMeTAD were dissolved in 1 mL of chlorobenzene. To this solution, 28.8 µL (0.20 mmol) of 4-*tert*-butylpyridine and 17.5 µL of a 1.8 M solution of lithium bis(trifluoromethanesulfonyl)imide (LiTFSI) in acetonitrile (0.03 mmol) were added. The mixture was then agitated, filtered through a PTFE syringe filter (0.22 µm pore size) and aged in daylight for approximately 3 h. Dynamic spin-coating of the perovskite-coated substrates was performed in the nitrogen-filled glovebox. While spinning at 4000 rpm for 20 s, 90 µL of the *p*-doped spiro-OMeTAD solution was applied rapidly between the 8th and the 9th second of the program. After the deposition, the substrates were transferred immediately into a desiccator ($\phi_{H2O} = 4.5\%$) overnight.

(e) Gold Electrode

As the final step, gold electrodes were deposited via thermal evaporation technique at a maximum rate of 1.5 Å·s^{-1} (Edwards FL400) on top of the spiro-OMeTAD layer using appropriately shaped retainer masks. Thereby, three electric contacts could be generated on each substrate.

6.5 Experiments

6.5.1 ^{29}Si-NMR Study on Precursor Solution of TEOS $Cs_{0.15}FA_{0.85}PbI_3$

Lead(II) iodide (461.1 mg, 1.00 mmol), FAI (146.2 mg, 0.85 mmol), cesium iodide (39.0 mg, 0.15 mmol) and DSS (10.9 mg, 0.05 mmol) were dissolved in 1 mL of a mixture of DMF/DMSO (5:1 v/v). TEOS (30 µL, 0.135 mmol) and water (6.0 µL, 0.30 mmol) were added. The solution was agitated for 1 min and filtered through a PTFE syringe filter (0.22 µm pore size) before NMR analysis.

^{1}H-NMR (500 MHz, DMF/DMSO 5:1 v/v, t = 1 h): δ = 8.96 (s, NH_2, FAI), 8.11 (s, CH, FAI), 8.03 (s, CHO, DMF), 3.78-3.73 (q, 23.59H, $^3J_{HH}$ = 7.0 Hz, CH_2, TEOS), 3.67 (s, 15.01H, H_2O), 2.97 (s, CH_3, DMF), 2.78 (s, CH_3, DMF), 2.70 (s, CH_3, DMSO), 1.71-1.61 (m, 2H, DSS), 1.17-1.13 (t, 34.06H, $^3J_{HH}$ = 7.0 Hz, CH_3, TEOS), 0.58-0.51 (m, 2H, DSS), –0.05 (s, 9H, DSS) ppm.

^{1}H-NMR (500 MHz, DMF/DMSO 5:1 v/v, t = 20 h): δ = 8.96 (s, NH_2, FAI), 8.11 (s, CH, FAI), 8.03 (s, CHO, DMF), 3.78-3.73 (q, 23.42H, $^3J_{HH}$ = 7.0 Hz, CH_2, TEOS), 3.67 (s, 14.83H, H_2O), 3.53-3.46 (q, 0.97H, $^3J_{HH}$ = 7.0 Hz, CH_2, EtOH), 2.97 (s, CH_3, DMF), 2.78 (s, CH_3, DMF), 2.70 (s, CH_3, DMSO), 1.71-1.61 (m, 2H, DSS), 1.17-1.13 (t, 33.41H, $^3J_{HH}$ = 7.0 Hz, CH_3, TEOS), 1.07-1.04 (t, 0.98H, $^3J_{HH}$ = 7.0 Hz, CH_3, EtOH), 0.58-0.51 (m, 2H, DSS), –0.05 (s, 9H, DSS) ppm.

^{29}Si-NMR (100 MHz, INEPT, DMF/DMSO 5:1 v/v, t = 1 h): δ = 1.20 (DSS), –81.76 (s, Q^0_R) ppm.

^{29}Si-NMR (100 MHz, INEPT, DMF/DMSO 5:1 v/v, t = 20 h): δ = 1.20 (DSS), –81.76 (s, Q^0_R) ppm.

6.5.2 ^{29}Si-NMR Study on Precursor Solution of APTES Cs$_{0.15}$FA$_{0.85}$PbI$_3$

Lead(II) iodide (461.1 mg, 1.00 mmol), FAI (146.2 mg, 0.85 mmol), cesium iodide (39.0 mg, 0.15 mmol) and DSS (10.9 mg, 0.05 mmol) were dissolved in 1 mL of a mixture of DMF/DMSO (5:1 v/v). APTES (31.7 μL, 0.135 mmol) and water (6.0 μL, 0.30 mmol) were added. The solution was agitated for 1 min and filtered through a PTFE syringe filter (0.22 μm pore size) before NMR analysis.

^{1}H-NMR (500 MHz, DMF/DMSO 5:1 v/v, t = 45 min): δ = 8.12 (s, CH, FAI), 8.03 (s, CHO, DMF), 3.80-3.72 (q, 14.65H, $^3J_{HH}$ = 7.0 Hz, CH_2^{Et}, APTES), 3.53-3.46 (q, 4.59H, $^3J_{HH}$ = 7.0 Hz, CH_2, EtOH), 3.39-3.34 (t, 4.53H, $^3J_{HH}$ = 6.98 Hz, CH_2^{Pr}, APTES), 2.97 (s, CH_3, DMF), 2.78 (s, CH_3, DMF), 2.69 (s, CH_3, DMSO), 1.72-1.60 (m, 2H, DSS; 4.72H, CH_2^{Pr}, APTES), 1.21-1.11 (t, 21.91H, $^3J_{HH}$ = 7.0 Hz, CH_3^{Et}, APTES), 1.09-1.04 (t, 5.15H, $^3J_{HH}$ = 7.0 Hz, CH_3, EtOH), 0.67-0.62 (m, 3.89H, CH_2^{Pr}, APTES), 0.59-0.46 (m, 2H, DSS), –0.05 (s, 9H, DSS) ppm.

^{1}H-NMR (500 MHz, DMF/DMSO 5:1 v/v, t = 47 h): δ = 8.11 (s, CH, FAI), 8.03 (s, CHO, DMF), 3.53-3.46 (q, 19.15H, $^3J_{HH}$ = 7.0 Hz, CH_2, EtOH), 2.97 (s, CH_3, DMF), 2.78 (s, CH_3, DMF), 2.69 (s, CH_3, DMSO), 1.75-1.61 (m, 2H, DSS; 5.04H, CH_2^{Pr}, APTES), 1.09-1.04 (t, 25.25H, $^3J_{HH}$ = 7.0 Hz, CH_3, EtOH), 0.57-0.52 (m, 2H, DSS), –0.05 (s, 9H, DSS) ppm.

^{29}Si-NMR (100 MHz, INEPT, DMF/DMSO 5:1 v/v, t = 1 h): δ = 1.20 (DSS), –45.85 (s, T^0_H), –45.91 (s, T^0_H), –46.07 (s, T^0_R), –46.11 (s, T^0_H), –57.05 (T^2) ppm.

^{29}Si-NMR (100 MHz, INEPT, DMF/DMSO 5:1 v/v, t = 20 h): δ = 1.20 (DSS), –46.05 (s, T^0_R), –57.05 (s, T^2), –68.43 (s, T^3) ppm.

^{29}Si-NMR (100 MHz, INEPT, DMF/DMSO 5:1 v/v, t = 47 h): δ = 1.20 (DSS), –57.07 (s, T^2), –66.6 (s, T^3), –68.33 (s, T^3), –68.44 (s, T^3), –68.52 (s, T^3) ppm.

6.5.3 Synthesis of 2-Phenylethylammonium Iodide
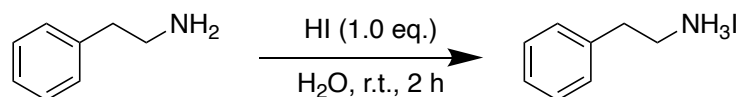
Hydroiodic acid (10 mL of a 57 wt% solution in water, 75.7 mmol, 1 equiv.) were cooled to 0 °C in an ice bath. 2-Phenylethylamine (9.52 mL, 75.7 mmol, 1 equiv.) were slowly dropped into the solution under vigorous stirring. After 2 h, the solvent was evaporated at 80 °C and 150 mbar. The obtained solid was washed with diethyl ether and dried under vacuum at 90 °C to yield 2-phenylethylammonium iodide (69.6 mmol, 92 % yield).

¹H-NMR (300 MHz, DMSO): δ = 7.76 (s, 3H, NH_3), 7.38-7.22 (m, 5H, H^{ar}), 3.10-3.00 (dd, 2H, $^2J_{HH}$ = 6 Hz, $^2J_{HH}$ = 3 Hz, CH_2NH$_3$), 2.90-2.80 (dd, 2H, $^2J_{HH}$ = 6.0 Hz, $^2J_{HH}$ = 3.0 Hz, CH_2) ppm.

¹³C-NMR (75 MHz, DMSO): δ = 137.18 (s, C_{quart}), 128.66 (s, C_{ortho}), 128.61 (s, C_{meta}), 126.75 (s, C_{para}), 39.94 (s, CH$_2$NH$_3$), 32.99 (s, CH$_2$) ppm.

6.6 Calculations

6.6.1 Integral Ratios in NMR Spectroscopy

The molar concentrations of the reacting compounds were calculated according to Equation 9. The integral of the signal at –0.05 ppm of the internal standard DSS (I_{stand}) was set to a value of 9, coinciding with the number of H (N_{stand}). The molar concentration of the standard (M_{stand}) was 0.05 M.

(9) $$M_x = \frac{I_x}{I_{stand}} \cdot \frac{N_{stand}}{N_x} \cdot M_{stand}$$

M: molar concentration

I: integral

N: number of H

6.6.2 Tolerance Factor

The Goldschmidt tolerance factor t is defined according to Equation 10.[23]

(10) $$t = \frac{r_A + r_X}{\sqrt{2}(r_B + r_X)}$$

t: tolerance factor

r: ionic radius

The ionic radii of the ions relevant for this work are listed in Table 6.3. Stability of the cubic perovskite structure is empirically provided for a tolerance factor between 0.8 and 1.0. Larger or smaller values lead to non-perovskite crystal structures.[31]

Table 6.3. Crystal ionic radii of the constituent ions used within this work. Values taken from ref. [61] and [62].

ion	formula	crystal ionic radius [pm]
lead	Pb^{+II}	133
cesium	Cs^+	181
rubidium	Rb^+	166
potassium	K^+	152
methylammonium	$[CH_3NH_3]^+$	217
formamidinium	$[NH_2CHNH_2]^+$	253
iodide	I^-	220

6.6.3 Tauc Plot Protocol

In this section, the determination of direct bandgap energies E_g as well as Urbach energies E_U is described. Assuming that the Tauc relation in Equation 11 holds, one can plot – after rearrangement – the expression $(\alpha h\nu)^{1/n}$ against the energy E of the incident light.[63] The bandgap energy E_g will then be the intercept with the abscissa of the regression of the linear regime corresponding to the absorption edge in question. The different plots are shown in Figure 6.1 and Figure 6.2 for $MAPbI_3$ films and $Cs_{0.15}FA_{0.85}PbI_3$ films, respectively.

$$(11) \qquad \alpha h\nu = A\left(h\nu - E_g\right)^n$$

α: absorption coefficient

h: Planck constant

ν: incident light frequency

A: band edge sharpness constant

E_g: bandgap energy

n: = 0.5 for direct bandgap
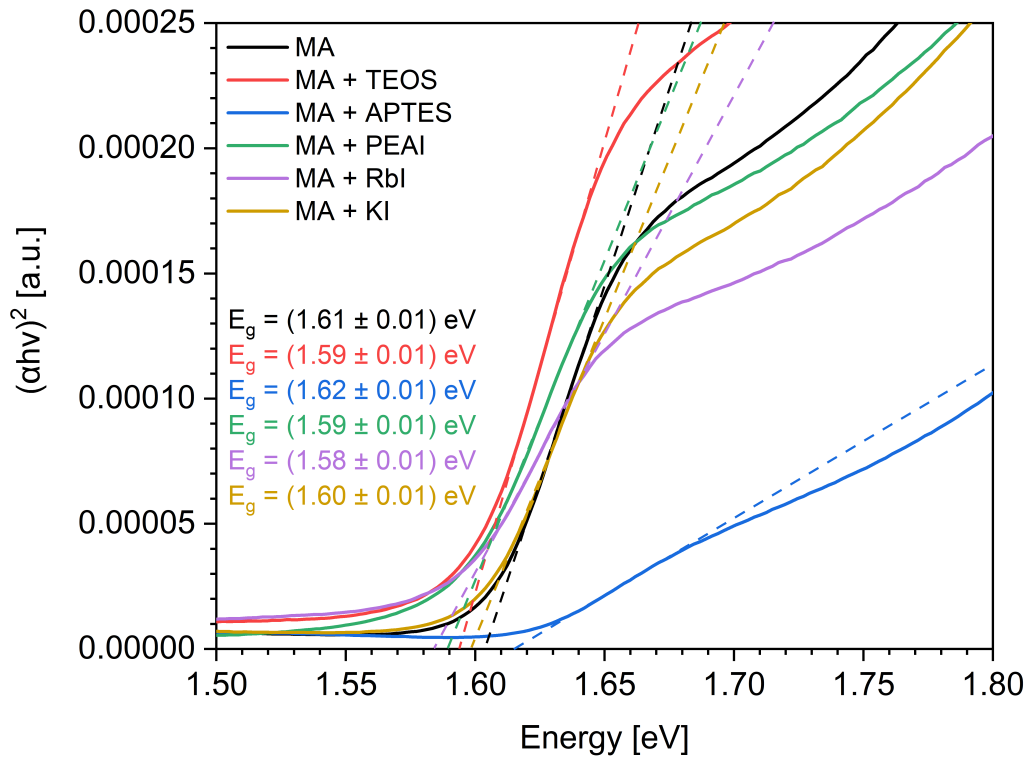
Figure 6.1. Extrapolation of the linear regime of the first absorption edge of differently passivated MAPbI$_3$ films to the abscissa in a Tauc plot of the direct bandgap ($n = 0.5$) using linear regression.
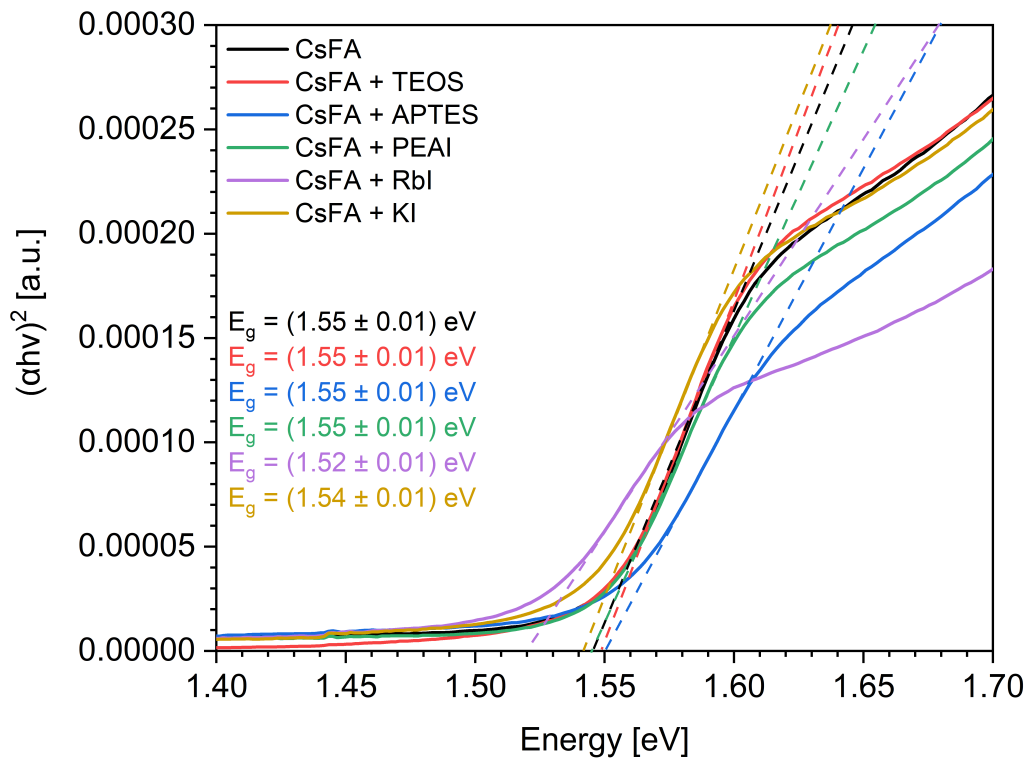

Figure 6.2 Extrapolation of the linear regime of the first absorption edge of differently passivated Cs$_{0.15}$FA$_{0.85}$PbI$_3$ films to the abscissa in a Tauc plot of the direct bandgap ($n = 0.5$) using linear regression.

In order to determine the Urbach energy E_U as an optically determined measure for sub-bandgap absorption due to defect states, absorption coefficients are first calculated according to Equation 12.

$$(12) \qquad \alpha = \frac{4\pi \cdot k}{\lambda}$$

k: extinction

λ: wavelength

E_U can then be extracted according to Equation 13 by plotting the expression $ln(\alpha)$ against the energy E.[64] The Urbach energy will be the inverse of the slope of the linear regime corresponding to the first absorption edge, as shown in Figure 6.3 and Figure 6.4.

$$(13) \qquad \alpha = \alpha_0 \cdot \exp\left(\frac{E}{E_U}\right)$$

E_U: Urbach energy
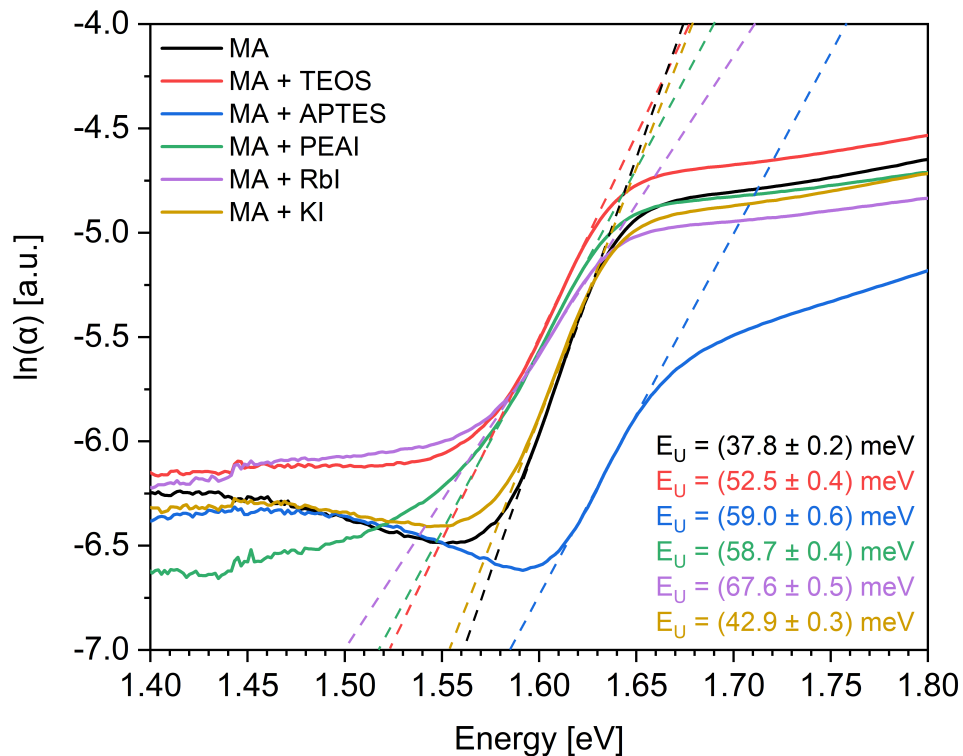
Figure 6.3. Determination of the slope of the linear regime of the first absorption edge of differently passivated MAPbI$_3$ films in an Urbach plot using linear regression.
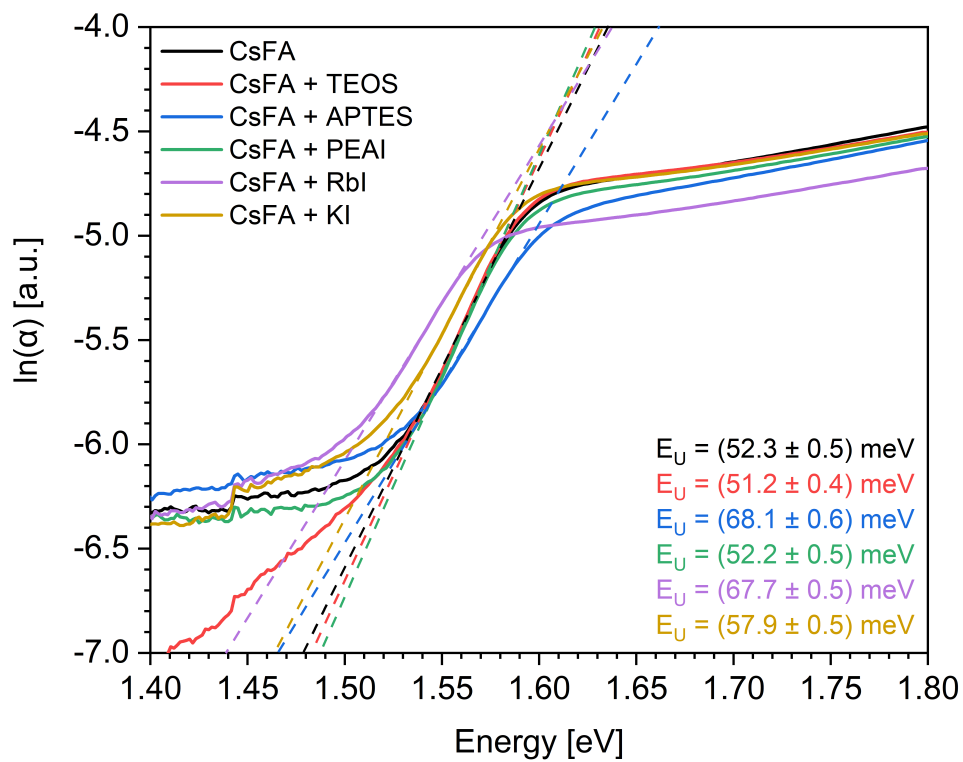
Figure 6.4. Determination of the slope of the linear regime of the first absorption edge of differently passivated $Cs_{0.15}FA_{0.85}PbI_3$ films in an Urbach plot using linear regression.

7 References

[1]   O. Tschauner, C. Ma, J. R. Beckett, C. Prescher, V. B. Prakapenka, G. R. Rossman, *Science* **2014,** *346*, 1100-1102.

[2]   A. Kojima, K. Teshima, Y. Shirai, T. Miyasaka, *Journal of the American Chemical Society* **2009,** *131*, 6050-6051.

[3]   B. Chen, P. N. Rudd, S. Yang, Y. Yuan, J. Huang, *Chemical Society Reviews* **2019,** *48*, 3842-3867.

[4]   The National Renewable Energy Laboratory (NREL), Best Research-Cell Efficiency Chart, URL: *https://www.nrel.gov/pv/cell-efficiency.html,* retrieved: 24.11.2020.

[5]   W. Shockley, H. J. Queisser, *Journal of Applied Physics* **1961,** *32*, 510-519.

[6]   S. Rühle, *Solar Energy* **2016,** *130*, 139-147.

[7]   M. V. Kovalenko, L. Protesescu, M. I. Bodnarchuk, *Science* **2017,** *358*, 745-750.

[8]   L. Meng, J. You, Y. Yang, *Nature Communications* **2018,** *9*, 5265.

[9]   V. D'Innocenzo, G. Grancini, M. J. P. Alcocer, A. R. S. Kandada, S. D. Stranks, M. M. Lee, G. Lanzani, H. J. Snaith, A. Petrozza, *Nature Communications* **2014,** *5*, 3586.

[10]   A. Uddin, *Perovskite Solar Cells*, In: J. Huang, Y. Yuan (Eds.), World Scientific Handbook of Organic Optoelectronic Devices, World Scientific, **2018**, Vol. 1, pp 285-367.

[11]   S. S. Lim, T. C. Sum, *The Photophysics of Halide Perovskite Thin Films*, In: J. Huang, Y. Yuan (Eds.), World Scientific Handbook of Organic Optoelectronic Devices, World Scientific, **2018**, Vol. 1, pp 113-139.

[12]   W.-J. Yin, T. Shi, Y. Yan, *Applied Physics Letters* **2014,** *104*, 063903.

[13]   D. W. de Quilettes, S. M. Vorpahl, S. D. Stranks, H. Nagaoka, G. E. Eperon, M. E. Ziffer, H. J. Snaith, D. S. Ginger, *Science* **2015,** *348*, 683-686.

[14]   J. S. Yun, A. Ho-Baillie, S. Huang, S. H. Woo, Y. Heo, J. Seidel, F. Huang, Y.-B. Cheng, M. A. Green, *The Journal of Physical Chemistry Letters* **2015,** *6*, 875-880.

[15]   B. Philippe, B.-W. Park, R. Lindblad, J. Oscarsson, S. Ahmadi, E. M. J. Johansson, H. Rensmo, *Chemistry of Materials* **2015,** *27*, 1720-1731.

[16]   D. Li, S. A. Bretschneider, V. W. Bergmann, I. M. Hermes, J. Mars, A. Klasen, H. Lu, W. Tremel, M. Mezger, H.-J. Butt, S. A. L. Weber, R. Berger, *The Journal of Physical Chemistry C* **2016,** *120*, 6363-6368.

[17]   A. Latini, G. Gigli, A. Ciccioli, *Sustainable Energy & Fuels* **2017,** *1*, 1351-1357.

[18]   E. Smecca, Y. Numata, I. Deretzis, G. Pellegrino, S. Boninelli, T. Miyasaka, A. La Magna, A. Alberti, *Physical Chemistry Chemical Physics* **2016,** *18*, 13413-13422.

[19]   J. Huang, Y. Yuan, Y. Shao, Y. Yan, *Nature Reviews Materials* **2017,** *2*, 17042.

[20]   T. Kirchartz, *Philosophical Transactions of the Royal Society A: Mathematical, Physical and Engineering Sciences* **2019,** *377*, 20180286.

[21]   T. Liu, Y. Zhou, Z. Li, L. Zhang, M.-G. Ju, D. Luo, Y. Yang, M. Yang, D. H. Kim, W. Yang, N. P. Padture, M. C. Beard, X. C. Zeng, K. Zhu, Q. Gong, R. Zhu, *Advanced Energy Materials* **2018,** *8*, 1800232.

[22]   I. C. Smith, E. T. Hoke, D. Solis-Ibarra, M. D. McGehee, H. I. Karunadasa, *Angewandte Chemie International Edition* **2014,** *53*, 11232-11235.

[23]   D. B. Mitzi, *Synthesis, Structure, and Properties of Organic-Inorganic Perovskites and Related Materials*, In: K. D. Karlin (Ed.), Progress in Inorganic Chemistry, John Wiley & Sons, New York, **1999**, Vol. 48, pp 1-121.

[24]   N. R. Venkatesan, R. M. Kennard, R. A. DeCrescent, H. Nakayama, C. J. Dahlman, E. E. Perry, J. A. Schuller, M. L. Chabinyc, *Chemistry of Materials* **2018,** *30*, 8615-8623.

[25]   A. S. Thind, G. Luo, J. A. Hachtel, M. V. Morrell, S. B. Cho, A. Y. Borisevich, J.-C. Idrobo, Y. Xing, R. Mishra, *Advanced Materials* **2019,** *31*, 1805047.

[26]   C. Liang, D. Zhao, Y. Li, X. Li, S. Peng, G. Shao, G. Xing, *Energy & Environmental Materials* **2018,** *1*, 221-231.

[27]   M. Abdi-Jalebi, Z. Andaji-Garmaroudi, S. Cacovich, C. Stavrakas, B. Philippe, J. M. Richter, M. Alsari, E. P. Booker, E. M. Hutter, A. J. Pearson, S. Lilliu, T. J. Savenije, H. Rensmo, G. Divitini, C. Ducati, R. H. Friend, S. D. Stranks, *Nature* **2018,** *555*, 497-501.

[28]   M. Saliba, T. Matsui, K. Domanski, J.-Y. Seo, A. Ummadisingu, S. M. Zakeeruddin, J.-P. Correa-Baena, W. R. Tress, A. Abate, A. Hagfeldt, M. Grätzel, *Science* **2016,** *354*, 206-209.

[29]   D. J. Kubicki, D. Prochowicz, A. Hofstetter, S. M. Zakeeruddin, M. Grätzel, L. Emsley, *Journal of the American Chemical Society* **2017,** *139*, 14173-14180.

[30]   G. E. Eperon, S. D. Stranks, C. Menelaou, M. B. Johnston, L. M. Herz, H. J. Snaith, *Energy & Environmental Science* **2014,** *7*, 982-988.

[31]   Z. Li, M. Yang, J.-S. Park, S.-H. Wei, J. J. Berry, K. Zhu, *Chemistry of Materials* **2016,** *28*, 284-292.

[32]   C. C. Stoumpos, C. D. Malliakas, M. G. Kanatzidis, *Inorganic Chemistry* **2013,** *52*, 9019-9038.

[33]   A. Axt, I. M. Hermes, V. W. Bergmann, N. Tausendpfund, S. A. Weber, *Beilstein Journal of Nanotechnology* **2018,** *9*, 1809-1819.

[34]   Z. Kang, H. Si, M. Shi, C. Xu, W. Fan, S. Ma, A. Kausar, Q. Liao, Z. Zhang, Y. Zhang, *Science China Materials* **2019,** *62*, 776-789.

[35]   R. Sydam, R. K. Kokal, M. Deepa, *ChemPhysChem* **2015,** *16*, 1042-1051.

[36]   S. Sadewasser, T. Glatzel, *Experimantal Technique and Working Modes*, In: S. Sadewasser, T. Glatzel (Eds.), Kelvin Probe Force Microscopy, Springer International Publishing, **2018**, Vol. 65, pp 3-22.

[37]   B. Grévin, *Kelvin Probe Force Microscopy Characterization of Organic and Hybrid Perovskite Solar Cells*, In: S. Sadewasser, T. Glatzel (Eds.), Kelvin Probe Force Microscopy, Springer International Publishing, **2018**, Vol. 65, pp 331-365.

[38]   A. Henning, Y. Rosenwaks, *KPFM of Nanostructured Electrochemical Sensors*, In: S. Sadewasser, T. Glatzel (Eds.), Kelvin Probe Force Microscopy, Springer International Publishing, **2018**, Vol. 65, pp 367-389.

[39]   D. Kim, J.-H. Yun, M. Lyu, J. Kim, S. Lim, J. S. Yun, L. Wang, J. Seidel, *The Journal of Physical Chemistry C* **2019,** *123*, 14144-14151.

[40]   H. D. Kim, H. Ohkita, H. Benten, S. Ito, *Advanced Materials* **2016,** *28*, 917-922.

[41]   P. Kaienburg, P. Hartnagel, B. E. Pieters, J. Yu, D. Grabowski, Z. Liu, J. Haddad, U. Rau, T. Kirchartz, *The Journal of Physical Chemistry C* **2018,** *122*, 27263-27272.

[42]   G. Li, K. L. Ching, J. Y. L. Ho, M. Wong, H.-S. Kwok, *Advanced Energy Materials* **2015,** *5*, 1401775.

[43]   M.-C. Brochier Salon, P.-A. Bayle, M. Abdelmouleh, S. Boufi, M. N. Belgacem, *Colloids and Surfaces A: Physicochemical and Engineering Aspects* **2008,** *312*, 83-91.

[44]   S. De Wolf, J. Holovsky, S.-J. Moon, P. Löper, B. Niesen, M. Ledinsky, F.-J. Haug, J.-H. Yum, C. Ballif, *The Journal of Physical Chemistry Letters* **2014,** *5*, 1035-1039.

[45]   B. Luo, Y.-C. Pu, S. A. Lindley, Y. Yang, L. Lu, Y. Li, X. Li, J. Z. Zhang, *Angewandte Chemie International Edition* **2016,** *55*, 8864-8868.

[46]   J. T.-W. Wang, Z. Wang, S. Pathak, W. Zhang, D. W. deQuilettes, F. Wisnivesky-Rocca-Rivarola, J. Huang, P. K. Nayak, J. B. Patel, H. A. Mohd Yusof, Y. Vaynzof, R. Zhu, I. Ramirez, J. Zhang, C. Ducati, C. Grovenor, M. B. Johnston, D. S. Ginger, R. J. Nicholas, H. J. Snaith, *Energy & Environmental Science* **2016,** *9*, 2892-2901.

[47]   S. Zhang, S. M. Hosseini, R. Gunder, A. Petsiuk, P. Caprioglio, C. M. Wolff, S. Shoaee, P. Meredith, S. Schorr, T. Unold, P. L. Burn, D. Neher, M. Stolterfoht, *Advanced Materials* **2019,** *31*, 1901090.

[48] M. Abdi-Jalebi, Z. Andaji-Garmaroudi, A. J. Pearson, G. Divitini, S. Cacovich, B. Philippe, H. Rensmo, C. Ducati, R. H. Friend, S. D. Stranks, *ACS Energy Letters* **2018,** *3*, 2671-2678.

[49] Y. Yamada, M. Hoyano, K. Oto, Y. Kanemitsu, *Physica Status Solidi B* **2019,** *256*, 1800545.

[50] D.-Y. Son, S.-G. Kim, J.-Y. Seo, S.-H. Lee, H. Shin, D. Lee, N.-G. Park, *Journal of the American Chemical Society* **2018,** *140*, 1358-1364.

[51] S. Akin, E. Akman, S. Sonmezoglu, *Advanced Functional Materials* **2020,** *30*, 2002964.

[52] S. Masi, A. F. Gualdrón-Reyes, I. Mora-Seró, *ACS Energy Letters* **2020,** *5*, 1974-1985.

[53] J. Zhang, C. Xie, G. Li, P. Dai, L. Yang, R. Liu, B. Pan, *The Journal of Chemical Physics* **2019,** *151*, 134104.

[54] G. Paul, S. Chatterjee, H. Bhunia, A. J. Pal, *The Journal of Physical Chemistry C* **2018,** *122*, 20194-20199.

[55] K. Wang, T. Wu, C. Wu, R. Sriramdas, X. Huang, K. Wang, Y. Jiang, H. Liu, Y. Yan, D. Yang, T. Ye, C. Liu, X. Hu, X. Jiang, S. Priya, *Journal of Materials Chemistry A* **2020,** *8*, 7659-7670.

[56] C. M. M. Soe, W. Nie, C. C. Stoumpos, H. Tsai, J.-C. Blancon, F. Liu, J. Even, T. J. Marks, A. D. Mohite, M. G. Kanatzidis, *Advanced Energy Materials* **2018,** *8*, 1700979.

[57] I. M. Hermes, S. A. Bretschneider, V. W. Bergmann, D. Li, A. Klasen, J. Mars, W. Tremel, F. Laquai, H.-J. Butt, M. Mezger, R. Berger, B. J. Rodriguez, S. A. L. Weber, *The Journal of Physical Chemistry C* **2016,** *120*, 5724-5731.

[58] Z. Zhu, V. G. Hadjiev, Y. Rong, R. Guo, B. Cao, Z. Tang, F. Qin, Y. Li, Y. Wang, F. Hao, S. Venkatesan, W. Li, S. Baldelli, A. M. Guloy, H. Fang, Y. Hu, Y. Yao, Z. Wang, J. Bao, *Chemistry of Materials* **2016,** *28*, 7385-7393.

[59] T. Leijtens, G. E. Eperon, A. J. Barker, G. Grancini, W. Zhang, J. M. Ball, A. R. S. Kandada, H. J. Snaith, A. Petrozza, *Energy & Environmental Science* **2016,** *9*, 3472-3481.

[60] A. Klasen, P. Baumli, Q. Sheng, E. Johannes, S. A. Bretschneider, I. M. Hermes, V. W. Bergmann, C. Gort, A. Axt, S. A. L. Weber, H. Kim, H.-J. Butt, W. Tremel, R. Berger, *The Journal of Physical Chemistry C* **2019,** *123*, 13458-13466.

[61] G. Kieslich, S. Sun, A. K. Cheetham, *Chemical Science* **2014,** *5*, 4712-4715.

[62] R. Shannon, *Acta Crystallographica Section A* **1976,** *32*, 751-767.

[63] J. Tauc, R. Grigorovici, A. Vancu, *Physica Status Solidi B* **1966,** *15*, 627-637.

[64] K. Boubaker, *The European Physical Journal Plus* **2011,** *126*, 10.
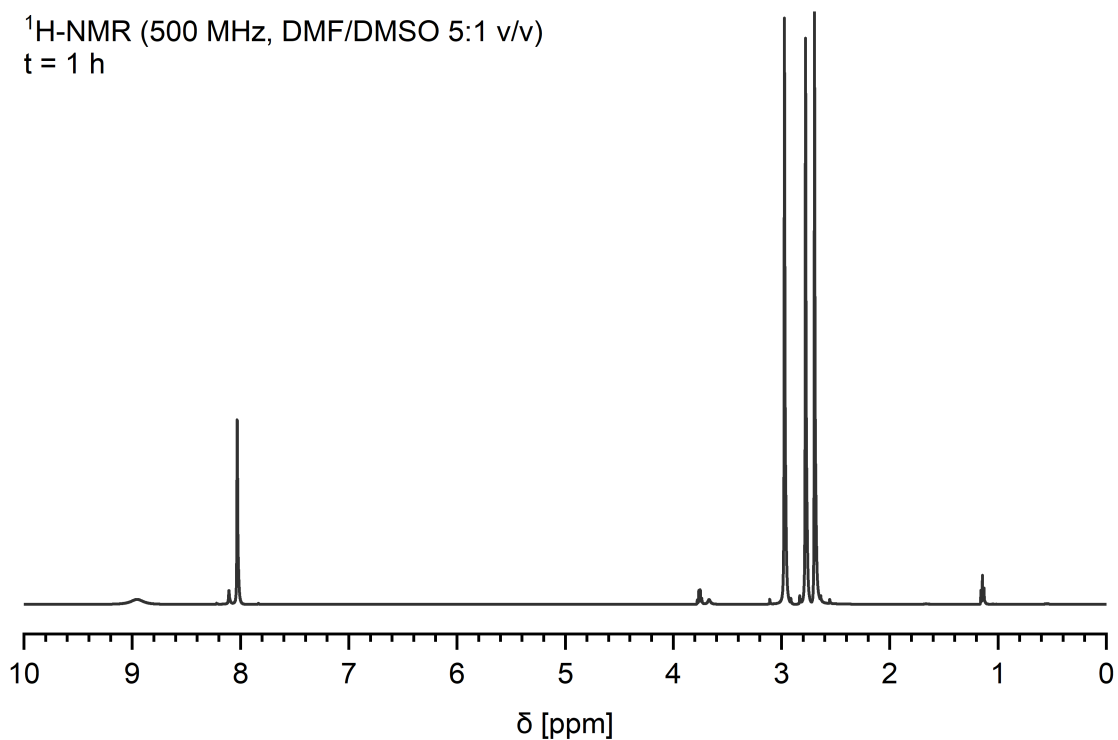
A Appendix

¹H-NMR (500 MHz, DMF/DMSO 5:1 v/v)
t = 1 h

Figure A.1 Full ^{1}H-NMR spectrum of a $Cs_{0.15}FA_{0.85}PbI_3$ precursor solution containing 0.135 M of TEOS and 0.3 M water after 1 h reaction time at 25 °C prepared according to ref. [21].
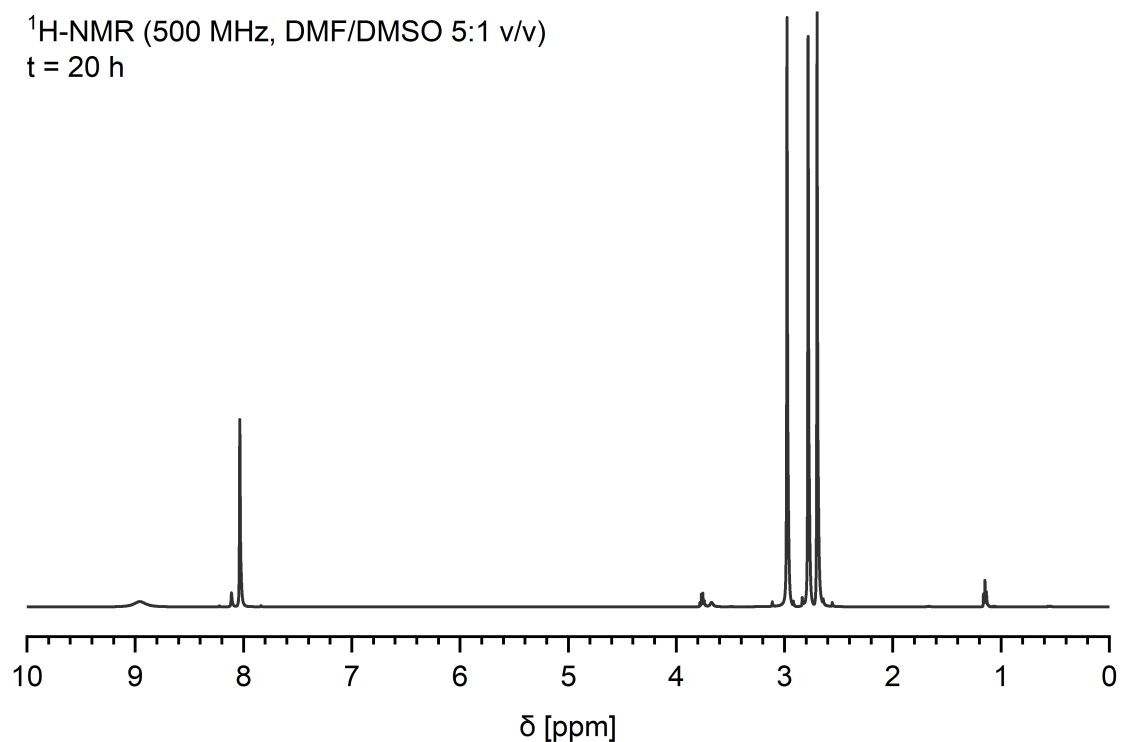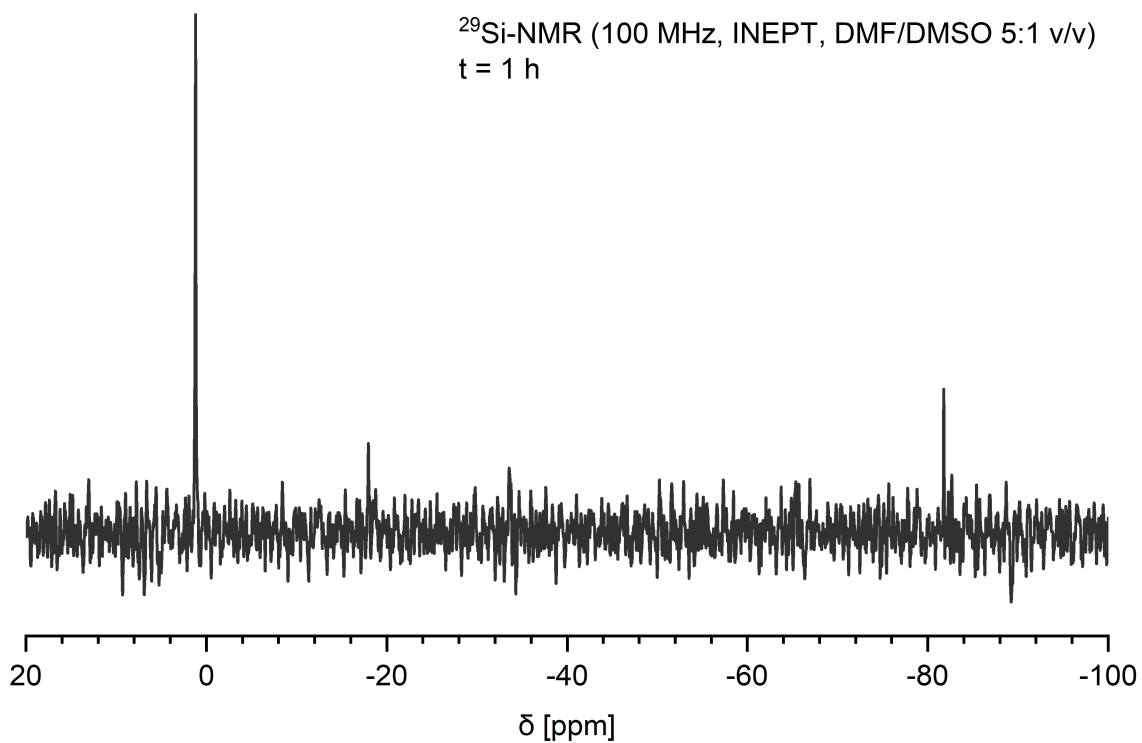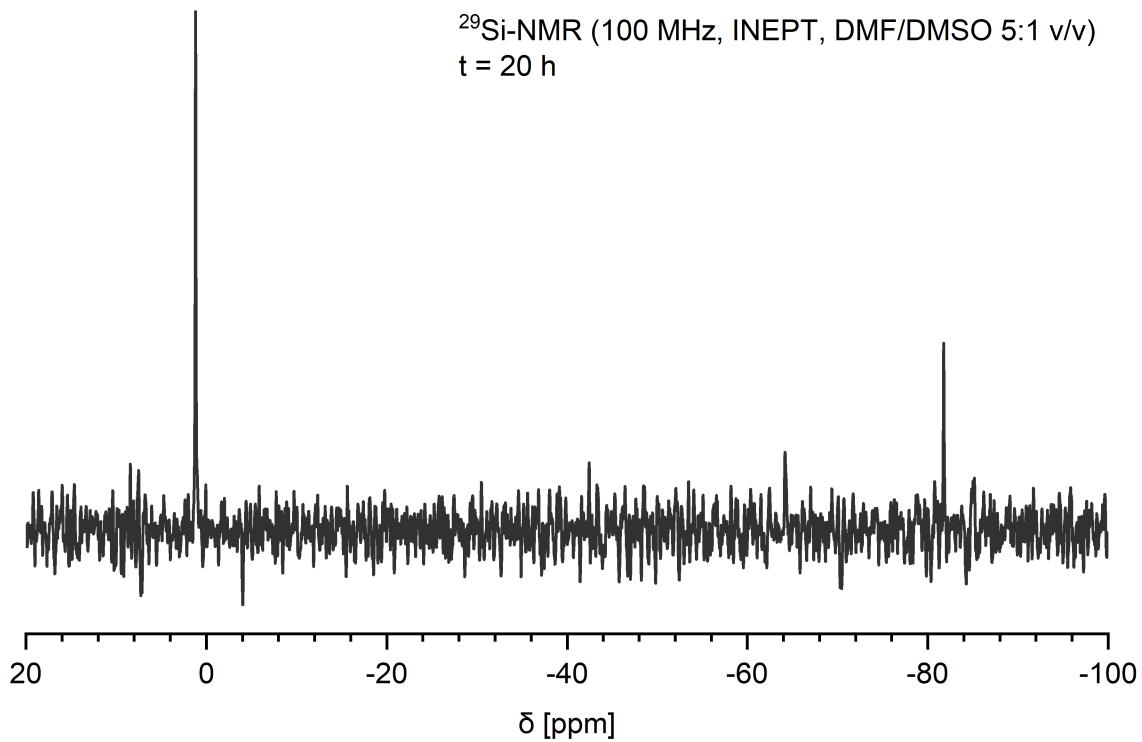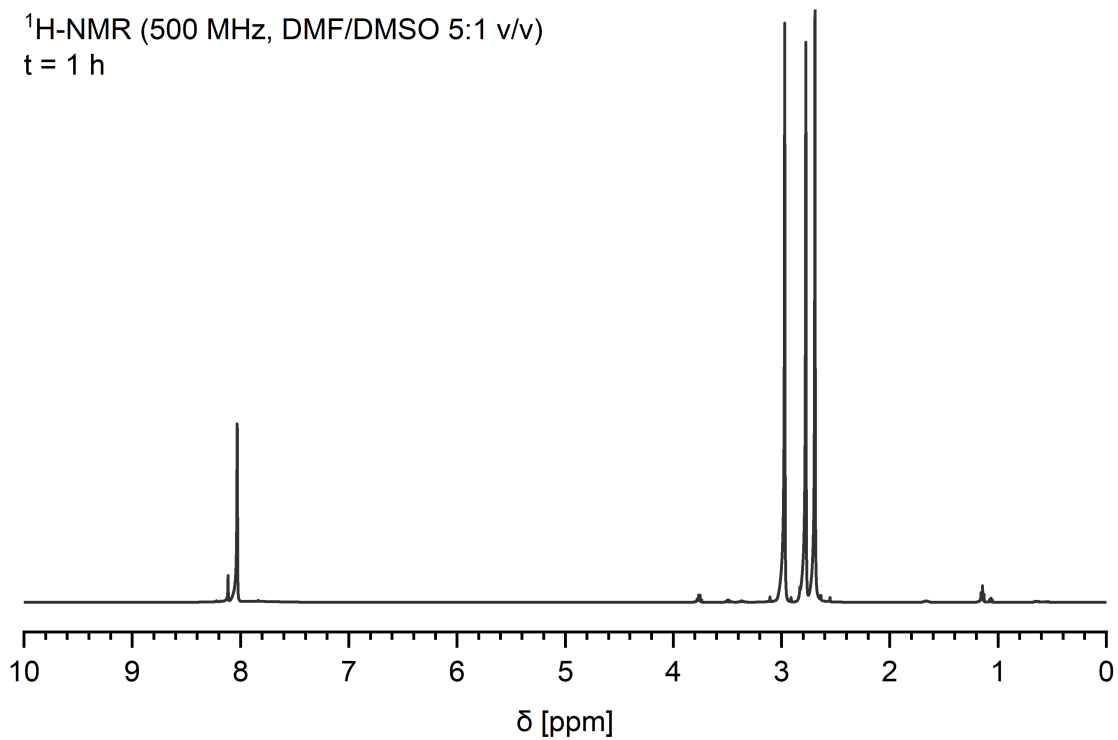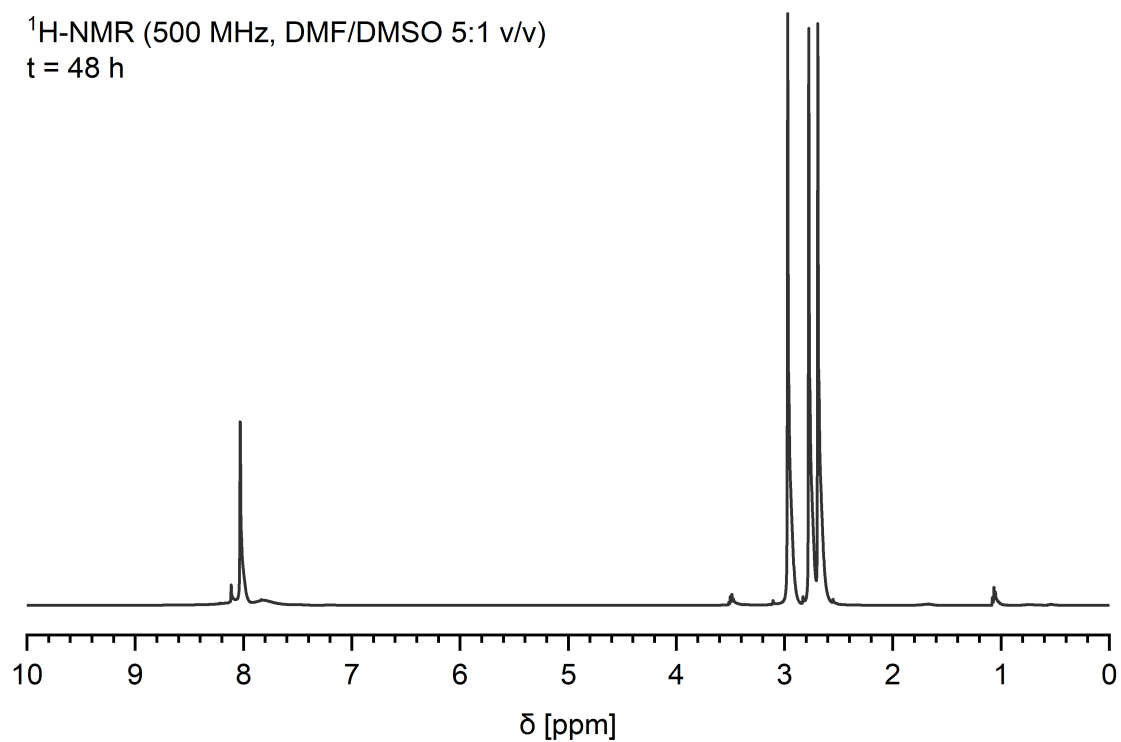
¹H-NMR (500 MHz, DMF/DMSO 5:1 v/v)
t = 20 h

Figure A.2. Full ^{1}H-NMR spectrum of a $Cs_{0.15}FA_{0.85}PbI_3$ precursor solution containing 0.135 M of TEOS and 0.3 M water after 20 h reaction time at 25 °C prepared according to ref. [21].

Figure A.3. Full ^{29}Si-NMR spectrum of a $Cs_{0.15}FA_{0.85}PbI_3$ precursor solution containing 0.135 M of TEOS and 0.3 M water after 1 h reaction time at 25 °C prepared according to ref. [21].

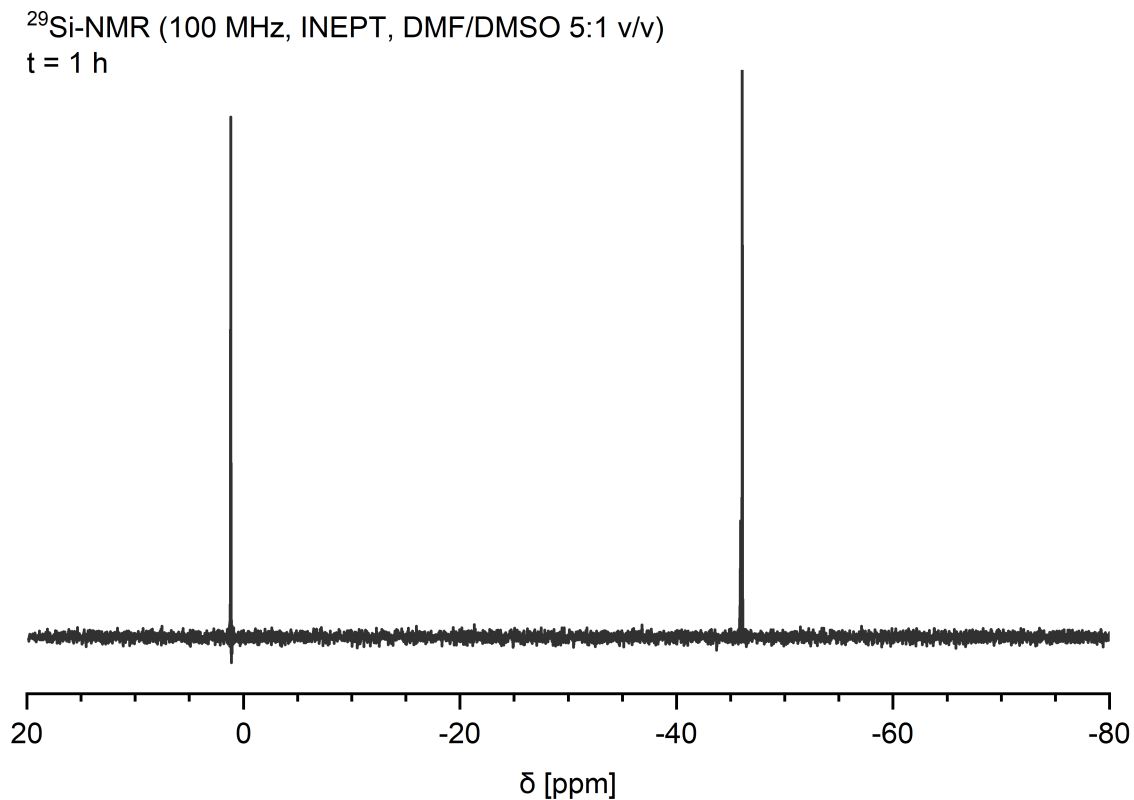**Figure A.4.** Full ^{29}Si-NMR spectrum of a $Cs_{0.15}FA_{0.85}PbI_3$ precursor solution containing 0.135 M of TEOS and 0.3 M water after 20 h reaction time at 25 °C prepared according to ref. [21].

Figure A.5. Full ^{1}H-NMR spectrum of a $Cs_{0.15}FA_{0.85}PbI_3$ precursor solution containing 0.135 M of APTES and 0.3 M water after 1 h reaction time at 25 °C prepared according to ref. [21].

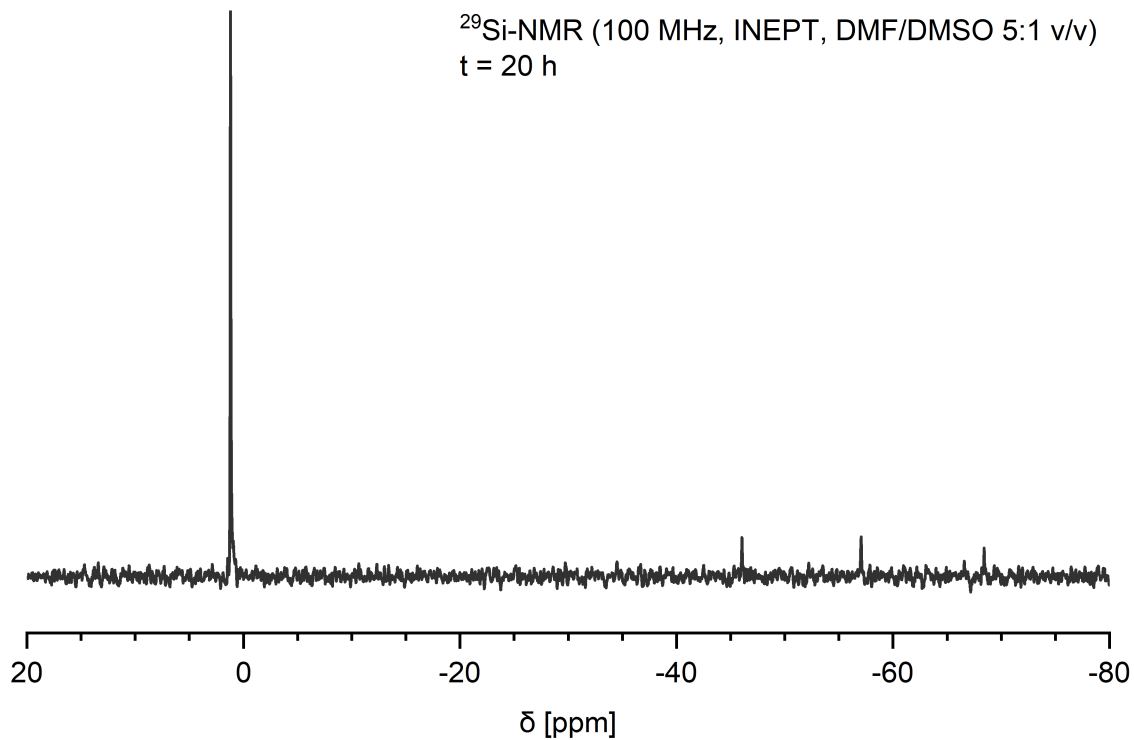**Figure A.6.** Full ^{1}H-NMR spectrum of a $Cs_{0.15}FA_{0.85}PbI_3$ precursor solution containing 0.135 M of APTES and 0.3 M water after 48 h reaction time at 25 °C prepared according to ref. [21].

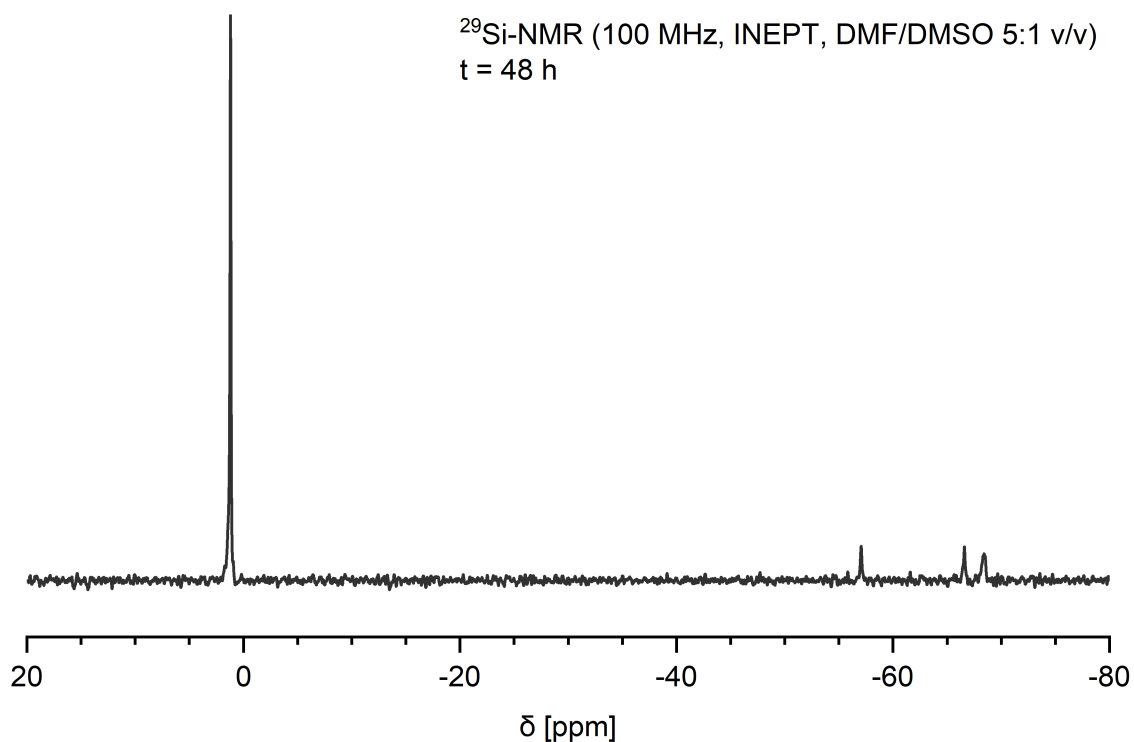^{29}Si-NMR (100 MHz, INEPT, DMF/DMSO 5:1 v/v)
t = 1 h

δ [ppm]

Figure A.7. Full ^{29}Si-NMR spectrum of a $Cs_{0.15}FA_{0.85}PbI_3$ precursor solution containing 0.135 M of APTES and 0.3 M water after 1 h reaction time at 25 °C prepared according to ref. [21].

^{29}Si-NMR (100 MHz, INEPT, DMF/DMSO 5:1 v/v)
t = 20 h

δ [ppm]

Figure A.8. Full ^{29}Si-NMR spectrum of a $Cs_{0.15}FA_{0.85}PbI_3$ precursor solution containing 0.135 M of APTES and 0.3 M water after 20 h reaction time at 25 °C prepared according to ref. [21].
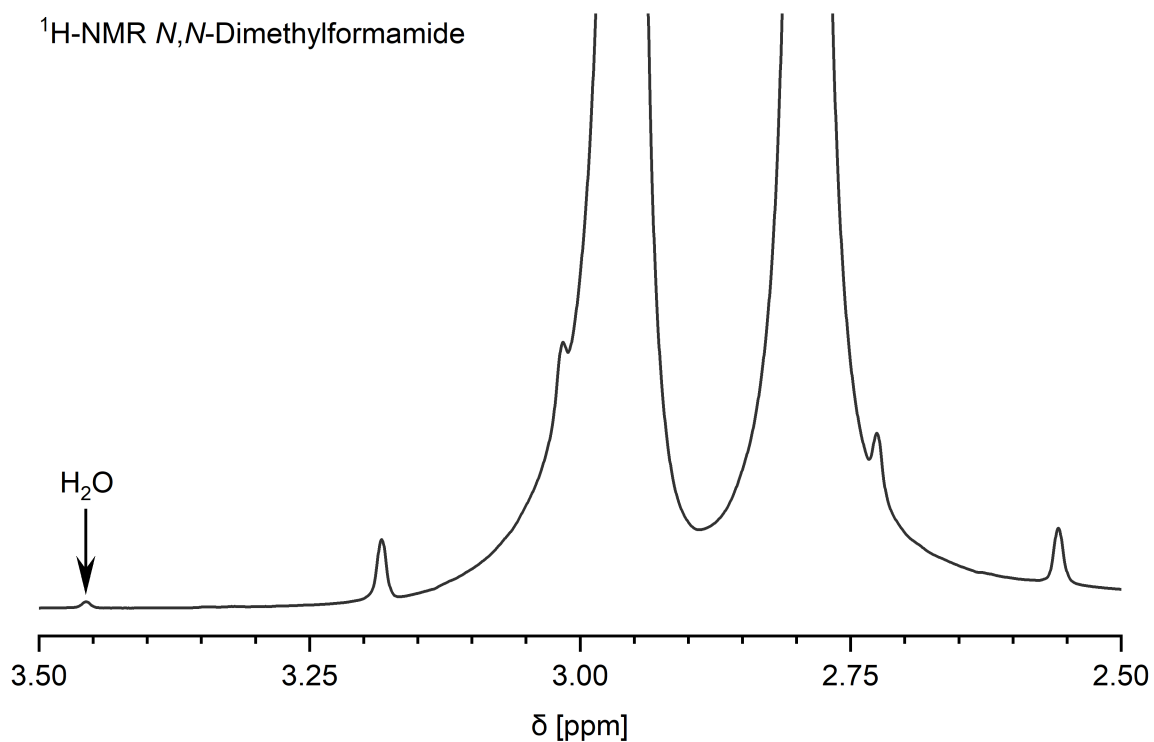
Figure A.9. Full ^{29}Si-NMR spectrum of a $Cs_{0.15}FA_{0.85}PbI_3$ precursor solution containing 0.135 M of APTES and 0.3 M water after 48 h reaction time at 25 °C prepared according to ref. [21].

Figure A.10. Detail of the ^{1}H-NMR spectrum of DMF which was used in all experiments accentuating the peak for residual water.
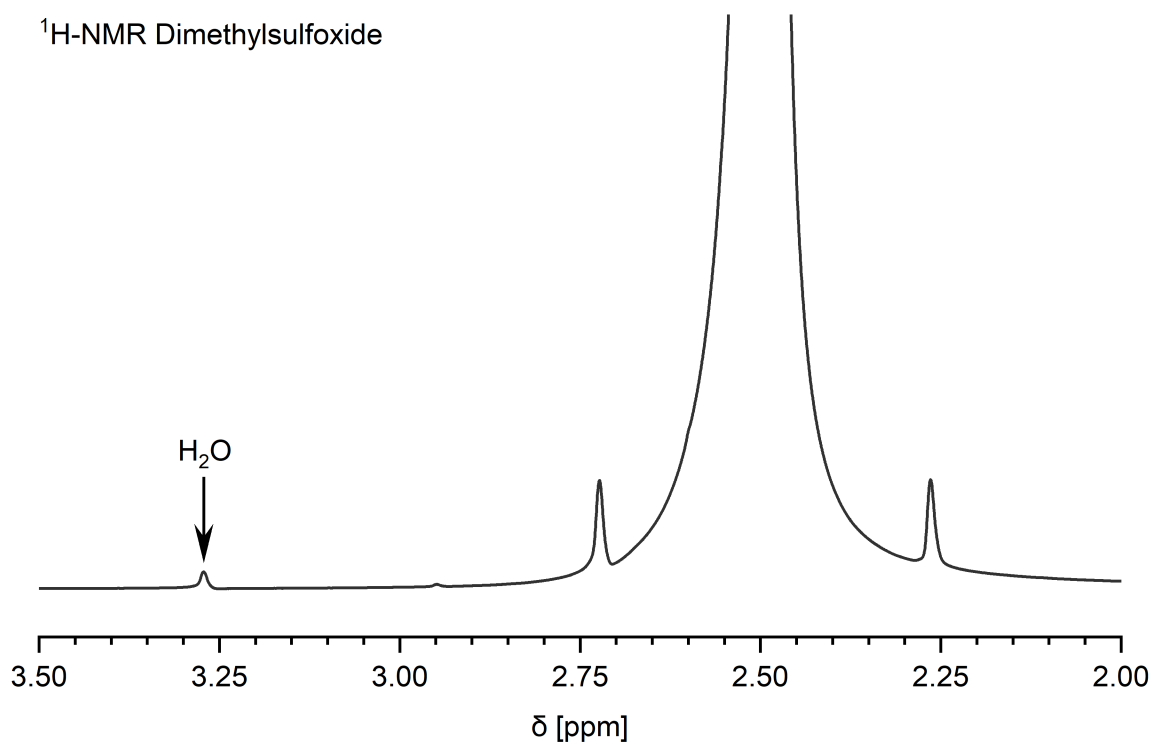
Figure A.11. Detail of the ^{1}H-NMR spectrum of DMSO which was used in all experiments accentuating the peak for residual water.
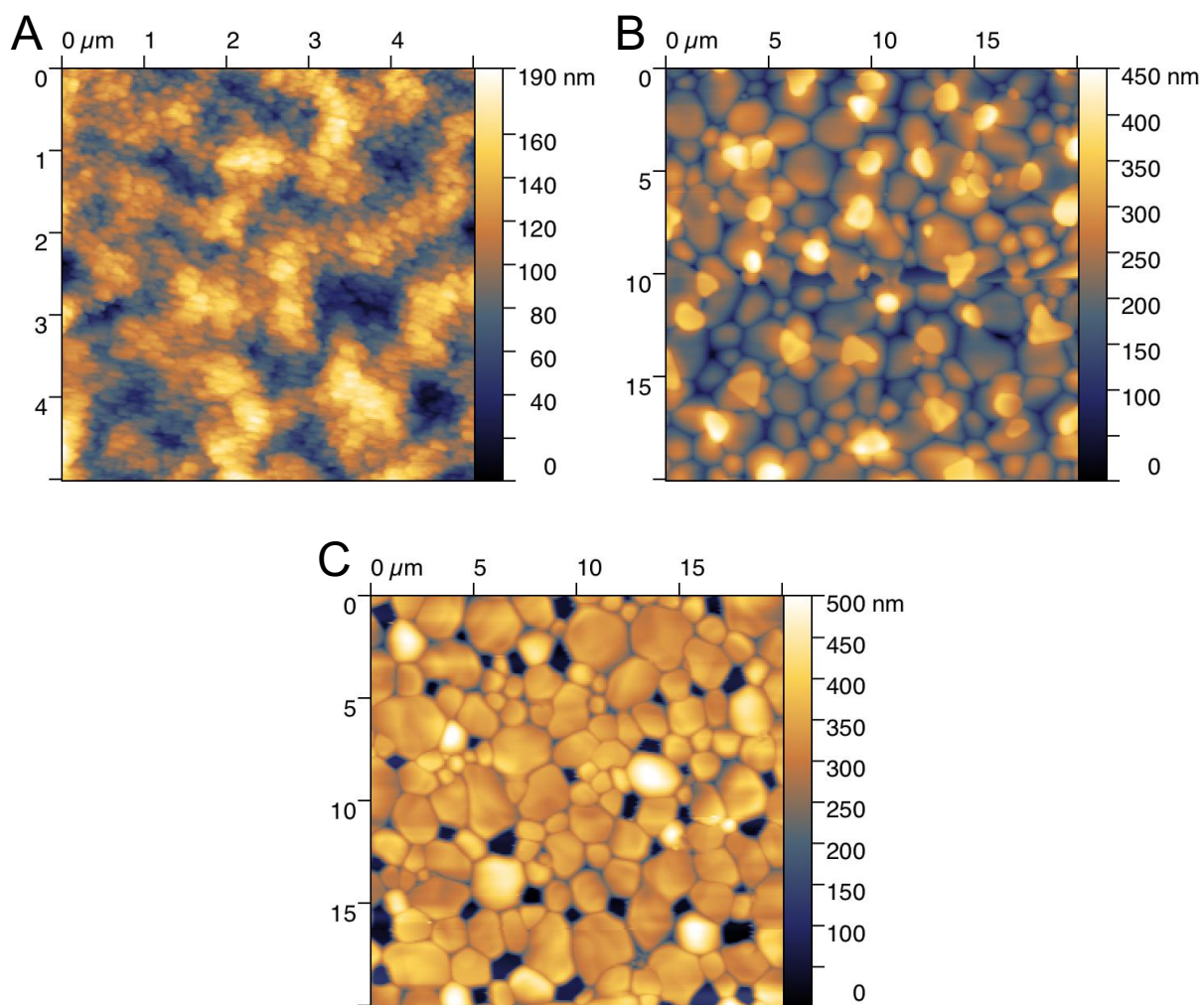
Figure A.12. AFM topography images of (A) a DMSO-annealed, APTES-passivated MAPbI₃ film which exhibits drastically reduced grain sizes, (B) a DMSO-annealed, RbI-passivated MAPbI₃ film clearly showing floating grains, (C) a DMSO-annealed MAPbI₃ film exhibiting a high density of pinholes due to dewetting.